Doctoral Dissertation
Doctoral Program in Chemical Engineering (35^{th}cycle)

Production and activation of shear-responsive drug carriers for treating obstructed blood vessels: a coupled CFD-DEM approach

By

Lorenzo Vasquez Giuliano

******

Supervisor(s):
Prof. Marco Vanni

Doctoral Examination Committee:
Prof. Marco Ellero, Basque Center for Applied Mathematics
Prof. Matthäus Bäbler, KTH Royal Institute of Technology
Prof. Jean-Sébastien Kroll-Rabotin, École des Mines de Nancy
Prof. Chiara Galletti, University of Pisa

Politecnico di Torino
2023

Declaration

I hereby declare that, the contents and organization of this dissertation constitute my own original work and does not compromise in any way the rights of third parties, including those relating to the security of personal data.

Lorenzo Vasquez Giuliano
2023

* This dissertation is presented in partial fulfillment of the requirements for **Ph.D. degree** in the Graduate School of Politecnico di Torino (ScuDo).

Abstract

The obstruction of critical blood vessels caused by clots is one of the leading causes of death worldwide, causing the development of efficient antithrombotic strategies to be of the utmost importance. Blood clots are usually treated using a tissue plasminogen activator (tPA), a protein that is able to dissolve the clot, restoring normal blood flow and preventing the major consequences ischemic events lead to. However, this treatment requires a prompt administration of the active agent and a careful choice of the dosage, as the amount of freely circulating active agent should not overcome a certain threshold. In recent years, a lot of effort has been put into overcoming these limitations and developing novel drug delivery systems. One of the most interesting and promising is based on shear-responsive drug carriers, micrometric clusters of polymeric nanoparticles, coated with the active agent and produced via spray drying. The carriers are stable under normal blood flow conditions but are designed to undergo breakup right onto the clot, in response to the local increase in the hydrodynamic stress caused by the lumen restriction itself. The resulting fragments are more likely to adhere to the clot, enhancing the efficiency of the thrombolytic action.

The present work moves the first steps to the establishment of a simulation framework able to follow the production process of the carriers from the agglomeration via spray drying to the shear-inducted de-agglomeration: the production process of the clusters and their subsequent breakup is investigated and simulated through discrete element methods (DEM), while the flow field in an obstructed blood vessel is investigated using computational fluid dynamics (CFD) techniques to show that the increase in hydrodynamic stress is able to act as a trigger for the activation of the carriers.

A qualitative relationship between the spray drying process conditions and the morphology of the final product has been identified: fast particle diffusion and long shrinkage time (low Péclet number) lead to the formation of compact agglomerates, while hollow agglomerates are obtained for slow particle diffusion and short shrinkage time (high Péclet number). A dataset of plausible compact and hollow carrier morphologies has been generated by DEM spray drying simulations, and a statistical analysis of the response of carriers to the CFD-calculated flow field in an obstructed microfluidic device has been performed, thus linking the process conditions of the formation of agglomerates to their response to pathological shear stresses. The correlation between hydrodynamic forces and internal mechanical stresses has been studied using a discrete element method based on Stokesian dynamics. CFD simulations have shown that the presence of a peak in hydrodynamic forces caused by the occlusion of the vessel can act as an internal, non-invasive activation mechanism for drug carriers.

Future experimental validations of the agglomeration and de-agglomeration process are necessary for the development of a reliable protocol for the production of drug carriers via spray drying and to validate the strict connection between morphology and process conditions that has been found using numerical methods. The direct observation of the activation process of the manufactured agglomerates in a real microfluidic device is necessary for refining the parameters of the proposed framework in order to properly match experimental evidences. At that point, CFD-DEM simulations can act as a valuable guideline for the production process: the choice of the material and the identification of the proper size and shape are the key steps for an optimal design of shear-responsive drug carriers able to correctly perform an efficient thrombolytic action.

Contents

List of Figures

List of Tables

Nomenclature

Roman Symbols

$\mathbf{x}$	Linear position
$\ddot{\mathbf{x}}$	Linear acceleration
$\dot{\mathbf{x}}$	Linear velocity
$\mathbf{D}$	Symmetric component of the velocity gradient
$\mathbf{E}^{\infty}$	Rate-of-strain tensor
$\mathbf{F}$	Force
$\mathbf{n}$	Unit vector
$\mathbf{q}$	Particle orientation
$\mathbf{S}$	Stresslet
$\mathbf{T}$	Torque
$\mathbf{t}_r$	Rolling direction
$\mathbf{t}_s$	Sliding direction
$\mathbf{u}$	Velocity of the fluid
$\mathbf{u}^{\infty}$	Velocity of the undisturbed flow field
$\mathbf{u}_r$	Relative rolling velocity
$\mathbf{y}$	Point of application of a force

$\mathscr{M}^{\infty}$	Far-field mobility matrix
$\mathscr{R}$	Resistance matrix
$\mathscr{R}_{2B}$	Two-body resistance function
$\nabla\mathbf{u}$	Velocity gradient
$\overline{c}_n$	Average coordination number
$\tilde{T}$	Characteristic time
$\tilde{U}$	Characteristic velocity
$\tilde{U}_{max}$	Maximum fluid velocity in a vessel
A	Area
a	Radius of primary particles
A_h	Hamaker constant
b	Contact radius
b_0	Zero-load contact radius
b_h	Contact radius predicted by Hertz theory
C	Solute concentration (continuous method)
C_D	Drag coefficient
D	Diffusivity of the solute
d_c	Diameter of an agglomerate
D_v	Diameter of the obstructed vessel
E	Elastic modulus
f_j	Distribution of forces
F_n	Normal force
F_s	Sliding force

F_{po}	Pull-off force
G	Shear modulus
h	Surface-to-surface distance
h_c	crust thickness of an agglomerate
h_{po}	Pull-off distance
I_{ij}	Component of the inertia tensor
J_{ij}	Oseen-Burgers tensor
k	Droplet shrinkage velocity
k_b	Boltzmann constant
K_H	Hertz stiffness coefficient
k_N	Normal stiffness coefficient
k_r	Rolling stiffness coefficient
k_s	Sliding stiffness coefficient
k_t	Torsional stiffness coefficient
K_{ijk}	Stresslet propagator tensor
L	Characteristic length
m	Mass
M_n^{α}	n-th multipole moment
M_r	Rolling torque
M_t	Twisting torque
N	Tensile stress
N^*	Maximum tensile stress along the path of an agglomerate
n_{CPU}	Number of computational cores

n_{step}	Number of simulation steps
np	Number of particles
P	Point force
p	Pressure
p_0	Coefficient for surface pressure distribution
p_{pack}	Packing porosity
Pe	Péclet number
R	Radius of the droplet
r	Radial coordinate
R_H	Hydraulic radius
R_v	Radius of the internal void core
R_{gyr}	Radius of gyration
R_{ij}	Torque propagator tensor
R_{N^*}	Radial position of the most solicitated bond
Re	Reynolds number
Re_p	Particle Reynolds number
S_c	Contact surface
S_{ij}	Stresslet
s_t	Timestep safety factor
St	Stokes number
St_p	Particle Stokes number
t	Time
u'_i	Flow field disturbance

U_E	Stored elastic energy
U_M	Mechanical energy
U_S	Surface energy
U_T	Total energy of the system
u_z	Displacement along direction z
V	Volume
v	Velocity of the receding front (continuous method)
Z	Computational time
z_0	Minimum approach distance

Greek Symbols

$\boldsymbol{\chi}$	Randomic three-element vector
$\boldsymbol{\omega}$	Rotational velocity
Δt	Timestep
Δt_{cr}	Critical timestep
δ	Equilibrium gap thickness
δ_h	Normal overlap referred to sphere radius
δ_N	Normal overlap
δ_s	Tangential displacement
δ_{ij}	Dirac delta
δ_{po}	Critical overlap
ε_N	Normal strain
ε_{ijk}	Levi-Civita operator
η_r	Rolling damping coefficient

η_s	Tangential damping coefficient
η_t	Torsional damping coefficient
Γ	Dimensionless solute concentration (continuous method)
γ_s	Surface energy density
λ	Mixing index
λ_T	Tabor parameter
ω^∞	Rotational velocity of the undisturbed flow field
μ	Viscosity
μ_F	Friction coefficient
ν	Poisson ratio
ω_{ij}^∞	Antisymmetric component of the velocity gradient
ϕ_c	Friction angle
ϕ_r	Angular displacement for rolling
ϕ_t	Angular displacement for twisting
ρ_p	Density of the particles
σ	Surface tension
τ	Shrinkage time
τ_p	Particle relaxation time
θ	Dimensionless time (continuous method)
$\tilde{\omega}$	Vorticity
$\tilde{\rho}$	Dimensionless radial position (continuous method)
$\tilde{\tau}$	Viscous stress tensor
ξ	Linear displacement

ξ_r	Rolling displacement
ζ	Simulated time
Ω^∞	Rate-of-rotation tensor

Superscripts

$*$	Dimensionless quantity (Stokesian dynamics)
α	Relative to the α-th particle
∞	Relative to undisturbed flow field
ΩF	Relative to angular velocity and force
ΩS	Relative to angular velocity and stresslet
ΩT	Relative to angular velocity and torque
cm	Center of mass
$crit$	Critical value
EF	Relative to rate of strain and force
ES	Relative to rate of strain and stresslet
ET	Relative to rate of strain and torque
$hydro$	Hydrodynamic
PF	Point-force
t	Trial
UF	Relative to linear velocity and force
US	Relative to linear velocity and stresslet
UT	Relative to linear velocity and torque

Subscripts

0	Initial

br	Breakup
$brown$	Brownian
c	Capillary
coh	Cohesive
$drag$	Drag
ext	External
l	Liquid
max	Maximum
min	Minimum
n	Relative to normal direction
p	Particle
po	Pull-off
r	Relative to rolling
s	Relative to sliding
t	Relative to twisting

Acronyms / Abbreviations

BBO	Basset-Boussinesq-Oseen
CDF	Cumulative Distribution Function
CFD	Computational fluid dynamics
DEM	Discrete element method
DMT	Derjaguin-Muller-Toporov
DoF	Degrees of freedom
FT	Force-Torque

FTS	Force-Torque-Stresslet
JKR	Johnson-Kendall-Roberts
tPa	Tissue plasminogen activator
VDW	Van der Waals
WSS	Wall shear stress

Chapter 1

Introduction

One of the main causes of death worldwide is the obstruction of critical blood vessels caused by clots [1]. Thrombosis events lead to a variety of life-threatening ischemic conditions, such as strokes or myocardial infarction. Therefore, the development of efficient antithrombotic strategies is of the utmost importance. The only treatment for acute ischemic events currently approved by the Food and Drug Administration is the use of a tissue plasminogen activator (tPA), a protein that is able to dissolve the clot, restoring normal blood flow and preventing the major consequences ischemic events lead to [2, 3]. However, this kind of treatment is heavily limited: it requires a prompt administration of the active agent and a careful choice of the dosage, in order to limit the amount of freely circulating active agent, which could lead to different but equally severe adverse effects, such as bleeding.

In recent years, a lot of effort has been put into overcoming the limitations mentioned above and developing novel drug delivery systems. The undesired effects of the drug along its circulation in the body should be minimized, and a localized action of the treatment is desired, i.e., the design of drug carriers should focus on their ability to deliver the drug only at the pathological location. To address this challenge, a number of strategies based on a *targeted* drug delivery system has been developed [4]: liposomes encapsulating tPA and undergoing rupture as a response to an external ultrasound source [5], magnetic microrods mechanically disrupting the clot under the action of an external magnetic field [6, 7], carriers made of microbubbles covered by magnetic nanoparticles with responsiveness to both the magnetic field and ultrasound solicitation [8], polymer particles encapsulating magnetite and tPA [9], and core–

shell fibrin-specific colloidal hydrogels [10]. However, all such approaches show some critical aspects: they require a rather precise knowledge of the clot position, because an external activation mechanism is needed to proptly release the drug on the pathological site.

A promising drug targeting method has been proposed by Korin and coworkers [11], and it is based on shear-responsive drug carriers. The drug carrier is here constituted by a micrometric cluster of polymeric nanoparticles, coated with the active agent and produced via spray drying. After intravenous injection, the agglomerates are stable under normal blood flow conditions but are designed to undergo breakup right onto the clot, in response to the local increase in the hydrodynamic stress caused by the lumen restriction itself [12, 13]. The resulting fragments experience a lower drag force with respect to the parent agglomerate and therefore are more likely to adhere to the clot and perform the thrombolytic action, as visualized in Fig. 1.1. This biophysical strategy is borrowed from the shear-based activation mechanism of normal circulating platelets and offers a robust and broadly applicable targeting method: it benefits of the narrowing of the lumen diameter and of the consequent local increase in the shear stress, which occurs regardless of the specific cause or location of the clot. Moreover, no external activation mechanisms are required: the drug release is triggered by the breakup of the carrier, that is induced by the obstruction itself. Even if there is uncertainty about the efficacy of this approach in dealing with fully obstructed vessel, and the knowledge of the type and location of the clot is needed to select the proper carrier size and site of administration, the drug delivery strategy based on shear-responsive carriers is undoubtedly interesting, as it is a possible answer to the two main challenges in the treatment of obstructed blood vessels: the undesired interactions with non-pathological regions would be drastically reduced and the *internal* activation mechanism guarantees a localized and performative drug release.

Although preclinical tests have shown convincing results, shear-responsive agglomerates are not widely employed as drug carriers at the present time. Demanding and challenging in-vivo and/or in-vitro experimental trials are in fact needed to refine such a drug delivery strategy. A proper and effective design of the drug carriers requires a thorough investigation of the flow field in proximity of an arterial obstruction, together with the response of carriers to the hydrodynamic stress, that is related to properties such as dimension, shape and material, and the conditions required in the production process to obtain shear-responsive agglomerates that are suitable for the proposed pharmaceutical issue. Numerical simulations represent a powerful tool to establish a framework that can act as a guide for future experimental tests. Computational fluid dynamics (CFD) simulations, for instance, have been successfully used to predict the wall shear stress distribution in aortic vessels, accurately reconstructed by magnetic resonance imaging [14], and simulations on model representations of obstructed vessels elucidate the role that the blood flow field distortion has on platelet aggregation and clot formation [15]. Cardiovascular research has also used CFD to predict how hemodynamics changes as a result of pathology [16], surgical outcomes [17, 18], design artificial medical devices [15]. Ultimately, computational fluid dynamics has been frequently used to obtain a complete and thorough knowledge of the flow characteristics, necessary to investigate the effect of the hydrodynamic stress on agglomerates flowing inside an obstructed vessel. A detailed simulation of the behaviour of agglomerates immersed in a flow field, i.e., information about their mechanical response to fluid dynamic stress eventually leading to breakup, can in fact be obtained by coupling CFD results with a discrete element method (DEM) [19].

The present work investigates the flow field in an obstructed blood vessel to show that the increase in hydrodynamic stress is able to act as a trigger for the activation of shear-responsive agglomerates. The formation of the shear-responsive drug carriers via spray drying is investigated and simulated through DEM as well. This leads to a better comprehension of the influence of process conditions on the morphology of the drug carriers, and ultimately on their mechanical stability. Once that the flow field inside an obstructed vessel is fully known and a population of well-characterized carriers with different morphologies and level of agglomeration has been obtained, the two branches of the problem can be joint together: a discrete element method

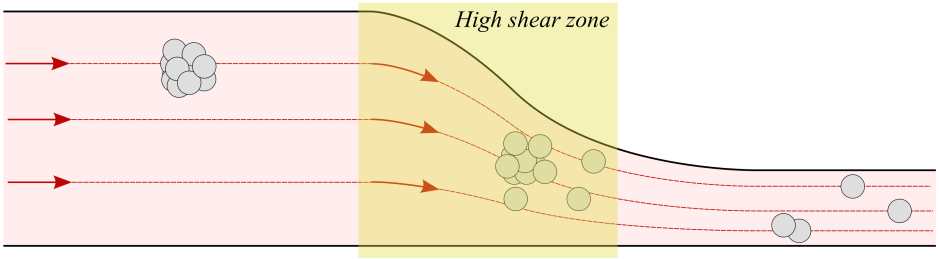

Fig. 1.1 Agglomerate of nanoparticles flowing in a partially obstructed vessel. When the agglomerate enters the high shear zone generated by the lumen obstruction, it breaks into smaller fragments.

based on Stokesian dynamics is employed to accurately evaluate the stresses acting on the particle–particle bonds and to finally predict the occurrence of breakup in the obstruction. In other words, the present work takes the first steps to the establishment of a simulation framework able to follow the production process of the carriers from the agglomeration via spray drying to the shear-induced de-agglomeration.

As mentioned above, the first step of the work is focused on the formation of the carriers via spray drying, and the simulation of the process through a DEM approach. The aim of this step is to enlight the influence of process conditions on the morphology of agglomerates produced by spray drying, focusing on the role of the Péclet number in obtaining different recognizable classes of agglomerates. As a result of the simulation campaign, a dataset of agglomerate morphologies with different properties is obtained. The methods are discussed in Chapter 2: section 2.1 shows the basic principles of contact mechanics between particles, while in section 2.2 the discrete element method and the related software used for the simulation of agglomerate formation via spray drying is presented. The results are summarized in Chapter 3, where DEM simulations are first validated against a continuous method for short times and then a correlation between the final obtained morphology and the process conditions has been found.

The DEM approach used in the first step is devoted to simulate the agglomeration of nanoparticles due to the shrinkage of a single droplet in a spray drying process. However, a refinement of the DEM method is required to effectively simulate the restructuring and breakup experienced by agglomerates when exposed to hydrodynamic forces. Therefore, the second step of the work describes and applies the Stokesian dynamics approach, a DEM method suitable for de-agglomeration phenomena. The methodology is depicted in Chapter 2, section 2.3, while in Chapter 4 the behaviour of clusters exposed to simple flows is investigated: the main dissimilarities in the response of agglomerates having different morphologies but exposed to the same flow field are highlighted, and an evaluation of the impact of simplifying assumptions on the upcoming simulation campaign is conducted.

In the third step of the work, the flow field in a microfluidic device mimicking an obstructed blood vessel is investigated using CFD techniques. Then, results from CFD and DEM are coupled in order to calculate the mechanical response of agglomerates produced via spray drying to the pathological flow field stress typically encountered in obstructed blood vessels. The effect of the obstruction in the microchannel is also compared with the peak in hydrodynamic stress obtained in more realistic representations of an obstructed blood vessel, an axisymmetric and an asymmetric stenosis, to verify the feasibility of the artificial microfluidic device to reproduce the pathological shear stress encountered in proximity of a clot. The methodology followed for CFD simulations is described in Chapter 2, section 2.4, and the results are discussed in Chapter 5.

Chapter 2

Methods

Parts of this Chapter are based on articles published by the candidate. In particular, sections 2.2 and 2.3 are partially taken from "Micromechanics and strength of agglomerates produced by spray drying", Vasquez Giuliano, L., Buffo, A., Vanni, M., Frungieri, G., JCIS Open, 2023 [20]; section 2.4 is partially taken from "Response of shear-activated nanotherapeutic particles in a clot-obstructed blood vessel by CFD-DEM simulations", Vasquez Giuliano, L., Buffo, A., Vanni, M., Lanotte, A. S., Arima, V., Bianco, M., Baldassarre, F., Frungieri, G., The Canadian Journal of Chemical Engineering, 2022 [19].

2.1 Contact mechanics

In this section, the basics of contact mechanics between particles are discussed. The case of colliding particles in absence of adhesion effects is presented, and then a model for collision in presence of adhesion is formulated. A more detailed review of the subject can be found in reference [21].

2.1.1 Basics of contact mechanics - non adhesive particles

When two bodies collide, deformation and stresses occur, giving rise to contact forces and torques acting on the two bodies. The comprehension of contact mechanics is of the utmost importance to model the phenomena. To understand the principal laws underlying the phenomenon, let's consider a pair of non-adhesive spheres in contact.

Sphere i is characterized by radius a_i, elastic modulus E_i, Poisson ratio ν_i and shear modulus G_i, sphere j is characterized by radius a_j, elastic modulus E_j, Poisson ratio ν_j and shear modulus G_j. It is convenient to define *effective* parameters a, E, G as:

$$\begin{aligned} \tfrac{1}{a} &= \tfrac{1}{a_i} + \tfrac{1}{a_j} \\ \tfrac{1}{E} &= \tfrac{1-\nu_i^2}{E_i} + \tfrac{1-\nu_j^2}{E_j} \\ \tfrac{1}{G} &= \tfrac{2-\nu_i}{G_i} + \tfrac{2-\nu_j}{G_j} \end{aligned} \tag{2.1}$$

If a force that is normal to sphere surface is acting, the spheres contact each other not over a single point, but over a finite, circular region. The contact radius b is defined as the radius of the contact region. Since the spheres are deformed at contact, it is possible to define also the normal overlap δ_N as the difference between the sum of the undeformed spheres' radii and the distance between their centers. Simple geometric considerations [21] show that the contact radius is related to normal overlap according to the following equation:

$$b = \sqrt{a\delta_N} \tag{2.2}$$

Eq. 2.2 is valid only if the contact radius is small compared to the radius of the sphere. The system made by two deformed particles in contact is illustrated in Fig. 2.1.

Let's consider direction z to be the direction normal to the contact region. The elastic displacements of the two spheres along z, namely u_{zi} and u_{zj}, have to satisfy the kinematic relationship expressed by Eq. 2.3 at any point on the contact region located at a distance r from the center of the region.

$$u_{zi} + u_{zj} = \delta_N - \frac{r^2}{2a} \tag{2.3}$$

Contact models relate the normal contact force F_n with the normal overlap δ_N. This relationship has been expressed in various ways: force-displacement laws modelled over a spring, a dashpot, a slider or combinations have been exploited, and if the dissipation of energy and the plastic deformation are taken into account, an hysteretic behaviour of the load-displacement curve should be expected.

The mutual configuration of two spheres has 6 degrees of freedom (DoF): 1 DoF from normal straining, 2 DoFs from sliding, 1 DoF from twisting, and 2 DoFs from

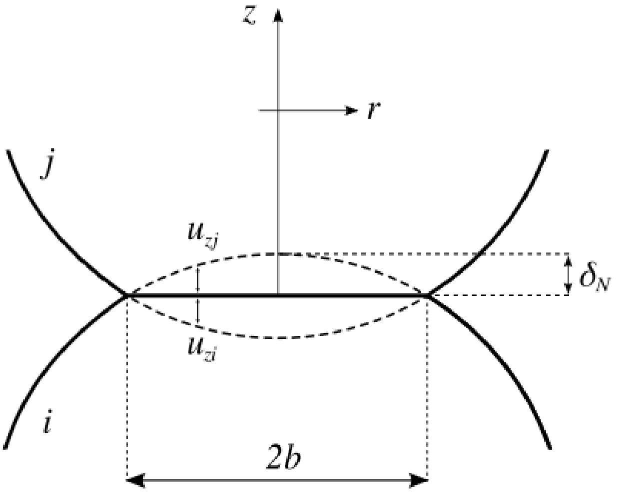

Fig. 2.1 Normal overlap δ_N and contact radius b for two spherical particles in contact. Dashed lines denote the undeformed particle surfaces, solid lines denote the deformed particle surfaces.

rolling, as visualized in Fig. 2.2. This means that also resistances to non-normal motions should be modelled, and they can be expressed as forces, torques or a combination of them.

An expression for normal elastic force between two non-adhesive elastic spheres in contact has been derived by Hertz [22]. The derivation has been conducted under a few working hypoteses: each sphere is treated as an elastic half-space loaded within the small contact region (contact radius much smaller than the sphere radius) producing displacements satisfying Eq. 2.3; moreover, contact surfaces are supposed to be frictionless, so that only the normal interaction force is relevant.

Let's consider a cylindrical polar coordinate system (r, θ, z), being $z = 0$ the top boundary of an elastic half-space that fills the region $z < 0$. It is stated in Eq. 2.3 that the displacement u_z in the z direction within a circle of radius b on the surface $z = 0$ is proportional to r^2. This can be obtained by imposing the following surface pressure distribution:

$$p = p_0 \left[1 - (r/b)^2\right]^{1/2} \tag{2.4}$$

where the coefficient p_0 is related to the elastic normal force F_n, that pushes the particles together along the line of centers (Eq. 2.5).

$$F_n = 2\pi \int_0^b p(r) r dr = \frac{2}{3} p_0 \pi b^2 \tag{2.5}$$

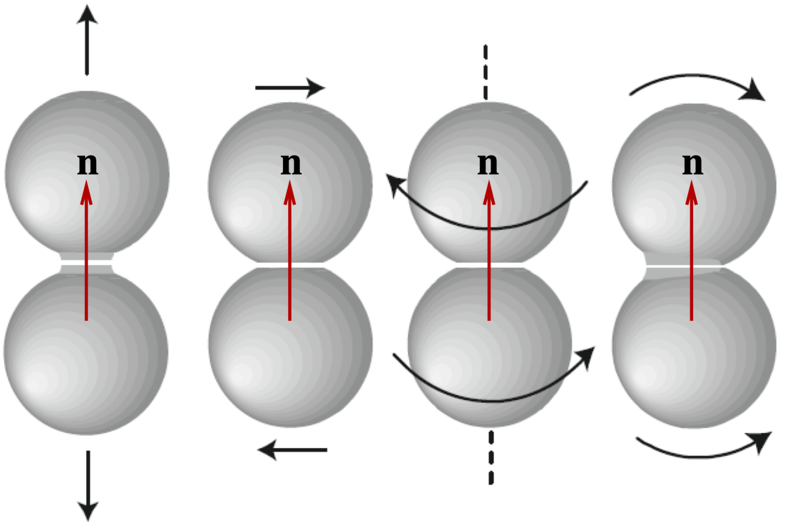

Fig. 2.2 Relative displacements between contacting spheres. From left to right: normal interaction; sliding; twisting; rolling.

Let's consider now a point force P acting perpendicularly to the surface of the elastic half-space. The solution for the problem is given by Timoshenko and Goodier [23] as:

$$[u_z]_{z=0} = \frac{P(1-\nu_i^2)}{\pi E_i r} \tag{2.6}$$

when considering the material labelled as i. If a distributed load $p(r)$ over a circle with radius b is considered, P can be thought as an infinitesimal load $p\,db$ applied at the location $\mathbf{x}'$ on the half-space surface. If S_c is the contact surface of radius b, the displacement at the generic location $\mathbf{x}$ is:

$$u_z(\mathbf{x}) = \frac{1-\nu_i^2}{\pi E_i} \int_{S_c} \frac{p(\mathbf{x}')}{|\mathbf{x}'-\mathbf{x}|} db' \tag{2.7}$$

Performing the integration and substituting Eq. 2.4 into Eq. 2.7:

$$u_{zi} = \frac{1-\nu_i^2}{E_i} \frac{\pi p_0}{4b} \left(2b^2 - r^2\right) \tag{2.8}$$

An analogous expression can be written for u_{zj}. Substituting in Eq. 2.3:

$$u_{zi} + u_{zj} = \frac{\pi p_0}{4bE} \left(2b^2 - r^2\right) = \delta_N - \frac{r^2}{2a^2} \tag{2.9}$$

From Eq. 2.2 and 2.9 (at $r > 0$), it is possible to obtain the following expressions:

$$\begin{aligned} b &= \tfrac{\pi a p_0}{2E} \\ \delta_N &= \tfrac{\pi b p_0}{2E} \end{aligned} \tag{2.10}$$

Finally, the classical Hertz force expression for elastic contact of contacting spheres is obtained by substituting Eq. 2.10 into Eq. 2.5.

$$F_n = \frac{4Eb^3}{3a} = K_H \delta_N^{3/2} \tag{2.11}$$

where K_H is the stiffness coefficient given by:

$$K_H = \frac{4}{3} E \sqrt{a} \tag{2.12}$$

Eq. 2.12 can be re-written as:

$$F_n = k_N \delta_N \tag{2.13}$$

where the stiffness k_N is expressed in term of contact region radius as $k_N = 4Eb/3$.

In an elastic contact model, the conservation of the net kinetic energy is implied, i.e., the relationship between force and displacement is the same during loading and unloading. In the practice, a dissipation to heat occurs during a collision process. There are models to characterize a collision by a restitution coefficient: a restitution coefficient of unity is associated to a complete elastic collision, while for a complete inelastic collision the restitution coefficient is zero.

2.1.2 Adhesive force in the normal interaction

In Section 2.1.1 contact mechanics between spheres has been discussed as they were adhesionless. Although this theory is effectively applicable in problems involving granular materials of large size, adhesion phenomena are of the utmost importance at small scales. Spheres of millimetric size are sometimes subject to liquid bridging, while van der Waals attraction phenomena are always significant for micrometric particles [24]. Experimental evidences of a deviation of the area of the contact region from the value predicted by the Hertz theory for small particles highlight the importance of interaction forces at small scales: van der Waals forces, electric double layer repulsion, liquid bridging, and others.

Macroscopic van der Waals forces arise from the interaction potential between atoms or molecules. At the particle scale, the adhesive force betwen two particles originates from the sum of attraction forces between all the microscopic elements within the two bodies. This results in an attraction potential that is inversely proportional to the square of the surface-to-surface distance h and directly proportional to the Hamaker coefficient A_h, whose magnitude depends on the material of the two interacting bodies and the medium filling the space between them. The pressure p, i.e., the normal force per unit area, is obtained from the derivative of the interaction energy with respect to the surface-to-surface distance.

The pairwise summation of intermolecular energies generates the interaction potential between two macroscopic bodies as the sum of a long-range attractive potential and a short-range repulsive potential. This means that two relatively distant bodies are attracted to each other, until the point where short-range steric repulsion becomes relevant. The long-range force is the macroscopic van der Waals force, resulting from induction, orientation and dispersion intermolecular effects. The latter is the most relevant: it originates at atomic/molecular level from the fact that the instantaneous position of electrons surrounding an atomic nucleus gives rise to a temporary electric polarized field. This field induce polarization in surrounding atoms, thus resulting in an electrostatic interaction between induced dipoles also at the particle scale. The short-range force is the steric repulsion due to the overlap of electron clouds of two different atoms. Fig. 2.3 shows the typical trend of the normal force as a function of the distance h between two macroscopic plane surfaces. It has the generic form[1]:

$$p(h) = -Ah^{-n} + Bh^{-m} \tag{2.14}$$

where A and B are positive constants, and m is a positive number higher than n. The sign of p is conventionally negative when referred to a compression: therefore, the first term accounts for the attractive force, the second term accounts for the repulsive one. If $m > n$, attraction is more significant at long range, while repulsion prevales at short range. The term δ is the equilibrium gap thickness for two contacting spheres in a vacuum, i.e. the separation distance for which attractive forces and repulsive forces balance each other, and therefore $p(\delta) = 0$. With these considerations made, it is possible to define the surface energy density γ_s as half the reversible work (per unit surface area) required to separate two surfaces with initial separation distance

---

[1] If the molecules of the plates interact via the 6-12 Lennard-Jones potential, the exponents of Eq. 2.14 become $n = 3$, $m = 9$.

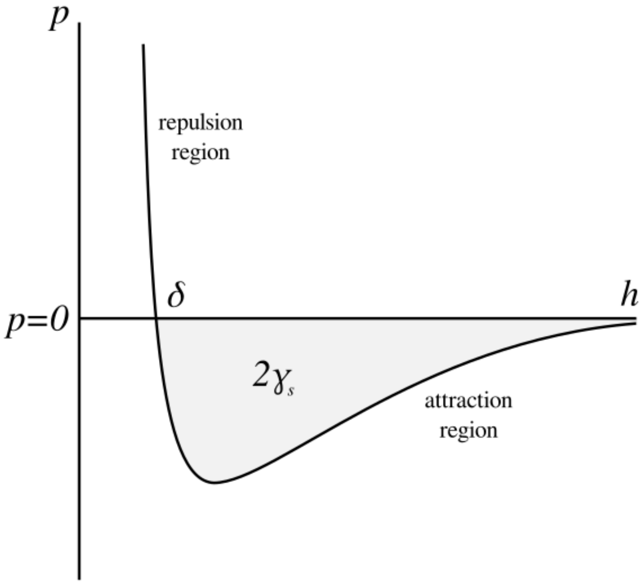

Fig. 2.3 Normal force per unit area p as a function of the surface-to-surface distance h. The term δ is the equilibrium gap thickness, and it separates the attraction region from the repulsion region. The area between the curve and the horizontal axis in the attraction region is $2\gamma_s$.

δ. It can be noticed that the area between the curve and the horizontal axis in the attraction region is $2\gamma_s$.

In order to appropriately model the combined adhesion-elastic force for two contacting spheres, the length scales associated respectively with elastic deformation and with adhesive force have to be estimated and compared. This result can be obtained by using the argument suggested by Tabor, which is based on the analysis of the orders of magnitude. According to the Hertz theory, the normal overlap δ_N in absence of adhesion can be written by combining Eq. 2.11 and 2.12 as:

$$\delta_N = \left(\frac{9}{16}\frac{F_n^2}{E^2 a}\right)^{1/3} \tag{2.15}$$

where F_n is the compressive force. If compression is generated by attractive van der Waals force, we can assume that the elastic normal force F_n has the same order of magnitude of the critical pull-off force F_{po}, which is proportional to the effective sphere radius and to the surface energy density as will be shown in Eq. 2.35. Consequently, we set $F_n \sim a\gamma_s$ in Eq. 2.15, and thus the order of magnitude of the normal overlap with adhesion can be estimated as:

$$\delta_N \propto \left(\frac{a\gamma_s^2}{E^2}\right)^{1/3} \tag{2.16}$$

Eq. 2.16 estimates the length scale associated with elastic deformation. The equilibrium gap thickness δ of Figure 2.3 is the length scale associated with the adhesive force, and their ratio is defined as the Tabor parameter λ_T (Eq. 2.17).

$$\lambda_T = \left(\frac{4a\gamma_s^2}{E^2\delta^3}\right)^{1/3} \tag{2.17}$$

For $\lambda_T \ll 1$ the elastic deformation has a negligible effect: therefore, the total normal force acting on the particle is simply the sum of the elastic force predicted by the Hertz theory and the adhesive force for two contacting spheres. In this case, the adopted model for the normal contact force is the Derjaguin-Muller-Toporov (DMT) model [25]. On the other hand, for $\lambda_T \gg 1$ the elastic deformation plays a non-negligible role: in this case, spheres are subjected to deformation and a flattened contact region has to be considered. The adhesive force is supposed to act only within the contact region, and it can be determined by approximating the contacting sphere surfaces as two flat planes. This is what happens with compliant materials and, in this case, the adopted model for the normal contact force is the JKR model [26]. The JKR model is indeed the one adopted for breakup DEM simulations in this work.

As mentioned above, in JKR model it is assumed that for two spheres with radius a_1 and a_2 the contact radius b is larger than the contact radius predicted by the Hertz theory, from now on referred to as b_h, because of the additional compression due to adhesive force, and that adhesive force only acts inside the contact region. These considerations are summed up in Fig. 2.4.

The following approach is adopted to determine the contact radius b and the critical pull-off force F_{po}: the total energy U_T of the system is estimated as a function of b, then the equilibrium condition $dU_T/db = 0$ is imposed. U_T can be thought as the sum of three terms: the stored elastic energy U_E, the mechanical energy U_M, and the surface energy U_S. Given the normal loading F with no adhesion, the contact radius is the one predicted by Hertz theory. Recalling Eq. 2.11 and 2.12 it is possible

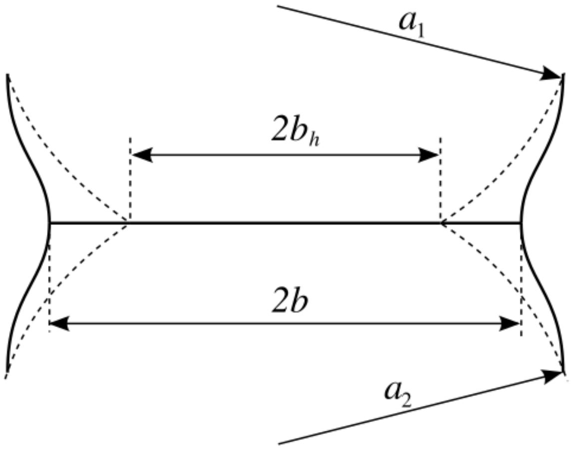

Fig. 2.4 Visual comparison of the contact between two spheres with radius a_1 and a_2 as predicted by Hertz model and JKR model. Contact radius is b_h and b respectively.

to write the following expression for F:

$$F = \frac{4}{3}\frac{Eb_h^3}{a} = \frac{\kappa b_h^3}{a} = \kappa\sqrt{a}\delta_h^{3/2} \tag{2.18}$$

$\kappa = 4E/3$ is a coefficient related to the stiffness ($\kappa = K_H/\sqrt{a}$), and the normal overlap δ_h is equal to b_h^2/a.

It is now useful to introduce the plot of normal compressive load F as a function of the normal overlap (Fig. 2.5): the state of the system described by the Hertz equation is associated to point A in the plot. When adhesive force is taken into account, the enhanced compression makes the contact area, the contact radius and the normal overlap larger. The point in Fig. 2.5 representing this situation is point B. The effective Hertz loading F_1 associated to the contact radius b would be:

$$F_1 = \frac{\kappa b^3}{a} = \kappa\sqrt{a}\delta_1^{3/2} \tag{2.19}$$

where $\delta_1 = b^2/a$. Following the curve of Hertz loading, it can be noticed that the point representing this situation is point C. The elastic energy stored in the system can be obtained using Fig. 2.5. In fact, the plot shows the two steps composing the JKR loading path:

- *O-C* is a Hertz-type loading with no adhesion effects, i.e., with $\gamma_s = 0$, that requires energy U_{O-C} ;

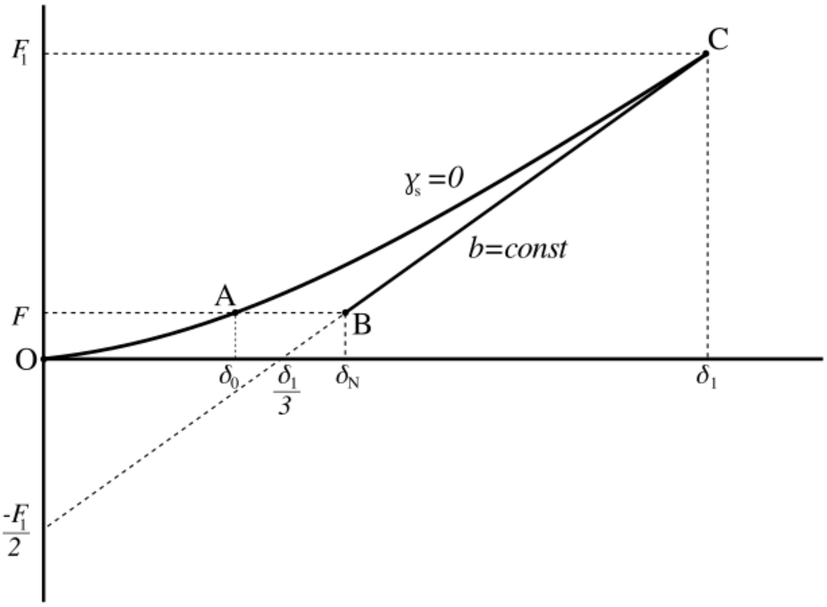

Fig. 2.5 Normal compressive load as a function of the normal overlap. Letters illustrate the loading path of JKR model: Hertz-type loading from O to C with $\gamma_s = 0$; unloading from C to B at constant contact radius b.

- *C-B* is an unloading process at constant contact radius b, that releases energy U_{C-B} .

The energy required for the first step is:

$$U_{O-C} = \int_0^{\delta_1} F d\delta_N = \frac{2}{5}\kappa a^{1/2}\delta_1^{5/2} = \frac{2}{5}\kappa\frac{b^5}{a^2} \tag{2.20}$$

To calculate the energy released in the second step, Eq. 2.21 from Boussinesq theory is employed [27], relying on the fact that the unloading process is similar to the problem of a flat punch.

$$d\delta_N = \frac{2dF}{3b\kappa} \tag{2.21}$$

The integration of Eq. 2.21 leads to an expression for the overlap δ_N at point B. Thanks to Eq. 2.18 and 2.19 it is possible to write it as a function of b, b_h and a.

$$\delta_N = \delta_1 + \frac{2F - 2F_1}{3b\kappa} = \frac{b^2}{3a} - \frac{2b_h^3 b^{-1}}{3a} \tag{2.22}$$

The energy associated to the second step is therefore:

$$U_{C-B} = \int_{\delta_1}^{\delta} F d\delta_N = \int_{F_1}^{F} \frac{2F}{3b\kappa} dF = \frac{F^2 - F_1^2}{3b\kappa} = \frac{1}{3}\kappa \frac{b_h^6 b^{-1} - b^5}{a^2} \tag{2.23}$$

It can be noticed that, due to the fact that b is larger than b_h, U_{C-B} has a negative value: in fact, it represents a release of energy during the unloading step. Finally, the elastic energy can be calculated as:

$$U_E = U_{O-C} + U_{C-B} = \frac{1}{15}\kappa \frac{b^5}{a^2} + \frac{1}{3}\kappa \frac{b_h^6 b^{-1}}{a^2} \tag{2.24}$$

The mechanical energy U_M at point B is equal to $-F\delta_N$. Knowing Eq. 2.18 and 2.21 it can be written as:

$$U_M = -\frac{1}{3}\kappa \frac{b_h^3 b^2 + 2 b_h^6 b^{-1}}{a^2} \tag{2.25}$$

The surface energy U_S is simply given by:

$$U_s = -2\pi\gamma_s b^2 \tag{2.26}$$

The total energy can finally be written as the sum of the elastic, mechanical and surface energy.

$$U_T = \frac{1}{15}\kappa \frac{b^5}{a^2} - \frac{1}{3}\kappa \frac{b_h^6 b^{-1}}{a^2} - \frac{1}{3}\kappa \frac{b_h^3 b^2}{a^2} - 2\pi\gamma_s b^2 \tag{2.27}$$

The equilibrium condition is:

$$\frac{dU_T}{db} = \frac{\kappa}{3b^2a^2}\left[b^6 - 2\left(b_h^3 + 6\pi a\gamma_s \frac{a}{\kappa}\right) b^3 + b_h^6\right] = 0 \tag{2.28}$$

Using expressions for F and F_1 (Eq. 2.18 and 2.19), and solving Eq. 2.28 for F_1:

$$F_1 = F + 6\pi a\gamma_s + \sqrt{12\pi a\gamma_s F + (6\pi a\gamma_s)^2} \tag{2.29}$$

If $F = F_n$ and substituting again $F_1 = b^3\kappa/a$, an equation for the contact radius in presence of adhesion is obtained.

$$b^3 = \frac{3a}{4E}\left[F_n + 6\pi a\gamma_s + \sqrt{12\pi a\gamma_s F_n + (6\pi\ a\gamma_s)^2}\right] \tag{2.30}$$

Moreover, an expression for the normal overlap can be obtained by re-arranging previous results into an expression for $F - F_1$ and substituting into Eq. 2.22.

$$\delta_N = \frac{b^2}{a} - \sqrt{\frac{4\pi b\gamma_s}{E}} \tag{2.31}$$

A relevant parameter descending from these equations is the contact radius at zero applied load b_0, obtained by setting $F_n = 0$ in Eq. 2.30.

$$b_0 = \left(\frac{9\pi\gamma_s a^2}{E}\right)^{1/3} \tag{2.32}$$

Modified forms ot these results express the normal force and the normal overlap in terms of b/b_0 and referred to the critical force and overlap at the pull-off point, namely F_{po} and δ_{po} respectively [28].

$$\frac{F_n}{F_{po}} = 4\left(\frac{b}{b_0}\right)^3 - 4\left(\frac{b}{b_0}\right)^{3/2} \tag{2.33}$$

$$\frac{\delta_N}{\delta_{po}} = 6^{1/3}\left[2\left(\frac{b}{b_0}\right)^2 - \frac{4}{3}\left(\frac{b}{b_0}\right)^{1/2}\right] \tag{2.34}$$

The critical pull-off force and the critical overlap predicted by the JKR model are:

$$F_{po} = 3\pi a\gamma_s \tag{2.35}$$

$$\delta_{po} = \frac{b_0^2}{2\cdot 6^{1/3}\cdot a} \tag{2.36}$$

According to JKR theory, when particles are moved away the overlap is allowed to assume negative values, taking into account the necking of the material. Complete detachment happens at the critical pull-off point, i.e., when $F_n = F_{po}$ and $\delta_N = \delta_{po}$.

2.1.3 Non-normal interactions

Non-normal interaction modes have to be discussed as well. A sphere "slides" when its surface slips relative to that of the other sphere in contact. This is due to relative tangential motion of the surfaces within the contact region. The slip velocity is $\mathbf{u}_s$, oriented along the slip direction $\mathbf{t}_s$, and along the same direction the slip resistance force F_s acts. Since F_s is not directed through the sphere center, a sliding torque $r_i F_s(\mathbf{n} \times \mathbf{t}_s)$ arises. The tangential force acting on impacting spheres is usually determined relying on the spring-dashpot-slider model by Cundall and Strack [29]. According to this model, F_s is proportional to the tangential displacement δ_s and depends on the sliding velocity $\mathbf{u}_s$ according to the following equation:

$$F_s = -k_s \delta_s \cdot \mathbf{t}_s - \eta_s \mathbf{u}_s \cdot \mathbf{t}_s \tag{2.37}$$

where $k_s = 8Gb(t)$ is the tangential stiffness coefficient [30], η_s is a damping coefficient. The particle tangential displacement is given by:

$$\delta_s = \int_{t_0}^{t} \mathbf{u}_s(\tau) \cdot \mathbf{t}_s \, d\tau \tag{2.38}$$

where t_0 is the time marking the beginning of the impact. The above equations are valid up to a critical value of the magnitude of the tangential force F_s^{crit}. Once this threshold has been exceeded, the system enters in a condition of dynamic friction.

The twisting motion is similar, but the spheres rotates at different rate in a direction along the normal vector connecting their centers. Therefore, the slip velocity is nil at the center of the contact region, and it increases linearly within the contact region with distance from the contact point. The resistance opposed by the sphere to twisting motion is a twisting torque oriented parallel to the normal vector. The twisting resistance is modelled analogously to the sliding resistance. Being k_t the tortional stiffness coefficient, η_t the dissipation coefficient, and Ω_t the relative twisting rate of the two colliding spheres along the normal direction, the twisting resistance torque is defined as:

$$M_t = -k_t \int_{t_0}^{t} \Omega_t(\tau) d\tau - \eta_t \Omega_t \tag{2.39}$$

The slip starts at the outer edge of the contact region and progress toward its center as long as the twisting moment increases, up to the reaching of a critical value [31].

Rolling occurs when spheres rotate and translate in such a way that they move tangentially relative to each other with no slipping occurring. Given the rolling velocity $\mathbf{u}_r$ distinguished from other types of motion, a spring-dashpot-model similar to the model for sliding resistance has been proposed [32]. The rolling displacement ξ_r is defined as:

$$\xi_r = \int_{t_0}^{t} \mathbf{u}_r(\tau) \cdot \mathbf{t}_r d\tau \tag{2.40}$$

where $\mathbf{t}_r$ is the rolling direction. Together with the rolling stiffness coefficient η_r and the rolling damping coefficient η_r, it contributes to define the rolling torque M_r as:

$$M_r = -k_r \xi_r - \eta_r \mathbf{u}_r \cdot \mathbf{t}_r \tag{2.41}$$

This equation describes the rolling torque up to the reaching of a critical value. Beyond the threshold, the rolling torque magnitude is supposed to be equal to the critical value.

The effect of adhesion on tangential interactions can also be considered. For small adhesive particles, the relevance of sliding and twisting is reduced, and therefore simple expressions can be used to take them into account. Thornton and Yin [33, 34] proposed a model based on the spring-dashpot-model by Cundall and Strack for non-adhesive particles. In this model, the sliding force F_s is described by Eq. 2.37 when $|F_s| < F_s^{crit}$, and by $F_s = -F_s^{crit}$ when $|F_s| \geq F_s^{crit}$, where the value of the critical sliding force is related to the normal interacting force. The influence of adhesion can be taken into account by simply implementing the pull-off force F_{po} in the expression for the critical value of the sliding force:

$$F_s^{crit} = \mu_F |F_n + 2F_{po}| \tag{2.42}$$

where μ_F is a friction coefficient.

Analogous considerations can be made when it comes to twisting resistance. F_t^{crit} is again $\mu_F |F_n + 2F_{po}|$ as in Eq. 2.42, and it is used to calculate the critical twisting torque:

$$M_t^{crit} = \frac{3}{16} \pi b F_t^{crit} \tag{2.43}$$

The simple extension of the Cundall-Strack model to the adhesive case by redefining the critical force is not valid for rolling, as the asymmetry of the stress distribution due to the adhesive force is the principal physical mechanism underlying

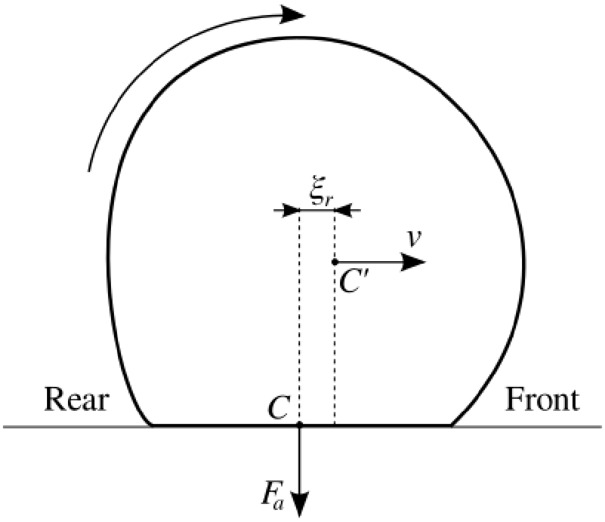

Fig. 2.6 Adhesive sphere rolling on a planar surface. The asymmetry in the contact region due to the necking occurring in the rear side of the particle makes the centroid C' moves ahead of the centroid of the contact region C. The lag between their horizontal positions is the rolling displacement ξ_r.

rolling resistance. A simple model for adhesive rolling resistance has been derived by Dominik and Thielens [35]. Let's consider a simple system constituted by an adhesive particle in contact with a plane, although the following considerations would fit any two spheres colliding. When the sphere is not rolling, the stress distribution predicted by the JKR model is symmetric about the contact point, i.e., the point on the contact surface directly below the particle centroid. When the sphere starts rolling, the situation depicted in Fig. 2.6 is realized. As can be seen, the material points of the particle on the front side continually jump on a state of contact with the planar surface, whereas the points on the rear side are continually pulled off. According to JKR theory, the jump-on occurs when the normal overlap δ_N is 0, while pull-off is delayed due to necking and occurs at $\delta_N = -\delta_{po}$. This gives rise to an asymmetry in the contact region: in the rear side, the particle remains in contact with the planar surface for a longer time, causing the rise of the rolling displacement ξ_r, i.e., the distance between the horizontal position of the centroid C' and the horizontal position of the center of the contact region C. The rolling resistance torque M_r is the product of the adhesive force $F_a = 4F_{po}\left(b/b_0\right)^{3/2}$ and the rolling displacement ξ_r. Therefore, the adhesive force F_a can be interpreted as a rolling coefficient k_r, and the rolling resistance torque can be defined as:

$$M_r = -k_r \xi_r \tag{2.44}$$

When a particle starts rolling, the contact region stays fixed because of the resistance opposed by M_r until a critical rolling displacement ξ_r^{crit} is reached. Then, the particle starts rolling, keeping a horizontal displacement ξ_r^{crit} between O and C. In other words, $M_r = -k_r \xi_r^{crit}$ for $\xi_r \geq \xi_r^{crit}$. The rolling displacement is calculated from the rolling velocity $\mathbf{u}_r$ in a similar fashion to Eq. 2.40. The critical rolling displacement can also be expressed in terms of a critical rolling angle ϕ_r^{crit} as:

$$\phi_r^{crit} = \xi_r^{crit} / a \tag{2.45}$$

2.2 DEM modelling for spray drying

The spray drying process was examined by a discrete element method able to accurately track the motion of each single colloidal particle. The motion dynamics of the particles was modelled through the open-source software *Yade*, appropriately modified to take into account the relevant forces acting on the particles, or bodies, during the shrinkage of the droplet, namely the capillary force, the Brownian force and the adhesive forces acting on the particles.

In *Yade*, bodies move through the simulation space and interact with each other. During a single iteration loop, the forces acting on each body are resetted, interactions between bodies are updated and the detection of new collisions begins. New interactions are defined and characterized, and forces acting on bodies are calculated using constitutive laws based on displacements. Finally, Newton's second law is used to calculate acceleration of bodies, and velocity and position of each body are updated. Time is increased by a fixed timestep Δt and a new iteration loop begins [36]. The main steps of the simulation loop are summarized in Fig. 2.7.

2.2.1 Contact forces

Particles are rigid but a certain overlap is allowed: under the hypotesis that deformation occurs only in a small region, the overlap is used to model interaction forces [37]. A normal stiffness k_N is calculated using Eq. 2.46: this stiffness is analogous to the stiffness of two springs in serial configuration with lengths equal to the sphere radii and it is related to the elastic modulus E of the bodies, as highlighted in Fig. 2.8. The equation is obtained considering the change of distance between the sphere centers as distributed onto deformations of both spheres, proportionally to their compliances. The displacement generates forces proportional to the stiffness.

$$k_N = \frac{2E_i a_i E_j a_j}{E_i a_i + E_j a_j} \tag{2.46}$$

A sliding stiffness k_s (or shear stiffness) is defined as a fraction of k_N. The following relation between inter-particle forces and the friction coefficient $\tan(\phi_c)$, where ϕ_c is the contact friction angle, has to be true [38]:

$$||\mathbf{F}_s|| \leq ||\mathbf{F}_n \tan(\phi_c)|| \tag{2.47}$$

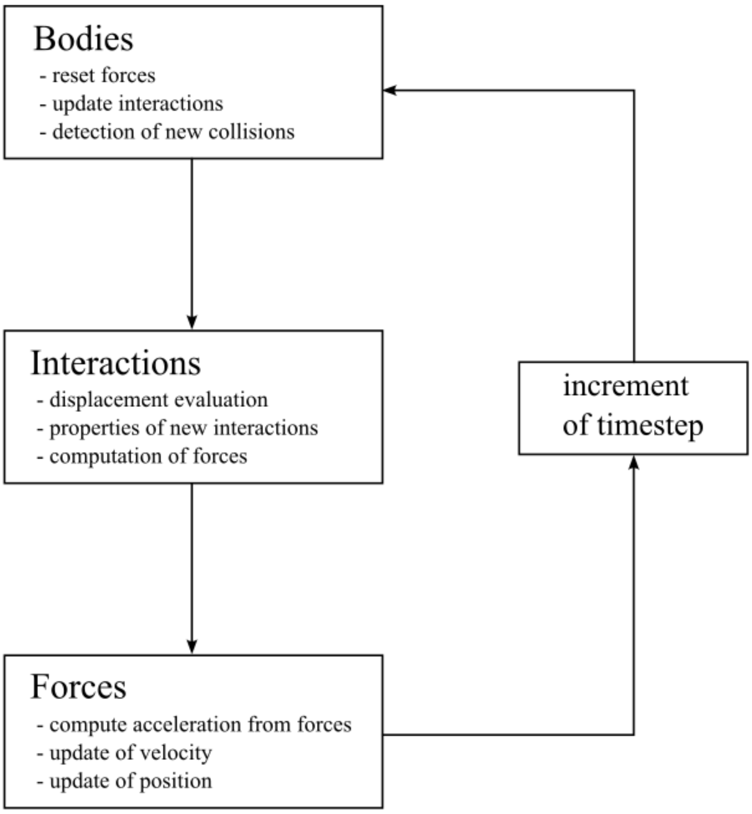

Fig. 2.7 Simulation loop in *Yade*.

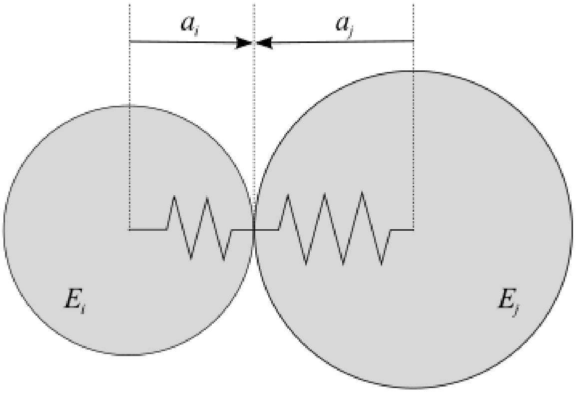

Fig. 2.8 Contact between the sphere i with radius a_i and elastic modulus E_i, and sphere j with radius a_j and elastic modulus E_j. The normal stiffness is analogous to the stiffness of two springs in serial configuration with lengths equal to the sphere radii.

As already mentioned in Section 2.1.1 (Fig. 2.2), the modes of spheres interaction are normal displacement, sliding, twisting and rolling. Normal displacement originates from the relative linear velocity of the particles along the interaction axis, described by the unit vector **n**; sliding is caused by the relative linear velocity perpendicular to **n**; twisting originates from the relative rotational velocity component parallel with **n**; rolling is caused by the relative rotational velocity component perpendicular to **n**. The principal components of the relative movement are the normal deformation and the shear deformation. The normal deformation is characterized by the overlap δ_N, the difference between the sum of the radii of the spheres and the distance of their centers or, in another view, the displacement of the initial contact point in the normal direction. Shear displacement $\vec{\delta_s}$ describes tangential interaction and is the component of the displacement of the initial contact point which is perpendicular to the contact line.

Every interaction is characterized by kinematic variables that are used to calculate the forces acting on the two spheres using constitutive laws. The forces are calculated accordingly to the selected contact model: the simplest contact model available in *Yade* is a non-cohesive elastic-frictional contact model based on the work by Cundall and Strack [29]. Properties of the material such as density, elastic modulus, etc. are defined, and when a new contact is detected, the interaction is created and related variables such as normal stiffness k_N, shear stiffness k_s and contact friction angle ϕ_c are computed on the basis of the material associated to the bodies [38]. At each step, displacements δ_N and δ_s are computed. If $\delta_N > 0$ the interaction is cancelled, otherwise the normal force $\mathbf{F}_n$ and a *trial* shear force $\mathbf{F}_s^t$ are calculated as follows:

$$\mathbf{F}_n = k_N \delta_n \mathbf{n} \tag{2.48}$$

$$\mathbf{F}_s^t = k_s \boldsymbol{\delta}_s \tag{2.49}$$

$\mathbf{F}_s = \mathbf{F}_s^t$ if $|\mathbf{F}_s^t| \leq |\mathbf{F}_n| \tan(\phi_c)$, otherwise the adjusted value for the shear force is $\mathbf{F}_s = \mathbf{F}_s^t \frac{|\mathbf{F}_n| \tan(\phi_c)}{|\mathbf{F}_s^t|}$. The total force $\mathbf{F} = \mathbf{F}_n + \mathbf{F}_s$ is applied at the contact point, so it generates torques as shown in Eq. 2.50 and 2.51.

$$\mathbf{M}_1 = \bar{d_1}(-\mathbf{n}) \times \mathbf{F} \tag{2.50}$$

$$\mathbf{M}_2 = \bar{d_2}\,\mathbf{n} \times \mathbf{F} \tag{2.51}$$

Additional forces arise from the binary interactions between the primary particles at contact. Besides the elastic-frictional model previously described, a cohesive normal force has been set, which was estimated according to the Johnson-Kendall-Roberts (JKR) theory of contact mechanics as [39]:

$$F_{coh} = F_{po} = \frac{3}{2} \pi \gamma_s a \tag{2.52}$$

where γ_s is the superficial energy of the monomers[2], and where the first equality states that the cohesive force equals the pull-off force F_{po} required to break the bond between the two particles. It should be noticed that Eq. 2.52 is equivalent to Eq. 2.35, because the radius in the latter equation is an *effective* radius, equal to $a/2$ for spheres of the same size.

2.2.2 Hydrodynamics forces and Brownian motion

Besides the forces arising from the particle-particle interactions, forces exerted by the fluid on the suspended particles are modelled as well. Viscous force and torque acting on the particles were considered according to the free–draining approximation, thus assuming that every particle interacts with the surrounding fluid as if it were alone in the system, i.e., neglecting all fluid-mediated particle-particle interactions [40–43]. Consequently, the viscous force acting on a single primary particle reduces

---

[2] If the particles are surrounded by a liquid, γ_s is the interfacial liquid-solid energy.

to the Stokes drag force:

$$\mathbf{F}_{drag} = -6\pi\mu_l a(\dot{\mathbf{x}}_p - \dot{\mathbf{x}}_l) \tag{2.53}$$

where μ_l is the liquid viscosity, a the radius of the primary particle, $\dot{\mathbf{x}}_p$ the linear velocity of the particle and $\dot{\mathbf{x}}_l$ the linear velocity of the liquid at the particle coordinates, which, under the condition of stagnant fluid, is equal to zero. Drag torque calculations are similar, but rotational velocities $\boldsymbol{\omega}$ are required:

$$\boldsymbol{T}_{drag} = -8\pi\mu_l a^3(\boldsymbol{\omega}_p - \boldsymbol{\omega}_l) \tag{2.54}$$

Brownian effects were taken into account, in order to capture the diffusion of the primary particles in the medium. To this aim, the Brownian force acting on a particle was implemented as follows [44]:

$$\mathbf{F}_{brown} = \sqrt{\frac{24 k_b T \cdot 6\pi\mu_l a}{\Delta t}} \cdot \boldsymbol{\chi} \tag{2.55}$$

where k_b is the Boltzmann constant, Δt is the fixed timestep between iterations and $\boldsymbol{\chi}$ is a three-elements vector where each element is a random number drawn at each iteration from a uniform distribution between -0.5 and $+0.5$. Brownian torque calculations are analogous and are based on the following equation:

$$\boldsymbol{T}_{brown} = \sqrt{\frac{24 k_b T \cdot 8\pi\mu_l a^3}{\Delta t}} \cdot \boldsymbol{\chi} \tag{2.56}$$

All other fluid-particle of particle-particle interactions are neglected, including colloidal van der Waals or double layer forces.

2.2.3 Integration of motion

Forces and torques acting on particles are employed to integrate motion equations by using the second order leapfrog method. These equations are solved individually for each particle, so the following steps will be referred to the integration of motion for a single sphere. According to the definitions given in Section 2.2.1, if $\mathbf{x}_i$ is the position of a particle at a certain time t_i, $\mathbf{x}_{i+1}$ is the position of the particle at time $t_{i+1} = t_i + \Delta t$. The value is updated using the acceleration $\ddot{\mathbf{x}}_i$ computed from the total force $\mathbf{F}$ acting on the particle and its mass m (Eq. 2.57).

$$\ddot{\mathbf{x}}_i = \mathbf{F}/m \tag{2.57}$$

Acceleration can be expressed with a 2nd order finite difference, obtaining:

$$\ddot{\mathbf{x}}_i \cong \frac{\mathbf{x}_{i-1} - 2\mathbf{x}_i + \mathbf{x}_{i+1}}{\Delta t^2} \tag{2.58}$$

$$\mathbf{x}_{i+1} = \mathbf{x}_i + \Delta t \left(\frac{\mathbf{x}_i - \mathbf{x}_{i-1}}{\Delta t} + \ddot{\mathbf{x}}_i \Delta t \right) \tag{2.59}$$

Informations about the value of $\mathbf{x}_{i-1}$ have already been lost. However, if one uses the approximation described by Eq. 2.60, Eq. 2.59 changes into Eq. 2.61.

$$\dot{\mathbf{x}}_{i-1/2} \simeq \frac{\mathbf{x}_i - \mathbf{x}_{i-1}}{\Delta t} \tag{2.60}$$

$$\mathbf{x}_{i+1} \simeq \mathbf{x}_i + \Delta t \left(\dot{\mathbf{x}}_{i-1/2} + \ddot{\mathbf{x}}_i \Delta t \right) \tag{2.61}$$

The term between brackets in Eq. 2.61 is an approximation for the current mean velocity $\dot{\mathbf{x}}_{i+1/2}$:

$$\dot{\mathbf{x}}_{i+1/2} \simeq \dot{\mathbf{x}}_{i-1/2} + \ddot{\mathbf{x}}_i \Delta t \tag{2.62}$$

Firstly, the algorithm computes the value of the current mean velocity $\dot{\mathbf{x}}_{i+1/2}$ (Eq. 2.62), which will be stored and used as $\dot{\mathbf{x}}_{i-1/2}$ in the next step; then, the position $\mathbf{x}_{i+1}$ is calculated (Eq. 2.63). It is worth to notice that positions $\mathbf{x}$ are known at times $i\Delta t$, while velocities $\dot{\mathbf{x}}$ are known at times $(i+1/2)\Delta t$.

$$\mathbf{x}_{i+1} = \mathbf{x}_i + \dot{\mathbf{x}}_{i+1/2} \Delta t \tag{2.63}$$

The particle orientation $\mathbf{q}_i$ is updated in a similar manner. For spherical objects, the inertia tensor is diagonal in every orientation, i.e., $I_{11} = I_{22} = I_{33}$. Therefore, the current angular acceleration $\dot{\boldsymbol{\omega}}_i$ can be computed if current torque $\mathbf{T}$ is known.

$$\dot{\boldsymbol{\omega}}_i = \frac{\mathbf{T}}{I_{11}} \tag{2.64}$$

The value of $\boldsymbol{\omega}_{i+1/2}$ is obtained with an equation similar to Eq. 2.62.

$$\boldsymbol{\omega}_{i+1/2} = \boldsymbol{\omega}_{i-1/2} + \dot{\boldsymbol{\omega}}_i \Delta t \tag{2.65}$$

The rotation vector is a quaternion defined as $\Delta\mathbf{q} = \boldsymbol{\omega}_{i+1/2}\Delta t$. Finally, the next orientation $\mathbf{q}_{i+1}$ can be computed as:

$$\mathbf{q}_{i+1} = \mathbf{q}_i + \Delta\mathbf{q} \tag{2.66}$$

The critical, fixed timestep Δt_{cr} for the stability of the explicit integration method is calculated as follows. The properties of the material has to be defined, such as density ρ_p and the elastic modulus E. Explicit integration schemes are employed and critical timestep calculations are based on sonic speed $\sqrt{E/\rho_p}$.

$$\Delta t_{cr} = a\sqrt{\frac{\rho_p}{E}} \tag{2.67}$$

in Equation 2.67 the timestep is defined in such a way that the elastic wave does not propagate farther than the minimum distance of integration points in a single step. This distance can be identified as the sphere's radius a because it is the minimum distance between two objects, if the two objects are the sphere and a facet.

The computational time Z increases linearly with the number of monomers. Also, computational time increases if the monomers are smaller, because in that case the computed timestep between iterations would be smaller. In particular, Z varies linearly with the radius of particles a. For a fixed domain volume V and a fixed simulated time ζ, Z roughly depends on the number of simulation steps n_{step}, on the number of particles np an on the number of computational cores n_{CPU}. Some of these variables can be related to the particle radius a as follows:

- The number of simulation steps n_{step} (Eq. 2.68) depends on the choice of the critical timestep Δt_{cr}, estimated by p-wave velocity. s_t is the timestep safety factor.

$$n_{step} = \frac{\zeta}{s_t \Delta t_{cr}} = \frac{\zeta}{s_t a}\sqrt{\frac{E}{\rho_p}} \tag{2.68}$$

- For a certain value p_{pack} of packing porosity, the number of particles np can be estimated as:

$$np = p_{pack}\frac{V}{\frac{4}{3}\pi a^3} \tag{2.69}$$

So the computational cost can be roughly estimated as $Z \propto a^{-1}a^{-3} \propto a^{-4}$. It has to be noticed that this relation is obtained for a fixed simulation volume: if other parameters are allowed to vary, the proportionality between the computational time and the particle radius can be different. The *Yade* code used for the simulation of the spray drying of a single droplet is given in Appendix A.

2.3 DEM modelling for breakup

The approach described in Section 2.2 is focused on the agglomeration of clusters, i.e., on their formation via spray drying. In that case, the role of fluid dynamic forces was minor in comparison to the capillary effect of the shrinking interface, and also highly accurate modelling of contact mechanics was not required, because adhesive forces were so strong to freeze the configuration of the growing aggregate after every contact. The de-agglomeration of the clusters provoked by viscous forces is equally important for the proposed case study. Agglomerates are in fact required to break up in the proximity of the occlusion, where large shear stresses hold. In this case, beside the intensity of the shearing force which is determinant in inducing dispersion, a key role is played also by the spatial arrangement of the primary particles within the agglomerate, which strongly affects the distribution of the mechanical stress in the network of contacting particles, the breakup occurrence and consequently the fragment size distribution [40, 45–47]. The study of the agglomerate rupture due to viscous stresses, performed by an in-house code, required two improvements in the DEM compared to the model used for simulating the spray drying process. Firstly, the viscous forces, which are responsible for breakage, had to be predicted accurately. The free–draining approximation, used in the first part of the work because of its favorable computational cost, neglects in fact fluid-mediated particle-particle interactions, which are known to strongly influence the way agglomerates undergo restructuring and breakup [48, 49]. Secondly, in this case, it was necessary to accurately compute and track the distribution of the mechanical stresses within the agglomerate structure, in order to ascertain if the critical stress inducing fracture is reached at any particle-particle contact. This effect was largely neglected in the first part of the work, i.e., the formation of rigid clusters of particles, in which the spatial configuration of the particles was seen to be frozen after contact. In the second part of the work, for rigorously addressing the deagglomeration phenomenon, Stokesian dynamics (SD) approach was adopted [46, 50–53]. The method allows to accurately predict the hydrodynamic stress, coupled with proper models for describing the colloidal particle-particle interactions [47, 54].

2.3.1 Stokes equations

The system of interest is made by spherical particles dispersed in a Newtonian fluid. Particles can be linked by van der Waals forces, constituting agglomerates. The hydrodynamic force exerted by the fluid can induce modifications in the particle-particle bonds, and even their breakup. The problem is characterized by resorting to Navier-Stokes equations for incompressible and Newtonian fluids. In a dimensionless form:

$$\nabla^* \cdot \mathbf{u}^* = 0 \tag{2.70}$$

$$St\frac{\partial \mathbf{u}^*}{\partial t^*} + Re\,\mathbf{u}^* \cdot \nabla^* \mathbf{u}^* = -\nabla^* p^* + \nabla^{*2} \mathbf{u}^* \tag{2.71}$$

If μ_l is the dynamic viscosity of the fluid and L, $\tilde{T}$ and $\tilde{U}$ are representative of a characteristic length, time and velocity of the considered system, the dimensionless quantities in Eq. 2.70 and 2.71 are defined as:

- $\nabla^* = L\nabla$
- $\mathbf{u}^* = \mathbf{u}/\tilde{U}$
- $t^* = t/\tilde{T}$
- $p^* = pL/(\mu_l \tilde{U})$

The Reynolds number Re and the Stokes number St are two fundamental dimensionless numbers characterizing the investigated system, defined as:

$$Re = \frac{\rho_l \tilde{U} L}{\mu_l} \quad ; \quad St = \frac{L^2}{\tilde{T} \nu_l} \tag{2.72}$$

ρ_l is the fluid density, $\nu_l = \mu_l/\rho_l$ is its kinematic viscosity.

For $L = a$, Reynolds and Stokes number are referred to particles and are called Re_p and St_p respectively. In the investigated system, the radius a of particles is small, so it is valid the assumption of $Re_p \ll 1$ and $St_p \ll 1$. Moreover, by assuming $\tilde{T} = a/\tilde{U}$, it can be noticed that $Re_p = St_p$. Under the discussed hypotheses, the creeping flow condition is realized: the inertial and the acceleration terms in Eq. 2.71

are negligible and one is therefore able to write Eq. 2.70 and 2.71 as the following Stokes equations. This is known as the *Stokes approximation*.

$$\nabla \cdot \mathbf{u} = 0 \tag{2.73}$$

$$0 = -\nabla p + \mu_l \nabla^2 \mathbf{u} \tag{2.74}$$

Stokes equations are *time-independent*, are *linear* with respect to **u**, and are *reversible*, i.e., $(-p, -\mathbf{u})$ is a solution of the equation if $(p, \mathbf{u})$ is a solution as well [55].

Eq. 2.73 and 2.74 define a flow field exerting a hydrodynamic force and torque on the particles. Colloidal interactions between particles are also taken into consideration, while Brownian motion is neglected, as will be discussed in the next sections. Particles' inertia is supposed to be negligible, and therefore forces acting on particles must balance each other. Hydrodynamic force and torque are balanced by the colloidal and contact forces and torques for every particle in the system, as described by Eq. 2.75.

$$\begin{cases} \mathbf{F}^{hydro} = -\mathbf{F}^{cont} \\ \mathbf{T}^{hydro} = -\mathbf{T}^{cont} \end{cases} \tag{2.75}$$

The complete solution of the Stokes equation and the subsequent calculation of forces and torques would require a notable computational cost. However, a different approach can be employed to calculate the hydrodynamic forces exerted by the fluid on particles and agglomerates. Stokesian Dynamics is an approach that uses a truncated multipole expansion of the rigorous solution of the Stokes equations for long-range interactions, while short-range interactions between particles are modelled using the lubrication theory. In this way, Stokesian dynamics is able of accurately simulate the hydrodynamic interactions at a reasonable computational cost [56, 57].

2.3.2 Single particle in Stokes regime

In this section, the equations governing the behaviour of a fixed, single, spherical particle in Stokes regime are shown [58]. The velocity of the undisturbed flow field $\mathbf{u}^\infty$ at the generic location **x** can be written as a 1^{st} order Taylor expansion centered

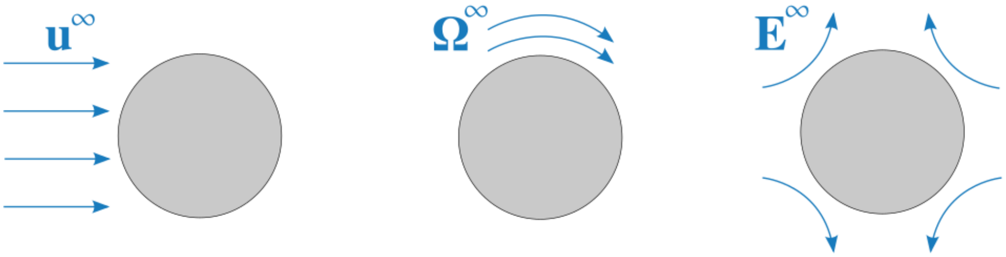

Fig. 2.9 Single particle in Stokes regime. Left: particle immersed in a uniform flow field. Middle: particle immersed in a pure rotating flow field. Right: particle immersed in a pure straining flow field.

in $\mathbf{x}_0$:

$$\mathbf{u}^\infty(\mathbf{x}) \approx \mathbf{u}^\infty(\mathbf{x}_0) + \nabla\mathbf{u}^\infty(\mathbf{x}_0) \cdot (\mathbf{x} - \mathbf{x}_0) \tag{2.76}$$

Eq. 2.76 is sufficiently accurate if the difference between $\mathbf{x}$ and $\mathbf{x}_0$ is small. Let's center the reference system in $\mathbf{x}_0$: if $\mathbf{u}^\infty(\mathbf{x}_0)$ is re-written as $\mathbf{u}^\infty$ for brevity, and if the velocity gradient $\nabla\mathbf{u}^\infty(\mathbf{x}_0)$ is decomposed in an antisymmetric and a symmetric part, Eq. 2.77 is obtained.

$$\mathbf{u}^\infty(\mathbf{x}) = \mathbf{u}^\infty + \Omega^\infty \cdot \mathbf{x} + \mathbf{E}^\infty \cdot \mathbf{x} \tag{2.77}$$

Ω^∞ and $\mathbf{E}^\infty$ are the rate-of-rotation and rate-of-strain tensors. As previously mentioned, Stokes equation is linear: therefore, the behaviour of a single particle in a generic flow field can be thought as the superposition of a uniform flow field $\mathbf{u}^\infty$, a rotating flow field $\Omega^\infty \cdot \mathbf{x}$ and a straining flow field $\mathbf{E}^\infty \cdot \mathbf{x}$. A visual representation of the three types of flow field has been given in Figure 2.9. The overall effect of the flow field on the particle is the sum of the effect of every single type of flow field.

The effect of the uniform flow field on an immersed spherical particle is obtained by imposing a no-slip condition at the particle surface, and prescribing that the flow field is undisturbed at large distance from the particle. The solution of the problem leads to some considerations: the particle causes a slowly-decaying distortion of the uniform flow field, therefore another particle in the system would be influenced by the presence of the first particle even for a relatively long distance. Moreover, Eq. 2.78 arises from the integration of the stress tensor over the particle surface, and allows one to calculate the hydrodynamic force exerted by the fluid on the particle.

$$\mathbf{F}^{hydro} = 6\pi\mu_l a\,\mathbf{u}^\infty \tag{2.78}$$

As mentioned above, the particle has been supposed to be fixed, but this result can be extended to the case of a particle moving at velocity $\mathbf{u}_p$. The inertia is negligible in Stokes regime, therefore it is easy to switch to a reference frame moving with the particle. Solving the problem in this reference frame and then getting back to a fixed reference frame, Eq. 2.79 is obtained.

$$\mathbf{F}^{hydro} = 6\pi\mu_l a(\mathbf{u}^\infty - \mathbf{u}_p) \tag{2.79}$$

Let us consider the case in which the particle is immersed in a pure rotating flow field, i.e., the only velocity associated to the fluid is the rotational velocity $\boldsymbol{\omega}^\infty$. If boundary conditions analogous to the ones discussed for the uniform flow field are imposed, the following results are obtained: the influence of the particle on the surrounding flow field decays faster; the hydrodynamic force exerted by the fluid on the particle is zero because of the intrinsic symmetry of the problem; a hydrodynamic torque arises, and it can be calculated by resorting to Eq. 2.80:

$$\mathbf{T}^{hydro} = 8\pi\mu_l a^3(\boldsymbol{\omega}^\infty - \boldsymbol{\omega}_p) \tag{2.80}$$

where $\boldsymbol{\omega}_p$ is the rotational velocity of the particle.

At this point, let us consider a particle immersed in a pure straining flow field. In this case, both the net force and torque are null. The resistance opposed by the particle to the straining component of the flow, i.e., the stresslet, can be calculated in index notation as:

$$S_{ij} = \frac{20}{3}\pi\mu_l a^3 E_{ij}^\infty \tag{2.81}$$

Another notable case is represented by a particle freely moving in a pure shear flow, i.e., the velocity of the fluid linearly changes along a direction, following the law $\mathbf{u}^\infty = (0, 0, \dot{\gamma}y)$, where $\dot{\gamma}$ is the shear rate. The flow is obtained by combining the contribution of a rotating and a straining component, as shown in Eq. 2.82, 2.83 and 2.84.

$$\mathbf{u}^\infty(\mathbf{x}) = \Omega^\infty \cdot \mathbf{x} + \mathbf{E}^\infty \cdot \mathbf{x} \tag{2.82}$$

$$\Omega^{\infty} = \frac{1}{2}\begin{bmatrix} 0 & 0 & 0 \\ 0 & 0 & -\dot{\gamma} \\ 0 & \dot{\gamma} & 0 \end{bmatrix} \tag{2.83}$$

$$\mathbf{E}^{\infty} = \frac{1}{2}\begin{bmatrix} 0 & 0 & 0 \\ 0 & 0 & \dot{\gamma} \\ 0 & \dot{\gamma} & 0 \end{bmatrix} \tag{2.84}$$

According to Eq. 2.79 and 2.80, the relative linear and angular velocity of a particle immersed in the fluid is proportional to the force and the torque exerted by the fluid on the particle, respectively. Moreover, hydrodynamic force and torque counter-balance the remaining forces and torques acting on the particle (Eq. 2.75). The relation between hydrodynamic forces exerted by a known flow field and the motion of the suspended particle α can be expressed by the following linear system:

$$\begin{bmatrix} a' & 0 & 0 & 0 & 0 & 0 & 0 & 0 & 0 & 0 & 0 \\ 0 & a' & 0 & 0 & 0 & 0 & 0 & 0 & 0 & 0 & 0 \\ 0 & 0 & a' & 0 & 0 & 0 & 0 & 0 & 0 & 0 & 0 \\ 0 & 0 & 0 & b' & 0 & 0 & 0 & 0 & 0 & 0 & 0 \\ 0 & 0 & 0 & 0 & b' & 0 & 0 & 0 & 0 & 0 & 0 \\ 0 & 0 & 0 & 0 & 0 & b' & 0 & 0 & 0 & 0 & 0 \\ 0 & 0 & 0 & 0 & 0 & 0 & 2c' & 0 & 0 & 0 & c' \\ 0 & 0 & 0 & 0 & 0 & 0 & 0 & 2c' & 0 & 0 & 0 \\ 0 & 0 & 0 & 0 & 0 & 0 & 0 & 0 & 2c' & 0 & 0 \\ 0 & 0 & 0 & 0 & 0 & 0 & 0 & 0 & 0 & 2c' & 0 \\ 0 & 0 & 0 & 0 & 0 & 0 & c' & 0 & 0 & 0 & 2c' \end{bmatrix} \left\{ \begin{matrix} F_x^{ext} \\ F_y^{ext} \\ F_z^{ext} \\ T_x^{ext} \\ T_y^{ext} \\ T_z^{ext} \\ S_{xx} \\ S_{xy} \\ S_{xz} \\ S_{yz} \\ S_{yy} \end{matrix} \right\} = \left\{ \begin{matrix} u^{\infty}(x^{\alpha}) - u_x^{\alpha} \\ u^{\infty}(y^{\alpha}) - u_y^{\alpha} \\ u^{\infty}(z^{\alpha}) - u_z^{\alpha} \\ \omega_x^{\infty} - \omega_x^{\alpha} \\ \omega_y^{\infty} - \omega_y^{\alpha} \\ \omega_z^{\infty} - \omega_z^{\alpha} \\ E_{xx}^{\infty} - E_{zz}^{\infty} \\ 2E_{xy}^{\infty} \\ 2E_{xz}^{\infty} \\ 2E_{yz}^{\infty} \\ E_{yy}^{\infty} - E_{zz}^{\infty} \end{matrix} \right\} \tag{2.85}$$

where:

$$a' = \frac{1}{6\pi\mu_l a} \quad ; \quad b' = \frac{1}{8\pi\mu_l a^3} \quad ; \quad c' = \frac{3}{20\pi\mu_l a^3}$$

Tensors **S** and $\mathbf{E}^{\infty}$, symmetric and traceless, are reduced to the equivalent five-component column vectors:

- $\mathbf{S} = (S_{xx}, S_{xy}, S_{xz}, S_{yz}, S_{yy})$
- $\mathbf{E}^{\infty} = \left(E_{xx}^{\infty} - E_{zz}^{\infty}, 2E_{xy}^{\infty}, 2E_{xz}^{\infty}, 2E_{yz}^{\infty}, E_{yy}^{\infty} - E_{zz}^{\infty}\right)$

The 11×11 matrix is the *mobility matrix* for a particle immersed in a flow field.

2.3.3 Multi-particle system

Eq. 2.85 can be easily extended to a colloidal suspension composed by np particles, resulting in a $11np \times 11np$ mobility matrix, i.e., $11np$ independent equations. If particles do not hydrodynamically interact with each other, the approach is referred to as the free-draining approximation.

However, it is possible to go further and take into consideration the hydrodynamic interactions between the particles suspended in the fluid. Faxén laws evaluate force, torque and stresslet acting on each suspended particle taking into account the disturbance that other particles exert on the flow field [58, 59]. The flow field disturbance u_i' is the difference between the disturbed flow field and the flow field if no other particles were suspended in the fluid. In index notation, it is $u_i'(\mathbf{x}) = u_i(\mathbf{x}) - u_i^\infty(\mathbf{x})$. Faxén laws for force, torque and stresslet are the following:

$$F_i^\alpha = 6\pi\mu_l a\left[-\left(1+\frac{a^2}{6}\nabla^2\right)u_i'(\mathbf{x}^\alpha) + (u_i^\alpha - u_i^\infty(\mathbf{x}^\alpha))\right] \tag{2.86}$$

$$T_i^\alpha = 8\pi\mu_l a^3\left[-\frac{1}{2}\varepsilon_{ijk}\nabla_j u_k'(\mathbf{x}^\alpha) + (\omega_i^\alpha - \omega_i^\infty(\mathbf{x}^\alpha))\right] \tag{2.87}$$

$$S_{ij}^\alpha = \frac{20}{3}\pi\mu_l a^3\left[-\left(1+\frac{a^2}{10}\nabla^2\right)E_{ij}'(\mathbf{x}^\alpha) + (-E_{ij}^\infty)\right] \tag{2.88}$$

ε_{ijk} is the Levi-Civita operator. If the disturbance is equal to zero, Eq. 2.79, 2.80 and 2.81 referred to the particle α are re-obtained.

Eq. 2.86, 2.87 and 2.88 still require a model for the disturbed flow field, in order to get a closure. Considering the case of a particle fixed in a uniform flow field, the combination of the velocity field solution with Eq. 2.78 in the limit $a \to 0$ results in the point-force solution of the Stokes equation, the *Stokeslet*.

$$u_i^{PF} = J_{ij} \cdot \frac{F_i^{hydro}}{8\pi\mu_l} \tag{2.89}$$

where J_{ij} is the Oseen-Burgers tensor, or stokeslet propagator (Eq. 2.90).

$$J_{ij} = \left(\frac{\delta_{ij}}{r} + \frac{x_i x_j}{r^3} \right) \tag{2.90}$$

Following a similar procedure, the solution for the point-torque and point-stresslet is obtained (Eq. 2.91 and 2.92) and expressed through the associated propagator tensor, R_{ij} and K_{ijk} respectively.

$$u_i^{PT} = \frac{1}{8\pi\mu_l} \frac{\varepsilon_{ijk} T_j^{hydro} r_k}{r^3} = R_{ij} \frac{T_j^{hydro}}{8\pi\mu_l} \tag{2.91}$$

$$u_i^{PS} = -\frac{1}{8\pi\mu_l} \frac{3x_i x_j x_k S_{jk}}{r^5} = K_{ijk} \frac{S_{jk}}{8\pi\mu_l} \tag{2.92}$$

Thanks to these equations, it is possible to extract the solution of the Stokes flow for a certain distribution of forces f_j as the superposition of the flow fields individually generated by each force, as expressed by the following equation:

$$u_i(\mathbf{x}) = u_i^{\infty}(\mathbf{x}) - \frac{1}{8\pi\mu_l} \sum_{\alpha=1}^{np} \int_{S_\alpha} J_{ij}(\mathbf{x}-\mathbf{y}) f_j(\mathbf{y}) dS_y \tag{2.93}$$

The point of application of each differential force is indicated by the vector $\mathbf{y}$. Eq. 2.93 is not explicitly solved by the Stokesian dynamics approach, wich instead focuses on a multipole expansion of the flow field about the center of the particle α. The n-th moment of this expansion reads as:

$$M_n^{\alpha} = -\int_{S_\alpha} (y_i - x_i^{\alpha})^n f_j(\mathbf{y}) dS_y \tag{2.94}$$

The zero moment, obtained by imposing $n = 0$, is the total force exerted by the particle on the fluid; The first moment ($n = 1$) can be decomposed in an antisymmetric component related to torque, and a symmetric component related to stresslet. The multipole expansion is then written as:

$$u_i'(\mathbf{x}) = u_i(\mathbf{x}) - u_i^{\infty}(\mathbf{x}) = \frac{1}{8\pi\mu_l} \sum_{\alpha=1}^{np} \left(1 + \frac{1}{6} a^2 \nabla^2\right) J_{ij} F_j^{\alpha} + R_{ij} T_j^{\alpha} + \left(1 + \frac{1}{10} a^2 \nabla^2\right) K_{ijk} S_{jk}^{\alpha} \tag{2.95}$$

The problem is closed by coupling Eq. 2.95 with the Faxén laws expressed by Eq. 2.86, 2.87 and 2.88.

The result is a $11np \times 11np$ linear system that couples linear velocity of particles, angular velocity of particles and rate of strain of the fluid with hydrodynamic force, torque and stresslet through a *far-field* mobility matrix $\mathscr{M}^{\infty}$. The system can be written in a compact notation as [56]:

$$\left\{ \begin{array}{c} \mathbf{u} - \mathbf{u}^{\infty}(\mathbf{x}) \\ \boldsymbol{\omega} - \boldsymbol{\omega}^{\infty}(\mathbf{x}) \\ -\mathbf{E}^{\infty}(\mathbf{x}) \end{array} \right\} = -\mathscr{M}^{\infty} \left\{ \begin{array}{c} \mathbf{F}^{hydro} \\ \mathbf{T}^{hydro} \\ \mathbf{S} \end{array} \right\} \tag{2.96}$$

where $\mathbf{F}^{hydro} = (\mathbf{F}^1, ..., \mathbf{F}^{\alpha}, ..., \mathbf{F}^{np})$, $\mathbf{T}^{hydro} = (\mathbf{T}^1, ..., \mathbf{T}^{\alpha}, ..., \mathbf{T}^{np})$ and $\mathbf{S}$ are the hydrodynamic forces, torques and stresslet acting on the np particles composing the agglomerate. The mobility matrix is symmetric and positive definite, therefore it can be divided in submatrices, as reported in Eq. 2.97.

$$\mathscr{M}^{\infty} = \begin{bmatrix} \mathscr{M}^{\infty}_{UF} & \mathscr{M}^{\infty}_{UT} & \mathscr{M}^{\infty}_{US} \\ \mathscr{M}^{\infty}_{\Omega F} & \mathscr{M}^{\infty}_{\Omega T} & \mathscr{M}^{\infty}_{\Omega S} \\ \mathscr{M}^{\infty}_{EF} & \mathscr{M}^{\infty}_{ET} & \mathscr{M}^{\infty}_{ES} \end{bmatrix} \tag{2.97}$$

This formulation of the method is known as Force-Torque-Stresslet, or FTS. It is the most accurate formulation based on Stokesian dynamics approach, although low order and less precise formulations are also possible, by truncating the multipole expansion at the zero-th moment (F formulation) or at the anti-symmetric component of the first moment (FT, or Force-Torque formulation). The vectors $\mathbf{u} = (\mathbf{u}^1, ..., \mathbf{u}^{\alpha}, ..., \mathbf{u}^{np})$ and $\boldsymbol{\omega} = (\boldsymbol{\omega}^1, ..., \boldsymbol{\omega}^{\alpha}, ..., \boldsymbol{\omega}^{np})$ are the linear and angular velocities of the primary particles, while $\mathbf{u}^{\infty}(\mathbf{x})$ and $\boldsymbol{\omega}^{\infty}(\mathbf{x})$ are the linear and angular velocities of the undisturbed flow field at the particle location $\mathbf{x}$. The Brownian effect is neglected in this formulation, because SD approach will be adopted for systems composed by relatively large aggregates immersed in flow fields exerting a high hydrodynamic force: in other words, the role of Brownian motion is negligible with respect to the effect of the shear flow in our breakup simulations.

The far-field mobility matrix takes into account only long-ranged interaction between particles, therefore it correctly describes hydrodynamic interactions between particles that are relatively far apart. SD approach introduces a short-ranged correction based on lubrication theory, in order to correctly reproduce the behaviour of the particles that are in relative motion close to each other. This is achieved by treating lubrication forces as two-body interactions and introducing them in a pair-wise additivity manner. Inverting the far-field mobility matrix, a resistance matrix $\mathscr{R}$ is obtained. This resistance matrix needs to be corrected by adding the two-body resistance function $\mathscr{R}_{2B}$ and subtracting the far-field two-body resistance function $\mathscr{R}_{2B}^{\infty}$ in order not to count twice for those interactions. Expressions defining the far-field two-body resistance function are found in the literature [55]. The overall resistance matrix $\mathscr{R}$ is therefore calculated as follows:

$$\mathscr{R} = (\mathscr{M}^{\infty})^{-1} + \mathscr{R}_{2B} - \mathscr{R}_{2B}^{\infty} \tag{2.98}$$

By dividing the resistance matrix in submatrices:

$$\mathscr{R} = \begin{bmatrix} \mathscr{R}^{UF} & \mathscr{R}^{\Omega F} & \mathscr{R}^{EF} \\ \mathscr{R}^{UT} & \mathscr{R}^{\Omega T} & \mathscr{R}^{ET} \\ \mathscr{R}^{US} & \mathscr{R}^{\Omega S} & \mathscr{R}^{ES} \end{bmatrix} \tag{2.99}$$

and using Eq. 2.75, the problem can be reformulated as:

$$\left\{ \begin{array}{c} \mathbf{u} \\ \boldsymbol{\omega} \end{array} \right\} = \left\{ \begin{array}{c} \mathbf{u}^{\infty}(\mathbf{x}) \\ \boldsymbol{\omega}^{\infty}(\mathbf{x}) \end{array} \right\} + \begin{bmatrix} \mathscr{R}^{UF} & \mathscr{R}^{\Omega F} \\ \mathscr{R}^{UT} & \mathscr{R}^{\Omega T} \end{bmatrix}^{-1} \left\{ \begin{array}{c} \mathbf{F}^{cont} + \mathscr{R}^{EF} E^{\infty} \\ \mathbf{T}^{cont} + \mathscr{R}^{ET} E^{\infty} \end{array} \right\} \tag{2.100}$$

Time integration of $\mathbf{u}$ and $\boldsymbol{\omega}$ gives the location and the orientation of the particles. In our code, the integration step is performed by a first-order explicit Euler method.

2.3.4 Contact and colloidal forces

Contact mechanics allows us to convert the hydrodynamic forces and torques exerted by the fluid on the particles into a distribution of internal mechanical stress. Such internal tensions govern the relative displacement of the particles in the cluster. The normal contact force acting between a pair of primary particles was obtained by linearisation of the JKR theory [39, 47], which is the most suitable model for the relatively compliant polymeric particles we will examine in the next chapters, according to Tabor's criterion. For a pair of contacting particles the surface-to-surface distance h is related to the force F_n acting along the normal direction. This distance is nil when undeformed particles are just in contact and may become positive or negative due to the deformation of the contact region under traction or compression, respectively. The relationship between h and F_n is as follows:

$$h = \frac{b_0^2}{a}\left(\frac{1+\sqrt{1+F_n/F_{coh}}}{2}\right)^{1/3} \cdot \left(\frac{1-3\sqrt{1+F_n/F_{coh}}}{3}\right) \tag{2.101}$$

$$b_0 = \left[\frac{9\pi\gamma_s a^2\left(1-\nu^2\right)}{2E}\right]^{1/3} \tag{2.102}$$

where b_0 is the zero-load contact radius, γ_s is the surface energy of the solid, and ν and E are respectively the Poisson ratio and the elastic modulus of the primary particles. The cohesive force of the contact, i.e., the largest traction force that the contact can bear, is given by Eq. 2.52.

When two contacting particles are pulled apart, due to cohesive forces, the contact is preserved up to a positive surface-to-surface distance, referred to as pull-off distance h_{po}, which is the distance at which detachment occurs abruptly:

$$h_{po} = \left[\frac{3\pi^2\gamma_s^2 a\left(1-\nu^2\right)^2}{8E^2}\right]^{1/3} \tag{2.103}$$

In physical terms it means that, while particles are moving apart, a small neck of material is present at the contact, preventing detachment as long as its length is smaller than h_{po}.

When particles are not in contact but are located in very close proximity, a normal force arises because of colloidal van der Waals attraction. The strength of the interaction depends on h, the surface-to-surface distance, according to the following law:

$$F_n^{VDW} = \frac{A_h\, a}{12\,(h+z_0)^2} \tag{2.104}$$

where A_h is the Hamaker constant, and z_0 is the minimum approach distance, introduced to avoid the infinite attraction force that would be obtained at contact ($h = 0$); in fact, the molecular roughness of the particles and the short-ranged repulsion prevent this singularity from happening and keep the attraction force finite.

Particles are brought to contact by van der Waals attraction, up to $h = 0$. Given the prescribed JKR contact model, particles are deformed by the attraction force,

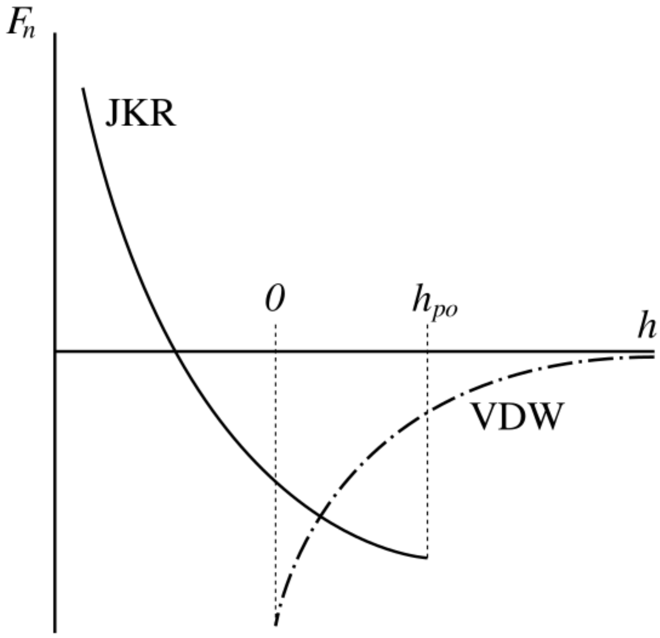

Fig. 2.10 Complete DEM model for two interacting particles. Dashdot line: normal force F_n given by van der Waals attraction (pre-contact). Solid line: F_n given by the JKR contact model (post-contact). Attraction for $F_n < 0$, repulsion for $F_n > 0$. Discontinuities between the two models in $h = 0$ and $h = h_{po}$.

up to a condition of overlap ($h < 0$). If a traction load is applied, particles can be separated, but they are considered to be still in contact even for $h > 0$ to simulate the necking phenomena: the bond is broken when the critical pull-off distance h_{po} is reached. At that point, normal force is again modelled as a van der Waals attraction. In other words, a discontinuity in the normal force arises at $h = 0$ and $h = h_{po}$ because of the switch between the van der Waals model and the JKR model occurring in these two points. These considerations are visualized in Fig. 2.10.

Forces and torques related to non-normal interactions, i.e., mutual sliding, rolling and twisting, were predicted by the model by Marshall [60], and are present only when particles are in contact. The sliding resistance force was calculated using a spring model which prescribes that:

$$F_s = \min\left(k_s \int_0^t \mathbf{u}_s(\tau) d\tau \cdot \mathbf{t}_s \,;\, F_s^{crit} \right) \tag{2.105}$$

where k_s is the sliding stiffness coefficient, and it is estimated using the following equation [52]:

$$k_s \approx 3.3 \frac{[\pi \gamma_s (1-\nu)]^{1/3}}{2-\nu} \left(\frac{aE}{1+\nu} \right)^{2/3} \tag{2.106}$$

The term $\mathbf{u}_s$ in Eq. 2.105 is the component of the particle relative velocity at the contact point aligned with the sliding direction $\mathbf{t}_s$. As long as the tangential force responsible for sliding is lower than the critical value F_s^{crit}, the force can be balanced by the elastic reaction of the contact, which is proportional to the tangential displacement. The critical displacement ξ^{crit}, corresponding to F_s^{crit}, is estimated on the basis of the work of Dominik and Thielens [61]:

$$\xi^{crit} \approx 0.05 \frac{\pi E b_0^2}{2(1+\nu)} \tag{2.107}$$

The twisting resistance torque M_t opposes the relative rotation of two particles around the axis connecting their centers. It is calculated using a relationship similar to the one of Eq. 2.105 and reads as:

$$M_t = \min \left(k_t \int_0^t \Omega_t(\tau) d\tau \, ; \, M_t^{crit} \right) \tag{2.108}$$

where Ω_t is the relative torsional velocity. The torsional stiffness coefficient k_t is given by:

$$k_t = 6\pi \gamma_s a^2 (1-\nu) \tag{2.109}$$

The critical angular displacement ϕ_t^{crit}, corresponding to the largest torsional torque that can be balanced by the elastic reaction of the contact before the contact point advances, is given by:

$$\phi_t^{crit} \approx 0.05 \frac{E b_0^3}{18 \gamma_s a^2 (1-\nu^2)} \tag{2.110}$$

The rolling resistance torque M_r and stiffness coefficient k_r are defined analogously to the sliding and twisting parameters. In order to distinguish the effect of rolling from other types of motions, the relative rolling velocity $\mathbf{u}_r$ between the two contacting spheres i and j is defined as follows [62]:

$$\mathbf{u}_r = -a \left(\mathbf{\Omega}_i - \mathbf{\Omega}_j \right) \times \mathbf{n} \tag{2.111}$$

where $\mathbf{\Omega}_i$ and $\mathbf{\Omega}_j$ are the angular velocities of the two particles and $\mathbf{n}$ the unit vector connecting their centers. The rolling resistance M_r is calculated as:

$$M_r = \min\left(k_r\left(\int_0^t \mathbf{u}_r(\tau)d\tau\right)\cdot\mathbf{t}_r\ ;\ M_r^{crit}\right) \tag{2.112}$$

where the term $\mathbf{t}_r$ is the direction of rolling, i.e., the unit vector aligned with the direction of the rolling velocity $\mathbf{u}_r$. The rolling stiffness coefficient k_r and the critical angular displacement ϕ_r^{crit} were respectively computed as:

$$k_r = 3\pi\gamma_s a^2 \tag{2.113}$$

$$\phi_r^{crit} \approx 0.2\frac{b_0}{a} \tag{2.114}$$

2.3.5 Rigid body approximation

A notable simplification of the method can be obtained in the limit of small elastic deformations. In this case, an agglomerate can be described as a rigid body: in other words, the relative position of the primary particles never changes, and therefore the velocity of each particle can be easily related to the velocity of the center of mass of the agglomerate, as shown in Eq. 2.115.

$$\begin{cases}\mathbf{u}^\alpha = \mathbf{u}^{cm} + \boldsymbol{\omega}^{cm}\times(\mathbf{u}^\alpha - \mathbf{u}^{cm})\\ \boldsymbol{\omega}^\alpha = \boldsymbol{\omega}^{cm}\end{cases} \tag{2.115}$$

Given the small dimension of the agglomerates, inertia is supposed to be negligible, therefore forces and torques acting on the agglomerate must be zero.

$$\begin{cases}\sum_{\alpha=1}^{np}(\mathbf{F}^\alpha + \mathbf{F}_{ext}^\alpha) = 0\\ \sum_{\alpha=1}^{np}[\mathbf{T}^\alpha + (\mathbf{u}^\alpha - \mathbf{u}^{cm})\times(\mathbf{F}^\alpha + \mathbf{F}_{ext}^\alpha)] = 0\end{cases} \tag{2.116}$$

$\mathbf{F}_{ext}^\alpha$ is the force acting on particle α.

To identify the occurrence of breakup, the hydrodynamic stress required is determined by comparing the internal force acting at each contact with the pull-off value required for severing the bond. The small scale motions at intermolecular contacts, due to surface forces or local deformations, are not considered in the approach, making the problem much better conditioned. The approach was proposed originally for isostatic agglomerates [51] and then extended to hyperstatic agglomerates [52] and it has then applied to the dynamics of breakup in turbulent fluids [63] and in highly viscous systems [64, 65]. Although this assumption causes the loss of some information about the dynamics of restructuring of the agglomerate, it can be employed without losing in accuracy if the agglomerate behaves almost like a rigid body until the breakup event, giving a substantial reduction of computing time.

2.4 CFD

Computational fluid dynamics is employed to thoroughly characterize the flow field of a fluid in an obstructed vessel. The equations of motion are solved using the software *ANSYS Fluent 20.* The resolution is based on a finite volume method [66], i.e., the solution is reached in an iterative way by dividing the domain into subdomains called *cells* and by solving equations of motion in every cell. The system investigated using CFD is biphasic, the continuous phase being a fluid flowing in an obstructed vessel, and the dispersed phase being micrometric drug carriers. Blood is a non-Newtonian fluid, composed of a continuous plasma matrix and a disperse phase, which includes red blood cells, white blood cells, and platelets. Although all these entities have size comparable with our drug carriers, we have considered blood as a pseudo-homogeneous liquid for the sake of simplicity. The particular composition of blood leads to a shear-thinning rheological behaviour, which has been described by resorting to a plethora of non-Newtonian models [67–69]. However, the common assumption of a Newtonian behaviour was seen to be sufficiently accurate in large vessels [70] and for high shear stresses [71]. Moreover, the influence of the dispersed phase (the drug carriers) on the flow field has been considered to be negligible given the small concentration and size of agglomerates, and therefore they were treated as tracer particles carried passively by the flow field. Finally, the short-term target of these simulations is to replicate a plausible experimental setup made by a dispersion of aggregates in a Newtonian fluid flowing in a microfluidic device. For all these reasons, CFD was employed to simulate the flow field of a continuous phase, Newtonian and incompressible. The path of massless particles passively carried by the flow field can be extracted, and agglomerates are considered to travel along these trajectories.

To model the continuous phase, the continuity equation and the Navier-Stokes equations were solved for a Newtonian, incompressible fluid by resorting to the *no-slip* condition for the walls of the vessel. The code solves the following continuity and momentum transport equations:

$$\nabla \cdot \mathbf{u} = 0 \tag{2.117}$$

$$\rho_l \frac{\partial \mathbf{u}}{\partial t} + \rho_l \nabla \cdot (\mathbf{u}\mathbf{u}) = -\nabla p + \nabla \tilde{\tau} \tag{2.118}$$

where $\mathbf{u}$ is the velocity of the fluid, ρ_l is the fluid density, p is the pressure, and $\tilde{\tau}$ is the viscous stress tensor. The system is laminar, and viscosity was assumed to be constant, hence the stress tensor is:

$$\tilde{\tau} = \mu \left(\nabla \mathbf{u} + \nabla \mathbf{u}^T \right) \tag{2.119}$$

The system quickly evolves to the condition of steady-state, so this is the condition of interest.

The code is based on a finite volume method approach to solve partial differential equations. The linear system resulting from the discretization of the conservation equations was solved by the software using a pressure-based segregated algorithm [72]. Pressure and velocity were coupled by using the Semi-Implicit Method for Pressure Linked Equations (SIMPLE) algorithm. Starting from an initialized solution:

1. Momentum equations are solved sequentially;
2. The obtained flow field is corrected using a pressure equation derived from continuity and momentum equations;
3. Properties of the system are updated;
4. Process is repeated until convergence is reached.

As mentioned above, the computational domain is subdivided in cells. The cells are mostly hexahedral, and they are aligned to the flow field in order to reduce the numerical diffusion effect. A second order upwind scheme was employed for spatial discretization.

Once that the flow field of the continuous phase has been calculated, it is possible to extract a set of trajectories followed by particles dispersed in the fluid. In Stokes regime, it is possible to calculate the trajectory through a balance of the forces acting on a single particle, the so-called Basset-Boussinesq-Oseen (BBO) equation [73].

As mentioned above, the system is considered to be highly diluted, therefore the trajectories of every agglomerate flowing in the obstructed vessel is computed as if the agglomerate was alone. Moreover, if agglomerates are supposed to be massless, many terms in the BBO equation vanish and their trajectory is described in terms of the velocity of the fluid $\mathbf{u}(x) = dx_l/dt$ by the simple equation:

$$\frac{dx_l}{dt} = \dot{x}_p \tag{2.120}$$

eventually re-written as:

$$\frac{d\dot{x}_p}{dt} = \frac{1}{\tau_p}(\dot{x}_l - \dot{x}_p) + a_c \tag{2.121}$$

where a_c is the acceleration due to forces acting on the particle, except for drag force, taken into account by the particle relaxation time τ_p, which is defined as:

$$\tau_p = \frac{2\rho_p a^2}{9\mu}\frac{24}{C_D Re} \tag{2.122}$$

where C_D is the drag coefficient and Re is the Reynolds number. Eq. 2.121 can be solved with a temporal discretization. Using an implicit trapezoidal scheme, Eq. 2.123 is obtained.

$$\frac{\dot{x}_p^{n+1} - \dot{x}_p^n}{\Delta t} = \frac{1}{\tau_p}(\dot{x}_l^* - \dot{x}_p^*) + a_c^n \tag{2.123}$$

$\dot{x}_p^{n+1}$ is the particle velocity at step $n+1$, $\dot{x}_p^n$ is the particle velocity at step n, a_c^n is the acceleration at step n, and $\dot{x}_l^* = \frac{1}{2}(\dot{x}_l^n + \dot{x}_l^{n+1})$, $\dot{x}_p^* = \frac{1}{2}(\dot{x}_p^n + \dot{x}_p^{n+1})$ are the average velocities between the two considered steps, for the fluid and the particle respectively. Explicit schemes are employed for a preliminary calculation of the terms $\dot{x}_l^{n+1}$ and $\dot{x}_p^{n+1}$. Finally, the position of the particle is updated from the step n to the step $n+1$ through the following equation:

$$x_p^{n+1} = x_p^n + \frac{1}{2}\Delta t(\dot{x}_p^n + \dot{x}_p^{n+1}) \tag{2.124}$$

A massless particle has the same velocity of the fluid at the particle position, i.e., $\dot{x}_l = \dot{x}_p$. This condition leads to a massive simplification of the algorithm for particle tracking.

Hydrodynamic forces acting on the dispersed phase have to be monitored along trajectories, and are related to the velocity gradient and the strain rate. The velocity gradient $\nabla\mathbf{u}$ defined by Eq. 2.125 is monitored along every trajectory. $\mathbf{D}$ is its symmetric component.

$$\nabla\mathbf{u}=\begin{bmatrix}\frac{\partial u_x}{\partial x} & \frac{\partial u_x}{\partial y} & \frac{\partial u_x}{\partial z}\\ \frac{\partial u_y}{\partial x} & \frac{\partial u_y}{\partial y} & \frac{\partial u_y}{\partial z}\\ \frac{\partial u_z}{\partial x} & \frac{\partial u_z}{\partial y} & \frac{\partial u_z}{\partial z}\end{bmatrix} \tag{2.125}$$

$$\mathbf{D}=\frac{1}{2}\left(\nabla\mathbf{u}+\nabla\mathbf{u}^T\right)=\frac{1}{2}\begin{bmatrix}2\frac{\partial u_x}{\partial x} & \frac{\partial u_x}{\partial y}+\frac{\partial u_y}{\partial x} & \frac{\partial u_x}{\partial z}+\frac{\partial u_z}{\partial x}\\ \frac{\partial u_y}{\partial x}+\frac{\partial u_x}{\partial y} & 2\frac{\partial u_y}{\partial y} & \frac{\partial u_y}{\partial z}+\frac{\partial u_z}{\partial y}\\ \frac{\partial u_z}{\partial x}+\frac{\partial u_x}{\partial z} & \frac{\partial u_z}{\partial y}+\frac{\partial u_y}{\partial z} & 2\frac{\partial u_z}{\partial z}\end{bmatrix} \tag{2.126}$$

The *strain rate* $\dot{\gamma}$ is related to the traces of tensors D and D^2 and it is calculated as[3]:

$$\dot{\gamma}=\sqrt{2[tr(D)^2-tr(D^2)]} \tag{2.127}$$

It is worth noting that a pure shear flow with a single non-zero component of the velocity gradient $\partial u_x/\partial y$ has strain rate $\dot{\gamma}=|\partial u_x/\partial y|$, whereas a planar elongational flow with $\partial u_x/\partial x=-\partial u_y/\partial y\neq 0$ and all other components null gives $\dot{\gamma}=\frac{1}{2}|\partial u_x/\partial x|$. In finite volume solvers, such as Fluent, the velocity gradient, and therefore the strain rate, has a constant value in every cell of the mesh, and we used that value without further interpolation, in view also of the high resolution of the grid. Hence, the value of the strain rate at a specific point along a trajectory is the value of the strain rate in the cell where the point is located.

The flow field is characterized also by the *vorticity* $\tilde{\omega}$, related to the antisymmetric component of the velocity gradient ω_{ij}^{∞}, as expressed by the following equations:

$$\omega_{ij}^{\infty}=\frac{1}{2}\left(\frac{\partial u_i}{\partial x_j}-\frac{\partial u_j}{\partial x_i}\right) \tag{2.128}$$

$$\tilde{\omega}=\sqrt{2\,\omega_{ij}^{\infty}\,\omega_{ij}^{\infty}} \tag{2.129}$$

The strain rate and the vorticity are a measure of the elongational and the rotational component of the flow field, respectively. The relative weight of the two

---

[3] In terms of components of the velocity gradient:
$\dot{\gamma}=\sqrt{2\left(\frac{\partial u_x}{\partial x}\right)^2+2\left(\frac{\partial u_y}{\partial y}\right)^2+2\left(\frac{\partial u_z}{\partial z}\right)^2+\left(\frac{\partial u_x}{\partial y}+\frac{\partial u_y}{\partial x}\right)^2+\left(\frac{\partial u_x}{\partial z}+\frac{\partial u_z}{\partial x}\right)^2+\left(\frac{\partial u_y}{\partial z}+\frac{\partial u_z}{\partial y}\right)^2}$

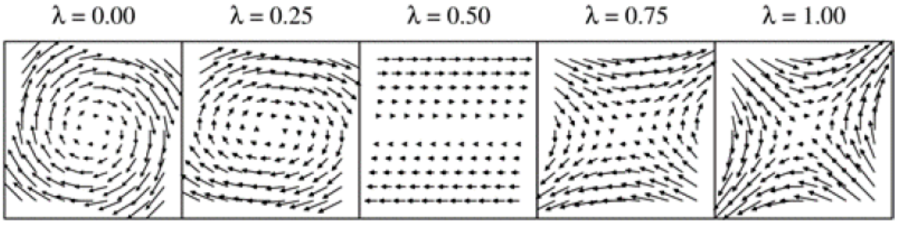

Fig. 2.11 Flow field as a function of the mixing index λ. For $\lambda \to 0$ to $\lambda \to 1$ the flow field goes from purely rotational to purely elongational. For $\lambda \simeq 0.5$, the flow is in condition of simple shear.

components is expressed as the *mixing index* λ, defined as:

$$\lambda = \frac{\dot{\gamma}}{\dot{\gamma} + \tilde{\omega}} \tag{2.130}$$

For $\lambda \to 0$, the flow field is predominantly rotational; for $\lambda \to 1$, it has a strong elongational component; for $\lambda \simeq 0.5$, the flow is in condition of simple shear, that is, the rotational and the elongational components equally contribute to the flow field. These considerations are summarized in Fig. 2.11.

Chapter 3

Simulation of spray drying

The chapter is based on the following article written by the candidate: Vasquez Giuliano, L., Buffo, A., Vanni, M., Frungieri, G., "Micromechanics and strength of agglomerates produced by spray drying", JCIS Open, 2023 [20].

3.1 Dynamics of spray drying

The tuning of the properties of the final drug carriers is intertwined with the production conditions. Therefore, a better understanding of the spray drying process leading to the formation of agglomerates is fundamental to drive the agglomeration mechanism and to control the morphology of the clusters and their mechanical features. Spray drying is a well-established technique to produce agglomerates of nanoparticles for pharmaceutical purposes [74–78]. Besides, it is also frequently applied in the manufacturing of ceramic powders [79, 80], the production of storage supports for lithium ions [81], of multi functional textiles [82], and it is often employed in the food industry, where it is used to increase the stability of perishable products [83]. The process starts from a liquid suspension of small colloidal particles: the suspension is atomized by flowing through a nozzle, it is brought in contact with a hot drying gas, and the suspension droplets generated upon atomization finally undergo evaporation, returning dry large agglomerates composed of small primary particles in contact. The morphology of the agglomerates produced in a spray drying process depends upon several variables, such as humidity, temperature, dimension of the atomized droplets and primary particles size and shape [84–86]. In this context, a number of theoretical and experimental studies showed that, among the most relevant parameters affecting the cluster morphology, the droplet Péclet number plays a key role. This dimensionless number expresses the ratio between the characteristic Brownian diffusion time of the colloidal particles inside the evaporating droplet and the characteristic droplet evaporation time [87–90]. A high value of the Péclet number is obtained if the velocity of diffusion of the primary particles in the droplet is slow compared to the droplet shrinkage velocity. In this case, the particles tend to accumulate at the evaporating front and, if adhesive forces between particles are strong enough to keep the particle in contact, the final agglomerate becomes a spherical shell, characterized by a void core and by an external crust made of contacting particles. On the contrary, low Péclet number conditions are encountered when the solvent evaporation is slow and the particle Brownian motion is intense; in this case the concentration of particles in the droplet is kept homogeneous throughout the drying process and the resulting agglomerate is compact [91].

The high variability of parameters involved in spray drying makes the process hard to model in its entirety. Therefore, it can be convenient to observe the drying of single droplets by mimicking the process conditions in the actual spray dryer [88], and to develop models for the process based on these observations. Different approaches can be adopted to model the solid phase dynamics during a spray drying process. Some rely on the study of the nucleation and growth of the solid phase thanks to energy and mass transport equations linked to a population balance model [92–94]. It has also been shown that the population balance can be coupled with CFD simulations to estimate model parameters, track the droplet trajectories and improve the predictions made by the model [95]. Although this method can provide some insights in the morphology of the produced agglomerates, it cannot reach the level of structural details that discrete element method simulations are able to return [96]. This method was employed for instance by Miyazaki and coworkers [97] to study particle aggregation in an evaporating droplet and was also used to describe the spray drying process when the radius of the colloidal particles follows a bimodal distribution [98, 99]. For this reason, in this thesis the formation of the agglomerates has been studied by a discrete element method, able to accurately track the motion of each single colloidal particle by keeping into account all the relevant particle-particle interactions, both direct and fluid-mediated, including therefore van der Waals forces, contact forces, Brownian motion and fluid induced stress.

The simulated system consists of a population of spherical colloidal particles with common radius a, initially uniformly dispersed within a single spherical shrinking droplet of water. The temperature T in the droplet was assumed to be uniform. As mentioned in Section 2.2.3, forces and torques acting on the primary particles are calculated in order to evolve their equations of motion, and are solved individually for each particle. The position of a single particle is updated for the next timestep by a second order integration of the equation of motion (See Eq. 2.57). The term on the right-hand side counts for all the forces the particle is subject to: the already mentioned drag force, brownian force, adhesive force, and the capillary force, which acts on the particles located at the evaporating front. A quadratic law was prescribed to model the reduction in time of the droplet radius R starting from the initial value R_0 [99]:

$$[R(t)]^2 = R_0^2 - k \cdot t \tag{3.1}$$

from which the total evaporation time τ corresponding to the condition $R(t) = 0$ can be calculated as $\tau = R_0^2/k$. Equation 3.1 is inferred from a mass and heat balance on the droplet and predicts a linear decrease of droplet surface in time. Such a model is fully appropriate for the first stage of drying, where the solvent occupies a major portion of the evaporating front and as such the process is similar to the evaporation of a particle-free droplet of solvent. An explanation for the prescribed quadratic law is given in Appendix B. It has to be mentioned the fact that as drying proceeds the evaporation rate might be affected by the accumulation of particles on the droplet surface which forces the solvent to diffuse through the void space between them [92, 100]. However, even if such a feature can be in principle incorporated in this modelling framework, no established form for describing this secondary stage of drying exists. Furthermore, the entity of adhesion forces in the following simulation is such that small or no restructuring of the final agglomerate is observed after contacts have been established, making the effect of the final part of the evaporation on aggregate morphology unimportant.

As the droplet dries, the solid particles are drawn inwards by capillary forces. The force arising from the interaction between the surface of the droplet and the particles wet by it is therefore modelled as a force oriented toward the center of the spherical droplet whose magnitude, proportional to the wet perimeter of the particle, was calculated as:

$$F_c = 2\pi\sigma\sqrt{a^2 - (r-R)^2} \tag{3.2}$$

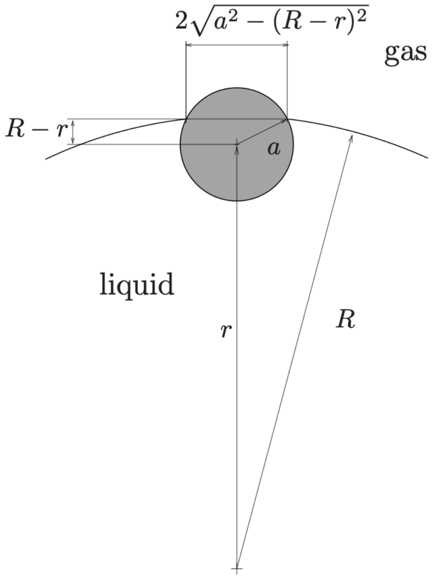

Fig. 3.1 Primary particle in contact with droplet surface: estimation of the wet perimeter and capillary force.

where σ is the surface tension of the liquid and r the radial coordinate of the particle in a reference system centered at the droplet center of mass (Fig. 3.1). In principle the rigorous evaluation of the capillary force should take into account the shape of the meniscus at the solid-liquid contact line and the contact angle. Equation 3.2 is therefore a simplification that correctly predicts the maximum capillary force for a fully wettable particle at the interface ($2\pi a\sigma$), and allows for a smooth transition of F_c to zero when the particle becomes completely immersed in the liquid.

As already mentioned, contact forces are assumed to be strong enough to make post-contact deformations extremely small. Hence, the generated structure is rigid, and does not exhibit the restructuring that may occur as a result of significant sliding or rolling phenomena of one particle on another in the secondary part of drying. Under these conditions, the results do not depend on the intensity of the capillary centripetal force, which merely moves the particles towards the center of the droplet without being able to induce rearrangement of the structure. Based on this consideration, a surface tension value that is much lower than that of the real liquid-vapour interface has been adopted. This made the simulations more stable and faster, without affecting the robustness of the predictions.

In this part of the work, no direct modelling of particle-particle hydrodynamic interactions has been adopted, i.e., lubrication forces and pre-contact van der Waals attraction between particles were both neglected at this stage, proceeding from the assumption that they have opposite effects in inducing particle contact. Lubrication forces tend in fact to keep particles away from each other, whereas van der Waals forces act promoting their contact. Their interplay may play a role in the kinetics of the contact formation but it is not expected to significantly affect the agglomerate morphology once contacts are formed. It is believed in fact that agglomeration in a shrinking droplet is driven by the capillary force acting on the particles sitting at the liquid-vapour interface, which, by retracting, pushes the particles towards each other inducing a force that is largely dominating over the resistance induced by hydrodynamic interactions. The parameter values used for the spray drying investigation are listed in Table 3.1.

3.2 Validation for short times

The predictions obtained by the single-droplet discrete element method simulations have been compared with a continuous model which can be deemed as a good approximation of the spray drying process in the initial part of the evaporation process and in the limit of low particle concentration. In such conditions, the dynamics of the population of particles can be studied as one would study the evolution of the concentration of a dissolved solute, which undergoes molecular diffusion inside the shrinking droplet.

We assumed the droplet to have an initial radius equal to R_0 and to shrink accordingly to the quadratic law of Eq. 3.1. The receding velocity v of the evaporating front is therefore given by:

$$v = -\frac{dR}{dt} = \frac{k/2}{R} \tag{3.3}$$

Parameter	Symbol	Value	Units
Particle density	ρ_p	1300	kg m^{-3}
Elastic modulus	E	3.40	GPa
Poisson ratio	ν	0.5	-
Surface tension	σ	$1.75 \cdot 10^{-4}$	N m^{-1}
Superficial energy	γ_s	$4.80 \cdot 10^{-3}$	N m^{-1}

Table 3.1 Parameter values used for the contact forces in *Yade* simulations.

If $C(r,t)$ is the solute concentration,i.e., the number concentration of primary particles, its evolution in time inside the spherical droplet can be described by the following unsteady diffusion equation [101]:

$$\frac{\partial C}{\partial t} = \frac{D}{r^2}\frac{\partial}{\partial r}\left(r^2\frac{\partial C}{\partial r}\right) \tag{3.4}$$

with boundary conditions at the center of the droplet and at the receding front, respectively defined as:

$$\left[\frac{\partial C}{\partial r}\right]_{r=0} = 0 \tag{3.5}$$

$$\left[vC - D\frac{\partial C}{\partial r}\right]_{r=R(t)} = 0 \tag{3.6}$$

The boundary conditions prescribe therefore that the system has radial symmetry (Eq. 3.5), and that the interface is impermeable to the solid, such that the diffusive flux given by the Fick's law balances the flux vC at the outer radius of the droplet (Eq. 3.6). We set a uniform initial concentration defined as $C|_{t=0} = C_0$. Parameter D is the diffusion coefficient of the primary particles due to the Brownian motion, which was calculated using the Stokes-Einstein equation:

$$D = \frac{k_b T}{6\pi\mu a} \tag{3.7}$$

where k_b is the Boltzmann constant. The continuous problem is conveniently reformulated in term of dimensionless concentration $\Gamma = C/C_0$, dimensionless time $\theta = kt/R_0^2$ and dimensionless radial position $\tilde{\rho} = r/R(t)$. By doing so, the moving boundary problem defined by the boundary condition of Eq. 3.6 is transformed in a fixed boundary problem, where the condition is applied at the constant dimensionless coordinate $\tilde{\rho} = 1$. Moreover, the solution depends on a single parameter, the Péclet number k/D, i.e., the ratio between the velocity of droplet evaporation and the velocity of diffusion. The dimensionless set of equations reads as follows:

$$\frac{\partial \Gamma}{\partial \theta} = -\frac{\tilde{\rho}}{2(1-\theta)}\frac{\partial \Gamma}{\partial \tilde{\rho}} + \frac{D/k}{1-\theta}\left(\frac{2}{\tilde{\rho}}\frac{\partial \Gamma}{\partial \tilde{\rho}} + \frac{\partial^2 \Gamma}{\partial \tilde{\rho}^2}\right) \tag{3.8}$$

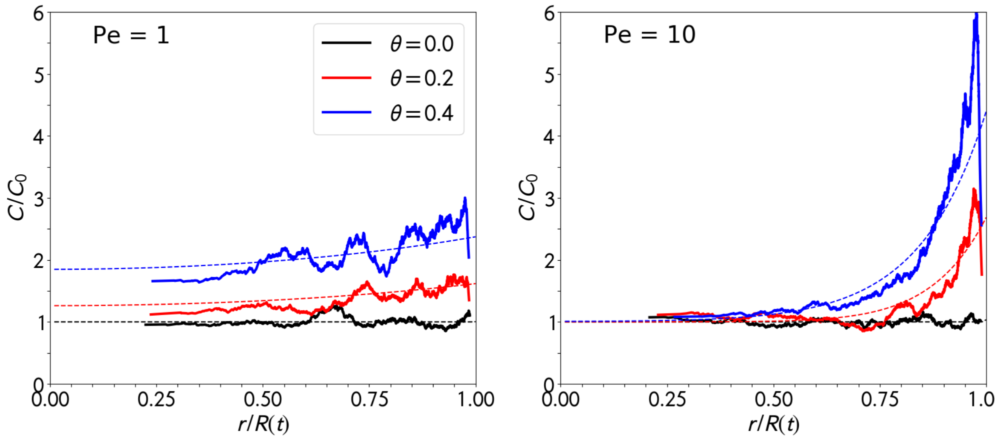

Fig. 3.2 Average concentration profile in a shrinking droplet for different values of the dimensionless time obtained from DEM simulations (solid lines) and the continuous model (dashed lines). Black, red and blue lines correspond to dimensionless times θ of 0.0, 0.2 and 0.4 respectively. Left: Pe = 1. Right: Pe = 10.

$$\left[\Gamma - 2\frac{D}{k}\frac{\partial\Gamma}{\partial\tilde{\rho}}\right]_{\tilde{\rho}=1} = 0\ ;\ \theta > 0 \tag{3.9}$$

$$\Gamma(\theta = 0) = 1\ ;\ 0 < \tilde{\rho} < 1 \tag{3.10}$$

Equation 3.8 was solved by using a second order finite difference scheme for discretizing the spatial coordinate and a Runge-Kutta scheme for the time advancement of the discretized solution.

Results for two different values of the Péclet number are reported in Fig. 3.2 as dashed lines and compared with the discrete element method results (solid lines). The graphs report the number particle concentration profile in the shrinking droplet for three different dimensionless times: $\theta = 0.0$, $\theta = 0.2$ and $\theta = 0.4$. It can be noticed that the average concentration increases in time as a consequence of droplet volume reduction, but also that the Péclet number has a significant effect on the concentration profile dynamics. The particle concentration is almost homogeneous in the droplet volume for $\mathrm{Pe} = 1$, because of the predominant effect of particle diffusivity over droplet shrinkage, whereas for larger Péclet, the concentration rapidly increases at the periphery of the droplet and a steep variation of the concentration profile can be observed along the radial coordinate r.

The graphs also report the DEM predictions; here the concentration profiles were obtained by using data from 25 equivalent realizations of the process, with 100

monomers	a [nm]	R_0 [µm]	τ [ms]	D [m^2/s]	Pe
100	10	0.215	0.21	$2.2 \cdot 10^{-11}$	10
100	10	0.215	2.10	$2.2 \cdot 10^{-11}$	1

Table 3.2 Main parameters of the DEM simulations contrasted with the continuous method of Eq. 3.4.

primary particles in each realization. The main parameters of the DEM simulations are reported in Table 3.2. The number concentration in the surroundings of each primary particle was calculated by considering the spherical shell that includes the 20 particles located immediately before and after the considered particle along the radial coordinate. The agreement between the continuous and discrete results is satisfactory, with the small discrepancies to be ascribed to the finite size of the particles used in the DEM simulations compared to the droplet size, which necessarily induce some statistical noise in the data. Moreover, it is unlikely for a particle of finite size to have its center of mass located at the extreme periphery of the droplet, thus explaining the concentration drop for $r/R(t) \to 1$. Nevertheless, the agreement proves that the adopted simulation strategy correctly predicts the particle collective behaviour inside the droplets. While in the present section only the early stages of drying are simulated, i.e., up to $\theta = 0.4$, in the following sections the spray drying process will be simulated in its entirety, i.e., up to $\theta = 1$.

3.3 Results

3.3.1 Péclet number

The ratio between the time scale of diffusion and the time scale of droplet evaporation, described by the Péclet number, was seen to have a major influence on the final morphology of the agglomerates. In the following DEM simulations, we computed the Péclet number as:

$$\mathrm{Pe} = \frac{R_0^2}{D\tau} \tag{3.11}$$

where R_0 is the droplet initial radius, τ is the shrinkage time of the droplet, given by the shrinkage rate relationship of Eq. (3.1), and D is the diffusion coefficient of the primary particles due to the Brownian motion, which was calculated using the

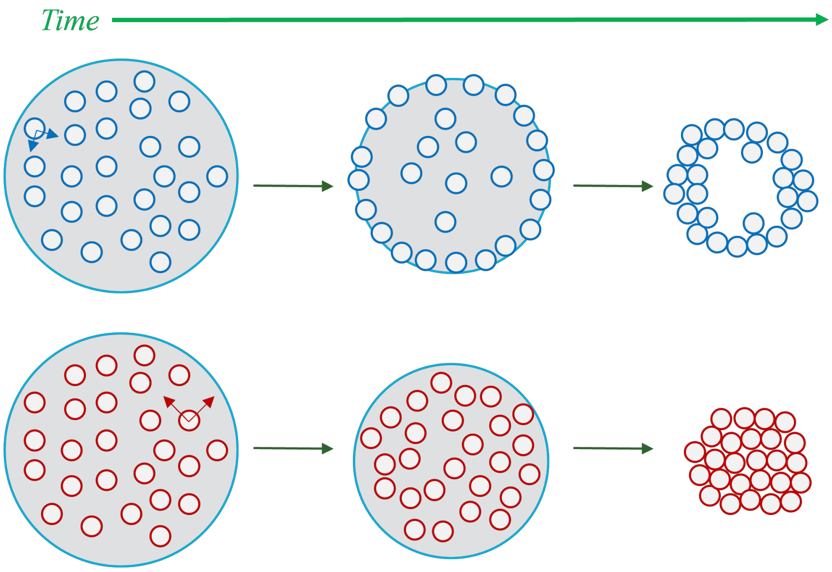

Fig. 3.3 Formation of agglomerates in a shrinking droplet at different conditions of Péclet number. Top: large Péclet number, diffusion is slow compared to the evaporation velocity, the particles accumulate at the evaporating front, resulting in a hollow aggregate. Bottom: low Péclet number, diffusion is fast compared to the evaporation velocity, the concentration of primary particles in the droplet is homogeneous throughout the process, resulting in a compact aggregate.

Stokes-Einstein equation (Eq. 3.7). In Eq. 3.11, R_0^2/D can be seen as a characteristic diffusion time of the particles inside the droplet.

The Péclet number is large when diffusion is slow compared to the evaporation velocity: in this case, the particles are not re-distributed in the droplet by Brownian motion and were seen to accumulate at the evaporating front, where they constituted a spherical shell or crust. On the contrary, the Péclet number is low if diffusion is fast compared to the time scale of evaporation: in this case, the concentration of primary particles in the droplet was seen to be kept homogeneous by Brownian motion throughout the evaporation, and finally the generation of homogeneous and compact spherical agglomerates was observed. A visual explanation of the phenomenon is presented in Fig. 3.3.

We quantitatively characterized these different emerged morphologies by computing the radial distribution of the primary particles, the diameter d_c and the crust thickness h_c of the agglomerates generated. The radial distribution for a sample of agglomerates is presented in Fig. 3.4 as a cumulative distribution function (CDF) that reports the fraction of particles located at radial distance from the center of mass

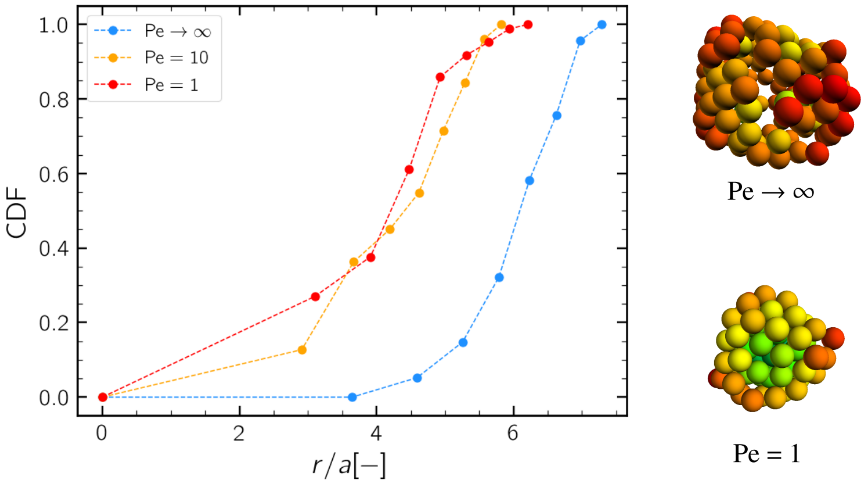

Fig. 3.4 CDF of the particle radial distribution in agglomerates obtained for different values of Péclet number. The structures obtained for $\mathrm{Pe} \to \infty$ and $\mathrm{Pe} = 1$ are visually shown. The colormap highlights the difference between the empty core of the cluster obtained for $\mathrm{Pe} \to \infty$ and the compact core of the cluster obtained for $\mathrm{Pe} = 1$. Green primary particles are close to the centre of mass of the agglomerate, red primary particles are far from it.

of the granule smaller than r. The plot compares the agglomerates generated from three simulations conducted at different Péclet numbers, obtained by varying the shrinkage velocity. The principal simulation parameters are reported in Table 3.3. In all cases the agglomerates are made of around 100 primary particles. For the ideal case of $\mathrm{Pe} \to \infty$, the diffusion coefficient D was set to zero. From the CDF and the picture of the agglomerates, it can be noticed that clusters with a compact core were obtained at low Péclet numbers ($\mathrm{Pe} < 10$), while hollow agglomerates with a large internal cavity were observed for $\mathrm{Pe} \to \infty$. Fig. 3.5 shows the evolution in time of the simulations conducted at $\mathrm{Pe} \to \infty$ and $\mathrm{Pe} = 1$. Similarities with the theoretical behaviour proposed in Fig. 3.3 can be observed.

monomers	a [nm]	R_0 [µm]	τ [ms]	D [m^2/s]	Pe	d_c [nm]	h_c/d_c
$\sim$100	10	0.215	0.21	0	∞	160	0.28
$\sim$100	10	0.215	0.21	$2.2 \cdot 10^{-11}$	10	132	0.43
$\sim$100	10	0.215	2.10	$2.2 \cdot 10^{-11}$	1	132	0.44

Table 3.3 Effect of the Péclet number - principal parameters of simulations and values of d_c, h_c and h_c/d_c associated to the final cluster.

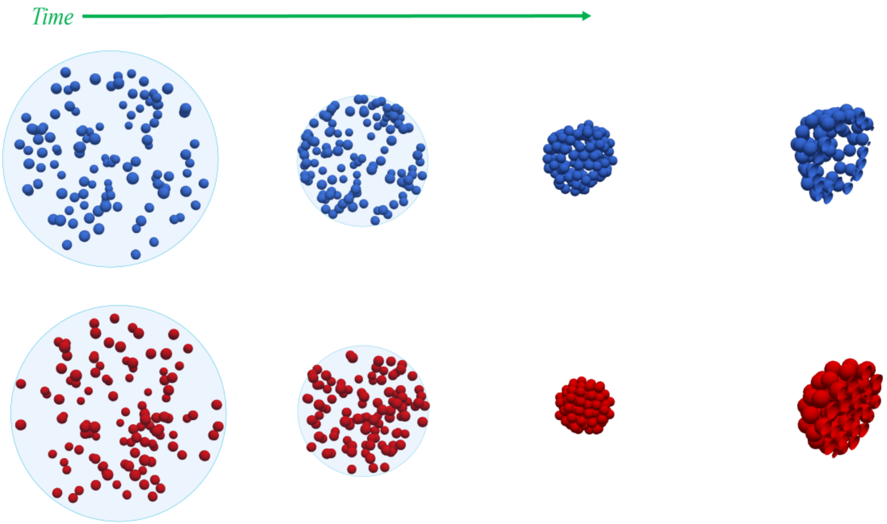

Fig. 3.5 Formation of agglomerates in a shrinking droplet simulated at Pe → ∞ (top) and Pe = 1 (bottom), and cross-section of the final hollow and compact agglomerates. The agglomerate obtained at Pe → ∞ shows an empty core, while the agglomerate obtained at Pe = 1 is compact.

The outer radius of a cluster has been defined as the mean distance from the c.o.m. of 10% of the farthest primary particles plus the radius of a primary particle; analogously, the inner radius is the mean distance of 10% of the nearest particles minus the radius of a primary particle [98]. Following these definitions, the diameter of the agglomerate d_c is two times the outer radius and the crust thickness h_c is the difference between the outer radius and the inner radius. A visual representation is given in Fig. 3.6 . The ratio h_c/d_c can be used to characterize the agglomerates: a low value of h_c/d_c means that the agglomerate is shell-shaped with an inner cavity, and it is classified as an *hollow* agglomerate; on the other hand, the maximum theoretical value for h_c/d_c, which is equal to 0.5, holds for clusters that are compact and homogeneous, and classified as *compact*. The values of h_c/d_c reported in Table 3.3 confirms what inferred from the particle radial distribution. For low Péclet numbers h_c/d_c tends to 0.5, meaning that the final agglomerate is compact, whereas for Pe → ∞, h_c/d_c is small, and the resulting agglomerate can be classified as hollow.

In the production of micrometric agglomerates, the initial droplet radius is often reported to be around 20-50 μm and the shrinkage time to range between 0.01 and 0.1 s. Under these conditions, which are quite frequent in practical drying systems, the Péclet number is always much larger than the unity, even in the presence of

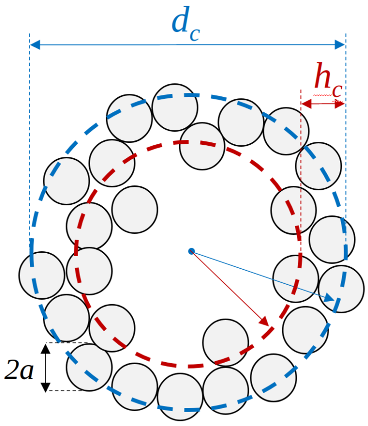

Fig. 3.6 Visual representation of the diameter of the agglomerate d_c and the crust thickness h_c. a is the radius of primary particles composing the agglomerate.

extremely small primary particles. For this reason we examined in some detail the behavior of the system in the high Péclet regime and, in particular, the effect of the evaporation time τ on the final shape of the granules. A set of simulations at large Péclet number but with different shrinkage times was performed (Table 3.4). For every condition of the system, five different but equivalent simulations were realized. The results are summarized in Figure 3.7, where it can be noticed that both the size (left plot) and the ratio h_c/d_c (right plot) are not affected by the variation of the shrinkage time in the high Pe limit, thus proving that in such a regime agglomerate morphology become insensitive to small variations of the drying conditions.

monomers	a [nm]	R_0 [µm]	τ [ms]	D [m^2/s]	Pe
60	1000	40	3	$2.2 \cdot 10^{-13}$	$2.4 \cdot 10^{6}$
60	1000	40	6	$2.2 \cdot 10^{-13}$	$1.2 \cdot 10^{6}$
60	1000	40	12	$2.2 \cdot 10^{-13}$	$6.1 \cdot 10^{5}$
60	1000	40	18	$2.2 \cdot 10^{-13}$	$4.1 \cdot 10^{5}$
60	1000	40	25	$2.2 \cdot 10^{-13}$	$2.9 \cdot 10^{5}$

Table 3.4 Principal parameters of the simulations for evaluating the effect of the shrinkage time τ in the high Péclet number limit.

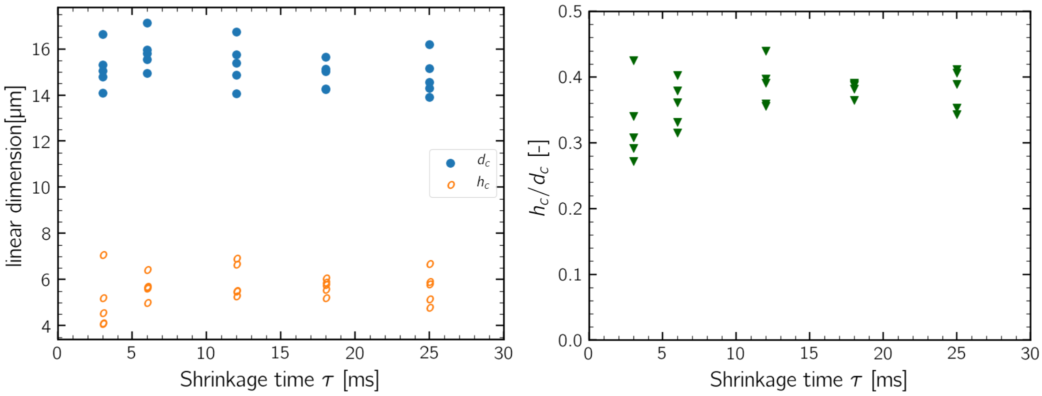

Fig. 3.7 Values of h_c, d_c and ratio h_c/d_c for clusters obtained at high Péclet number by varying the shrinkage time τ. For every τ, five different but equivalent simulations are considered. The cluster morphology is not significantly affected by the shrinkage time in the high Péclet number regime.

3.3.2 Solid Fraction

Although the Péclet number is a valuable tool to characterize this kind of simulations, some variables are not taken into account in its definition, for instance the volumic fraction of nanoparticles dispersed in the droplet. If the solid fraction is increased, agglomerate morphology may not be fully described by the Péclet number, i.e., aggregates could not be exactly classified as compact or hollow. In order to study the effect of particle concentration on the final cluster, simulations at $\mathrm{Pe} \to \infty$ have been conducted, starting from 1% solid fraction, then increased up to 2%, 5% and 7% by varying the number of monomers. Table 3.5 summarizes the results. No significant differences in terms of h_c/d_c have been observed, suggesting that the formation of an irregular aggregate requires a much higher solid fraction, incompatible with the computational cost of the simulations. However, relying on the fact that D is set to zero for this peculiar set of simulations, it is possible to increase the solid fraction by tuning the monomer radius a eluding any influence on the diffusivity and on the Péclet number. In this way, a high solid fraction can be set without significantly affecting the computational time. The radius of the monomers has been modified in order to obtain a solid fraction of 2%, 5%, 7%, 10%, 14%, and results are shown in Table 3.5 and in Fig. 3.8. The ratio h_c/d_c reaches higher values when bigger primary particles are considered, showing that the higher is the solid fraction, the less defined is the crust of the resulting agglomerate. The trend of the CDF associated to the radial distance of primary particles with respect to the c.o.m. of the agglomerates leads to analogous considerations.

3.3.3 Comparison with notable agglomerates

In this Section, agglomerates produced via single-droplet simulation of spray drying are compared with notable agglomerates having similar properties. Compact clusters produced at Pe $= 1$ and hollow clusters produced at Pe $\to \infty$ are compared with random close packing (RCP) agglomerates and hollow agglomerates of similar size, shape and dimension of the monomers.

RCP agglomerates were generated numerically using the Random Close Packing algorithm proposed by Skoge and coworkers [102], which arranges particles in such a way as to minimize the void fraction inside the aggregate (around 36%), avoiding at the same time the formation of an ordered structure. Starting from this highly-compacted type of structure, notable hollow agglomerates were generated by removing internal primary particles while keeping intact the outer shell. The parameter R_v normalized over the maximum radius of the agglomerate R_{max} defines the radius of the internal void core of these artificially generated clusters. Fig. 3.9 shows a notable aggregate for each class. Compact agglomerates generated via spray drying were compared with RCP agglomerates of the same size: for both classes, a=10 nm and $np \approx 90$. In the same way, hollow agglomerates generated via spray

monomers	a [nm]	solid fraction	Pe	d_c [nm]	h_c/d_c
100	10	1.1%	∞	153	0.31
197	10	2.0%	∞	195	0.29
515	10	5.2%	∞	259	0.32
687	10	6.9%	∞	276	0.31
100	13	2.0%	∞	198	0.34
102	17	5.1%	∞	251	0.32
94	19	6.6%	∞	268	0.38
95	22	9.5%	∞	307	0.40
89	25	13.9%	∞	329	0.40

Table 3.5 Effect of the solid fraction - principal parameters of simulations and values of d_c and h_c/d_c associated to the final cluster. Radius of the droplet is 0.215 µm, τ is 0.21 ms .

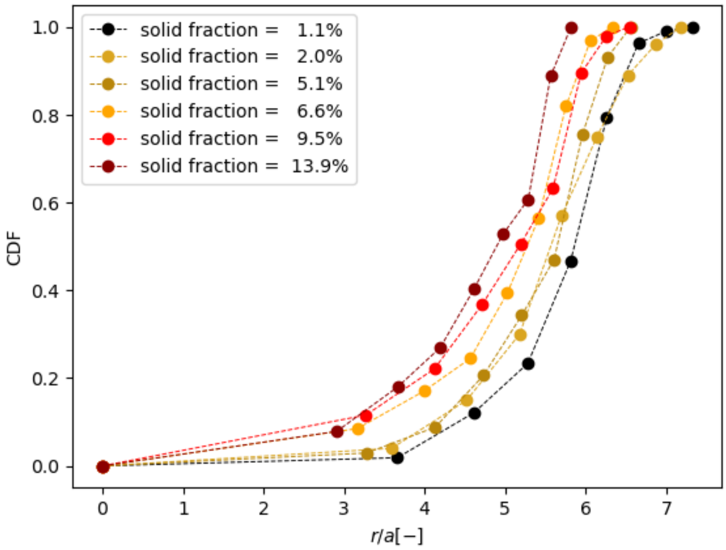

Fig. 3.8 CDF of the particle radial distribution in agglomerates obtained at D equal to zero for different values of the monomer radius a and solid fraction.

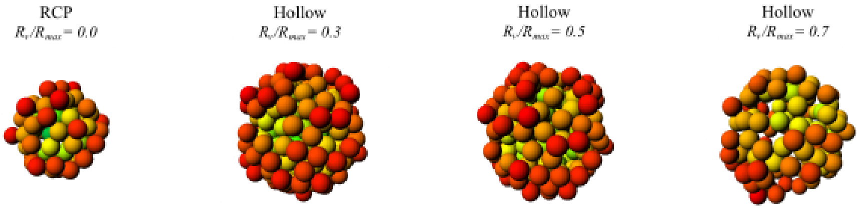

Fig. 3.9 From left to right: Random Close Packing agglomerate; hollow agglomerate generated from an RCP agglomerate by imposing a ratio between the radius of the internal void core R_v and the maximum radius of the original agglomerate R_{max} equal to 0.3; hollow agglomerate with R_v/R_{max}=0.5 ; hollow agglomerate with R_v/R_{max}=0.7 . Green primary particles are close to the centre of mass of the agglomerate, red primary particles are far from it.

drying were compared with notable hollow agglomerates having similar size and different void fractions at their core: R_v/R_{max}=0.3, 0.5, 0.7 . For every class, a=10 nm. Notable hollow agglomerates with R_v/R_{max}=0.7 are similar to agglomerates produced via spray drying also in terms of number of monomers: for both classes, $np \approx 110$. For every class of agglomerates, 10 different but equivalent realizations were analyzed. The different classes were compared on the basis of their size, the ratio h_c/d_c, the average coordination number of the primary particles $\overline{c}_n$ and the CDF of the radial distance of primary particles from the center of mass of the agglomerate. All these properties have been averaged over the entire population of aggregates of a certain type, and angle brackets are used to represent an averaged quantity.

Values of $\langle d_c \rangle$, $\langle h_c/d_c \rangle$ and $\langle \overline{c}_n \rangle$ with the associated standard error bar for every class of agglomerates are shown in Table 3.6, while CDF curves are presented in Fig. 3.10. Every curve is representative of an entire population of agglomerates. Properties of agglomerates generated at $\mathrm{Pe} = 1$ are remarkably close to RCP aggregates with the same number of primary particles in terms of size and compactness, as inferred from the associated ratio $\langle h_c/d_c \rangle$ close to 0.5 and the high coordination number $\langle \overline{c}_n \rangle$ shown in Table 3.6. The distributions of monomers in the cluster is very similar for the two classes of agglomerates, although the external region of agglomerates produced via spray drying (Fig. 3.10, red curve) is more irregular with respect to the well-defined RCP agglomerates (orange curve). The aggregates produced at $\mathrm{Pe} \to \infty$ compare well with hollow aggregates with prescribed internal void core. As the size of the internal void core increases, the average coordination number decreases with respect to compact clusters and the external crust becomes thinner, as highlighted by the ratio $\langle h_c/d_c \rangle$ in Table 3.6 and the cumulative distribution functions in Fig. 3.10 . The shell structure of agglomerates produced via spray drying at high Péclet number is well defined and their properties are similar to artificially generated hollow agglomerates having comparable size and number of monomers.

3.4 Conclusions

DEM simulations of a single-droplet spray drying process make it possible to generate numerically a plurality of agglomerates suitable for the proposed pharmaceutical issue. Moreover, the simulation is able to capture the impact of the most important

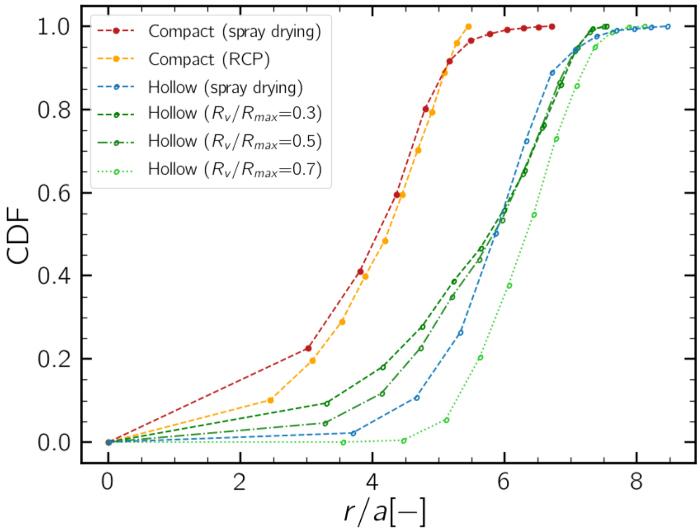

Fig. 3.10 CDF curves of the radial distance of primary particles from the center of mass of the agglomerates. Red: compact agglomerates obtained via spray drying simulations. Orange: RCP compact agglomerates. Blue: hollow agglomerates obtained via spray drying simulations. Green: hollow agglomerates generated from RCP agglomerates by imposing R_v/R_{max}=0.3 (dashed line), R_v/R_{max}=0.5 (dashdot line), R_v/R_{max}=0.7 (dotted line). Every CDF is representative of the entire population.

process conditions, summed up by the Péclet number, on the morphology of the cluster. The resulting agglomerates have been characterized by the ratio between their diameter and their crust, their hyperstaticity, the distribution of primary particles inside the volume of the agglomerate and a comparison with notable and already well-characterized types of agglomerates. After this analysis, two distinct classes have been distinguished: process conditions of low Péclet number led to the forma-

Class	np	a [nm]	$\langle d_c \rangle$ [nm]	$\langle h_c/d_c \rangle$	$\langle \bar{c}_n \rangle$
Compact (spray drying)	~ 90	10	129 ± 5	0.44 ± 0.01	3.83 ± 0.11
Compact (RCP)	~ 90	10	125 ± 1	0.43 ± 0.01	3.13 ± 0.15
Hollow (spray drying)	~ 110	10	163 ± 6	0.31 ± 0.02	3.01 ± 0.04
Hollow (R_v/R_{max}=0.3)	~ 200	10	163 ± 1	0.40 ± 0.02	3.41 ± 0.12
Hollow (R_v/R_{max}=0.5)	~ 180	10	161 ± 5	0.35 ± 0.05	3.15 ± 0.24
Hollow (R_v/R_{max}=0.7)	~ 110	10	168 ± 3	0.26 ± 0.02	2.34 ± 0.06

Table 3.6 Principal characteristics of every class of agglomerates and values of d_c, h_c/d_c and $\bar{c}_n$ averaged over the entire population of different but equivalent realizations.

tion of compact spherical agglomerates with uniform density, whereas in condition of high Péclet number hollow agglomerates were obtained.

At this point, we are able to generate a dataset of dried aggregates, but little has been said about their de-agglomeration in response to hydrodynamic forces. To do so, an improved discrete element method based on Stokesian dynamics is employed in Chapter 4.

Chapter 4

Breakup of agglomerates in simple flows

The chapter is based on the following article written by the candidate: Vasquez Giuliano, L., Buffo, A., Vanni, M., Frungieri, G., "Micromechanics and strength of agglomerates produced by spray drying", JCIS Open, 2023 [20].

Beside the agglomeration process, the mechanical response of the agglomerates to the fluid dynamic stress, i.e., the activation mechanism, has to be investigated as well [12, 13, 103]. To predict the pharmaceutical activity of the drug carriers, a detailed simulation of their behaviour when immersed in a flow field can again be obtained by DEM simulations. [45, 50, 104]. However, different degrees of complexity can be introduced in DEM simulations when modelling the fluid dynamics interactions between the suspending fluid and the solid particles. To simulate the formation of a single agglomerate following the shrinkage of a single droplet containing a suspension of nanoparticles, the so-called free-draining approximation was adopted, i.e. each particle is assumed to experience the Stokes drag force, as if no other particle were in the flow. On the other hand, when hydrodynamic forces are more intense, up to the point the they could lead to a deformation and a breakup of the structure, the hydrodynamic screening effects taking place in the agglomerate are known to play a non–negligible role [48]. These can be accurately taken into account by Stokesian dynamics [56], which, by using a low-order expansion of the exact solution of the flow field, is able to compute the hydrodynamic forces acting on each particle, allowing one to predict particle aggregation [105], but also agglomerate restructuring, and the breakup of soft and rigid agglomerates in both simple flow configurations [46, 51–53] and in complex flow fields [64].

In this Chapter, a compact and a hollow agglomerate obtained by *Yade* simulations are placed in simple flow fields in order to investigate the differences in their response to the same hydrodynamic stress. To this purpose, the complete formulation of the Stokesian dynamics approach is employed. First, accurate simulation of the deformable structure of the agglomerates was performed, obtaining precise and detailed information about their restructuring and breakup. Then, the previous results were compared with the ones obtained adopting the rigid body approximation discussed in Section 2.3.5, to verify the suitability of this assumption for conducting simpler and less time-consuming simulations without an excessive loss in accuracy.

4.1 Complete DEM in extensional flow

Two of the agglomerates produced by spray drying were subject to an elongational flow of gradually increasing intensity in order to investigate the effect of the hydrodynamic stress on the their structure. One of the agglomerates was taken from the population obtained at $\mathrm{Pe} = 1$, the other one from that obtained for $\mathrm{Pe} \to \infty$. The former is a compact aggregate and the ratio h_c/d_c is 0.44 ; The latter is a hollow aggregate and the ratio h_c/d_c is 0.28 . The radius of the primary particles of both agglomerates was $a = 100$ nm. The structural properties of the agglomerates and contacts (ρ_p, E, ν, γ_s) were the same as used in the spray drying simulations and are reported in Table 3.1. The compact agglomerate was formed by 85 monomers and initially had 177 interparticles contacts; the hollow agglomerate was made by 115 monomers with 185 initial interparticle contacts.

Contact forces are extremely sensitive to small changes in the relative position of the particles and even small departures from equilibrium give rise to extremely strong internal stresses. This is why, before studying the effect of the strength of the flow on the agglomerates, the two structures were immersed in a stagnant field for 0.1 s and then in a low-strength elongational flow ($\mu\dot{\gamma} = 2$ Pa) for an additional time of 0.1 s. This procedure allowed the contacting particles to adjust their relative position by reaching their equilibrium separation, making the breakup simulations more stable. The effect of the strength of the flow on the agglomerates was investigated by prescribing an elongational field with strength $\mu\dot{\gamma}$ that was increased linearly at a

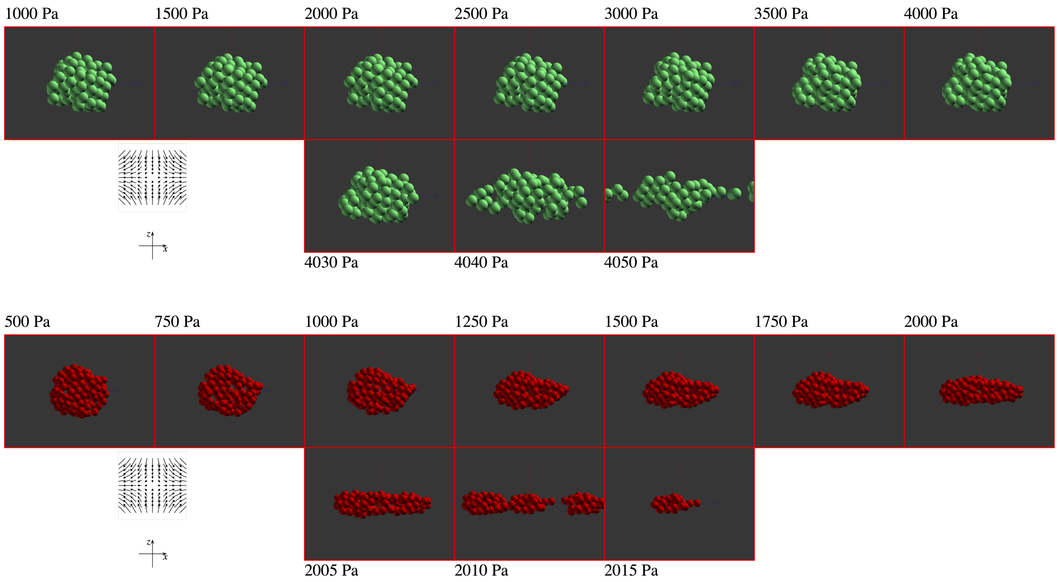

Fig. 4.1 Snapshots of the evolution up to breakup of a compact agglomerate obtained by spray drying in the low Péclet limit (above) and of a hollow agglomerate obtained in the high Péclet limit (below). Both are suspended in an elongational flow of increasing strength $\mu\dot{\gamma}$.

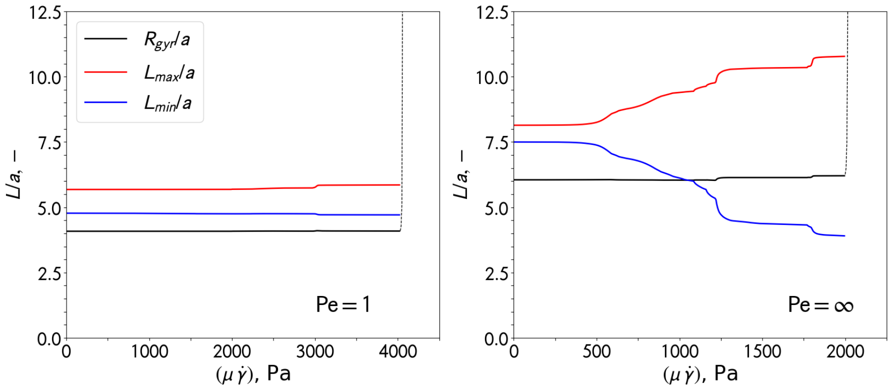

Fig. 4.2 Radius of gyration (black line); size of the largest (red) and smallest (blue) semiaxis of the equivalent ellipsoid for the compact agglomerate, Pe = 1 (left), and the hollow agglomerate, Pe $\to \infty$ (right), during the elongation process as a function of the applied fluid dynamic stress. The dashed line is the radius of gyration after breakup.

constant rate of 5000 Pa/s from 0 Pa until breakup could be observed. A constant time step $\Delta t = 5 \cdot 10^{-8}$ s was adopted in the first-order explicit integration of the translational and rotational equations of motion of all the primary particles.

The response to the fluid dynamic stress and the path to breakup is quite different for the two agglomerates considered, as made apparent in Figure 4.1, which reports a series of snapshots of the agglomerates taken at subsequent times and increasing values of stress. The compact one remained almost completely undeformed until a few moments before rupture. In the very initial stage ($\mu \dot{\gamma} < 1000$ Pa) it rigidly rotated until aligned with the fluid velocity direction. Between 1000 and 4000 Pa there was no significant movement of the agglomerate or deformation, except for the small sliding of few monomers on the surface of the structure. At 4020 Pa the agglomerate began to deform significantly by stretching in the x-direction of the flow; rupture occurred immediately thereafter, at around 4040 Pa. As shown in Fig. 4.2, the radius of gyration of the agglomerate did not change from the beginning of the application of the flow field until a few moments before rupture. In order to better characterise the geometry change, the agglomerate was also approximated by the triaxial ellipsoid with the same inertia tensor. The shortest and longest semi-axes of this ellipsoid, which represent the characteristic sizes of the agglomerate [106, 107] are also plotted as a function of time in Fig. 4.2. These variables remained constant during the process, except for a small variation at 3000 Pa due to the partial sliding of single monomers. This behaviour confirmed that the agglomerate was practically rigid until breakup, which therefore occurred in a brittle manner. The number of monomer-monomer contacts was 177 at the beginning of the simulation and remained constant at this value till 1500 Pa; after that, it increased slowly and steadily because of the compression in the z-direction until it reached 185 contacts shortly before breakup. The variation of the average coordination number $\bar{c}_n$ was extremely small, from 4.16 to 4.35, further showing that the structure of the agglomerate remained almost unchanged till breakup occurred.

In the hollow agglomerate the deformation of the structure before breakup was more significant (Fig. 4.1, bottom). Here too, there was an initial phase (up to 1000 Pa) of alignment with the flow field, but the structure remained rigid only up to about 600 Pa. At stresses larger than this, it began to flatten in the z-direction and to stretch in the x-direction. This effect is made quantitatively apparent by the change in the size of the semi-axes of the triaxial ellipsoid reported in Figure 4.2 (right), where the largest semiaxis, aligned with x throughout the deformation process, increases, whereas the smallest one, aligned with z, decreases. It is worth to notice that the radius of gyration was unable to reflect this deformation phenomena, because the simultaneous effect of compression along z and elongation along x balanced each other, such that the average distance of the primary particles from the centre of mass of the agglomerate remained almost unchanged. Results also made apparent that the flattening effect made the structure more rigid and in fact between 1200 and 1800 Pa the agglomerate was not subject to further deformation. Around 1800 Pa restructuring started again further flattening the agglomerate; then the structure remained stable until rupture, which took place between 2005 and 2010 Pa. It must be noted that during the entire process the structure did not collapse on itself completely but the internal cavity was preserved. The variation in the number of inter-particle contacts was here significant. They remained constant at 183 up to 600 Pa, then increased steadily with the partial flattening of the structure up to 199 at 1400 Pa and finally remained again constant until rupture. The average coordination number is quite high, but smaller than the previous case, because of the presence of the cavity; it varied from 3.18 at the beginning of the process to 3.46 just before breakup.

4.2 Rigid body approximation

In the DEM approach used in Section 4.1, processes acting at very different scales had to be simulated simultaneously. Hydrodynamic interactions and the large scale motion of the agglomerate took place on lengths of the order of the size of the agglomerate, whereas contact forces and local deformations of the contact area act on distances that could be smaller than 1 nm. As a consequence, the time step had to be extremely small in comparison to the duration of the process and the simulations were very slow and required substantial computational resources. However, it was apparent that, because of the high coordination number and the strength of the internal bonds, the compact agglomerate behaved almost like a rigid body until rupture. This behaviour suggested that relevant information on the breakup of the agglomerate can be obtained by simpler and much less time-consuming simulations. In the limit of small deformation and brittle fracture we can in fact apply the methods of the structural mechanics of rigid bodies discussed in Section 2.3.5 to determine

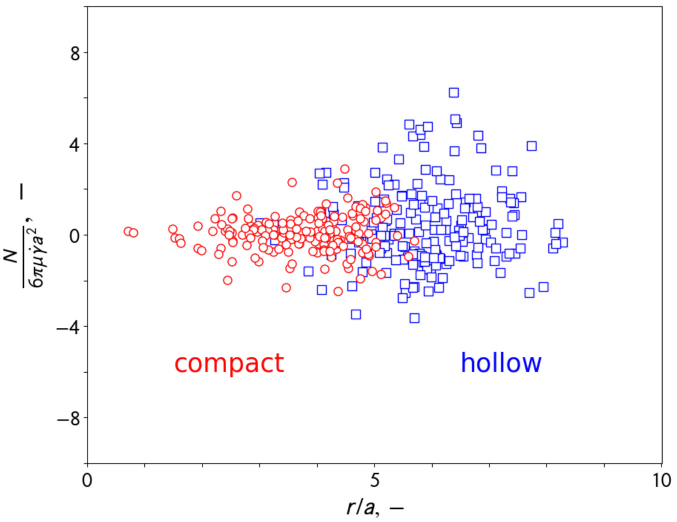

Fig. 4.3 Distribution of the normal stress at contact as a function of the distance r from the center of mass for the two agglomerates calculated from DEM under the rigid mody motion assumption. Red circles: compact agglomerate. Blue squares: hollow agglomerate.

how the hydrodynamic forces are redistributed as contact stresses over the particle network.

In the rigid body assumption limit, we assumed that breakup occurs when the normal stress exceeds the pull off force at one intermonomer bond. The distribution of intermonomer stresses for the compact agglomerate calculated by the rigid DEM is shown in Figure 4.3 by red circles as a function of the radial distance from the center of mass. The highest value for the compact agglomerate was $N_{max}/(6\pi\mu\dot{\gamma}a^2) = 2.89$, which should be compared with the pull-off force given by Eq. 2.52. In this way the critical shear stress for the breakup of the most stressed bond is $\mu\dot{\gamma}_{br} = 4120$ Pa, which compares considerably well with the value of 4040 Pa obtained by the complete DEM simulation. Most remarkably, and in some way unexpected, is what happened when the rigid DEM is applied to the hollow agglomerate (blue squares in Figure 4.3). The largest value of dimensionless normal stress was $N_{max}/(6\pi\mu\dot{\gamma}a^2) =$ 6.24, which gave rise to a critical shear stress of 1930 Pa. Even in this case the prediction of the rigid DEM was more than satisfactory when contrasted with the value given by the rigorous DEM (2010 Pa), although the assumption of stiffness is not fully valid in this case and the agglomerate underwent some restructuring before breaking up. However, apparently, the restructuring was not strong enough to significantly change the morphological features of the agglomerate, which preserved the central cavity and the cross-linked network of bonds until breakup. Therefore, the assumption of rigid agglomerates well predicted the different mechanical stability of the two classes of agglomerates, and it has been imposed for all the subsequent simulations.

Rigid DEM simulations based on Stokesian dynamics were conducted on a population of 10 compact agglomerates produced at $Pe = 1$ and 10 hollow agglomerates produced at $Pe \to \infty$ placed in a shear flow. As already commented, the physical deformation process leading to breakup through restructuring and detachment of fragments is not simulated under the condition of rigid body motion; however, valuable insights about the distribution of the contact forces inside the agglomerates can be obtained and the mechanical stability of the two classes can be compared.

Figure 4.4 shows the instantaneous value of the maximum tensile normal contact force N_{max} acting inside agglomerates suspended in a shear flow with constant shear rate $\dot{\gamma}$. Both time and maximum tensile stress are made dimensionless, exploiting the linearity between internal contact forces and applied hydrodynamic stress valid in the elastic regime. Each line refers to a single agglomerate, and blue lines are used for hollow agglomerates, red for compact ones. One arbitrary line for each class is highlighted to show the typical trend followed by N_{max} in a shear flow. The oscillation of N_{max} is due to the rotation of the rigid agglomerate in the shear flow, which exposes periodically different bonds to the orientation of maximum stretching. The two horizontal lines represent the maximum tensile stress experienced by an agglomerate along its whole path, averaged over the entire class. The dimensionless value for hollow and compact agglomerates was around 5.1 and 3.3, respectively. Such values correspond to a critical fluid dynamic shear stress $\mu\dot{\gamma}$ of 2360 Pa and 3650 Pa, respectively. At such stresses the normal contact force reaches the pull-off value. Hollow agglomerates experienced higher internal tensile forces, meaning therefore that are easier to break. Compact agglomerates are more hyperstatic, i.e. every particle is linked to a higher number of different particles; therefore, mechanical stress is discharged over neighbouring particles and thus stronger externally imposed hydrodynamic forces are needed to break their bonds, as observed for the elongational flow.

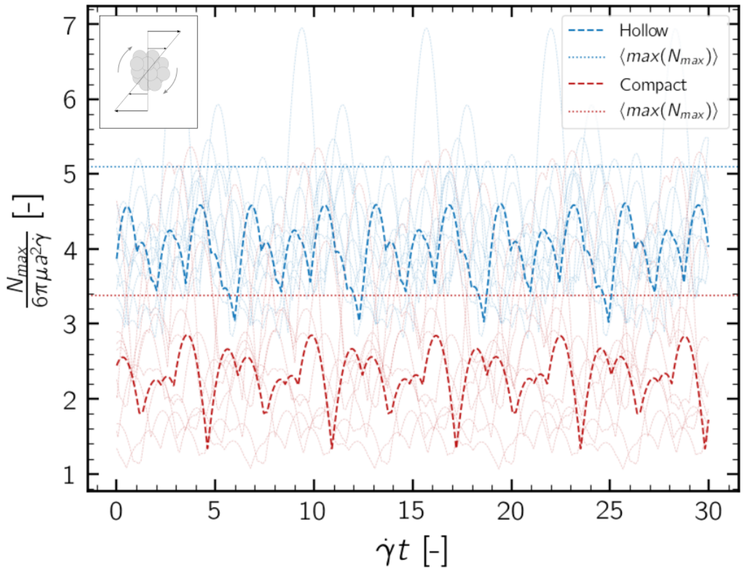

Fig. 4.4 Maximum tensile stress N_{max} acting inside a agglomerate in a shear flow. Blue curves: shell-type agglomerates produced at Pe $\rightarrow \infty$. Red curves: compact agglomerates produced at Pe $= 1$. Horizontal dotted lines show the average value of the maximum tensile stress experienced by a agglomerate along its path for the two classes of agglomerates. In the inset, a qualitative representation of the simulation setup and of the shear flow is given.

4.3 Conclusions

The mechanical response of agglomerates to a simple flow field has been investigated thanks to DEM simulations based on Stokesian dynamics. Moreover, we have linked the conditions required for de-agglomeration with the operating conditions of the spray drying step: compact agglomerates produced at Pe $= 1$ require high viscous forces to break, while the breakage of hollow agglomerates obtained at Pe $\rightarrow \infty$ is easier. It has to be noticed that the behaviour of such agglomerates is almost rigid up to their breakup: therefore, the rigid body approximation can be employed in following simulations to save computational cost without losing accuracy.

Finally, the behaviour of compact and hollow agglomerates has to be investigated in the context of the proposed pharmaceutical issue: DEM simulations of rigid agglomerates have to be conducted in the flow field generated in presence of an arterial occlusion. To do so, computational fluid dynamics is employed to extract information about the flow field in an obstructed vessel. The coupling between CFD and DEM will provide valuable insights about the response of dried aggregates to the pathological increase of fluiyd-dynamic stress caused by the occlusion.

Chapter 5

Breakup of agglomerates in complex flows

5.1 Introduction

The chapter is based on the following article written by the candidate: Vasquez Giuliano, L., Buffo, A., Vanni, M., Lanotte, A. S., Arima, V., Bianco, M., Baldassarre, F., Frungieri, G. , "Response of shear-activated nanotherapeutic particles in a clot-obstructed blood vessel by CFD-DEM simulations", The Canadian Journal of Chemical Engineering, 2022 [19].

A microfluidic device representing an obstructed blood vessel was designed for experimental purposes, and the flow field inside the device was characterized using CFD. The behaviour of drug carriers that encounter an obstruction was numerically investigated in the microfluidic device and in obstructed arteries with different morphology. Given their small size and inertia, the agglomerates follow the streamlines of the fluid very closely and thus can be treated as tracer particles. Hence, by integration of the fluid velocity, we computed a set of tracer particle trajectories in order to evaluate the hydrodynamic stress time series clusters are subjected to, which can in turn be used to evaluate their internal stresses. In other words, information about the hydrodynamic stress exerted by the fluid obtained from CFD has been coupled with the DEM method based on Stokesian dynamics to investigate the fragmentation occurring for drug carriers flowing in this pathological complex flow.

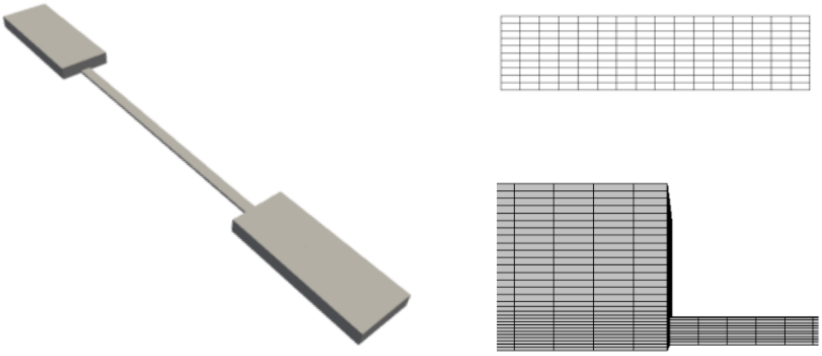

Fig. 5.1 Geometry, minimum cross-section shape and mesh detail for the microchannel. The minimum cross-section of the microchannel is a rectangle with sizes of 95 µm and 400 µm.

5.2 The microchannel

5.2.1 Setup of the simulation

The microfluidic device is shown in Figure 5.1. It has a rectangular section, and it is formed by a central stenotic tract (95 µm high x 400 µm wide x 10 mm long) and by a pre- and post-stenotic tract (each: 495 µm high x 2 mm wide x 5 mm long), corresponding to a 95% lumen obstruction. The viscosity of the fluid in the simulations was set to 10^{-3} Pa·s, and the density to 1000 kg/m^3. The flow travels a distance in the pre-stenotic region that is sufficient to reach the condition of fully-developed flow at the stenotic region entrance. The boundary condition that has been prescribed is a pressure difference between the inlet and outlet, to better reproduce the operative conditions that would be encountered in the actual experimental apparatus: the fluid is fed to the microchannel through cylindrical tubes linked to its upper part, thus not achieving a uniform velocity profile at the inlet of the vessel. Wall boundary conditions were applied on the lateral surfaces. The flow rate was adjusted according to a trial and error procedure until pathological values of the shear stress were reached in the restricted region (order of magnitude is 10^2 Pa). The simulation domain was subdivided using 98720 hexahedral cells.

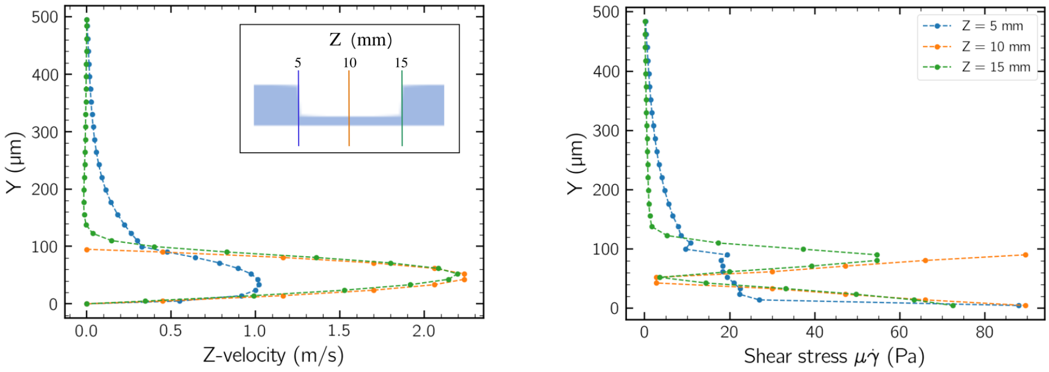

Fig. 5.2 Microchannel flow field. Z-velocity (left) and $\mu\dot{\gamma}$ profile (right) in the symmetry plane along the coordinate Y at three different coordinates Z. Z = 5 mm is the beginning of the stenotic tract, Z = 10 mm is its middle point, and Z = 15 mm is its end.

5.2.2 Flow field

First, transient simulations of the flow field in the vessel were conducted. The flow field was seen to quickly reach a stationary solution, so steady-state simulations have been used in the following to characterize the fluid dynamic behaviour of the obstructed vessels. Wall shear stresses greater than 100 Pa are considered pathological [11]. Two pathological conditions were investigated: the flow rate was tuned to reach a maximum wall shear stresses of 125 and 183 Pa, obtained for a volumetric flow-rate of around 1.10 and 1.50 ml/min, respectively.

The profiles of Z-velocity and $\mu\dot{\gamma}$ before, in the middle and after the restricted section are reported in Figure 5.2. A recirculation pattern can be seen from the Z-velocity plot at the end of the restricted section. The obstruction, therefore, causes a recirculation in the post-stenotic region, which is considered to be beneficial for the action of shear responsive agglomerates [11], as it keeps the fragments generated upon breakup near the wall of the stenotic region, thus increasing the probability of adhesion to the clot. In Figure 5.2, the shear stress profiles in the microchannel are reported on the right. The peak value of wall shear stress is due to the strong deformation of the flow field at the entrance of the restricted section, and it is reached at the very beginning of the stenotic region. Figures 5.3A and 5.3B make this feature more apparent, by showing the profile of wall shear stress along Z on the symmetry plane of the microchannel, both on the upper and the lower wall, and the strain rate contour plot on the same plane. The peak value of 183 Pa of the shear stress is

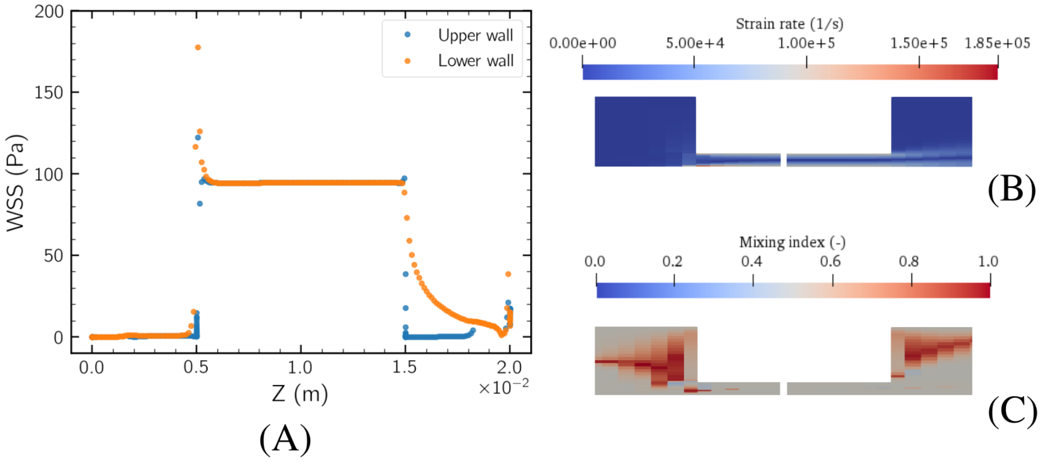

Fig. 5.3 Microchannel flow field characterization for an inlet flow-rate of 1.50 ml/min. (A) Axial profile of wall shear stress on the upper wall and the lower wall. Contour plot of (B) strain rate, and (C) mixing index on the symmetry plane

reached at the bottom wall of the device, soon after the beginning of the restricted section, and then it reaches a plateau value equal to 95 Pa.

In addition to the strain rate, the flow field was locally characterized also by the mixing index λ, defined and discussed in Section 2.4. As made apparent by the contour plot of λ reported in Fig. 5.3C, even if the lumen restriction causes a local increase in the elongational component of the flow, in the regions where the largest stresses are observed, the value of mixing index is around 0.5, thus indicating that pure shear flow conditions are present in those regions.

5.2.3 Fragmentation in the microchannel

The mechanical response of the agglomerates to the viscous stress was computed by running Stokesian dynamics simulations along the trajectories obtained via the interpolation of the flow field. Given the small size of the clusters, trajectories were computed using a one-way coupling, neglecting the back reaction of the clusters on the fluid and the binary interaction between them. Shear rate signals have been translated into tensile stress acting on each particle–particle bond, thanks to Stokesian dynamics. As an example, Figure 5.4 illustrates the outcome of the method for two generic agglomerates when immersed in a pure shear flow. The upper images show the drag forces acting on each primary particle of the agglomerate,

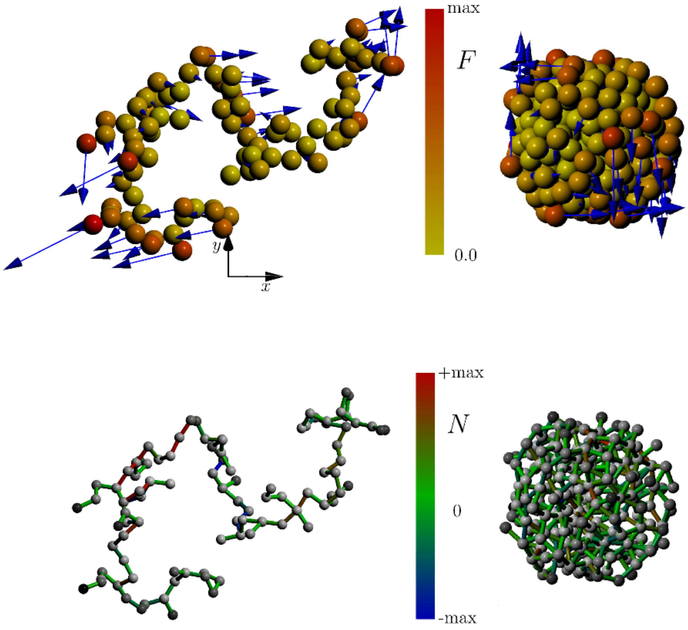

Fig. 5.4 Drag forces (above) and normal stresses at intermonomer bonds (below) for two different agglomerates under a shear flow.

whereas the lower ones report the normal (i.e., tensile) forces acting at inter-particle contacts. It is worth remembering that, for rigid agglomerates, breakup takes place when the tensile normal stress exceeds the cohesive strength at a contact, and, subsequently, the normal stress is the fundamental variable to predict the occurrence of breakup. Although subject to the same flow field, the distribution of the normal stress in two agglomerates can be very different, as made more clear by recalling Figure 4.3, showing the distribution of the normal stresses at contact in two different agglomerates. In the compact agglomerate, the strength of the normal force is small in comparison to what can be observed in the hollow agglomerate, where the average coordination number is lower and it is harder for particles to discharge the accumulated stress to neighbouring particles. It is apparent, therefore, that the stresses acting on the agglomerates depend on both their geometry and the local strain rate.

In Figure 5.5, we report a sample strain rate signal (Eq. 2.127) and the maximum instantaneous tensile stress N_{max} acting in the agglomerate. The maximum normal stress is normalized using $6\pi\mu a\langle u\rangle$, where $\langle u\rangle$ is a representative velocity of the fluid. In this case, the mean velocity in the stenotic region of the microchannel has been chosen, $\langle u\rangle$=1.1 m/s . It is worth noting that there is no time lag between the

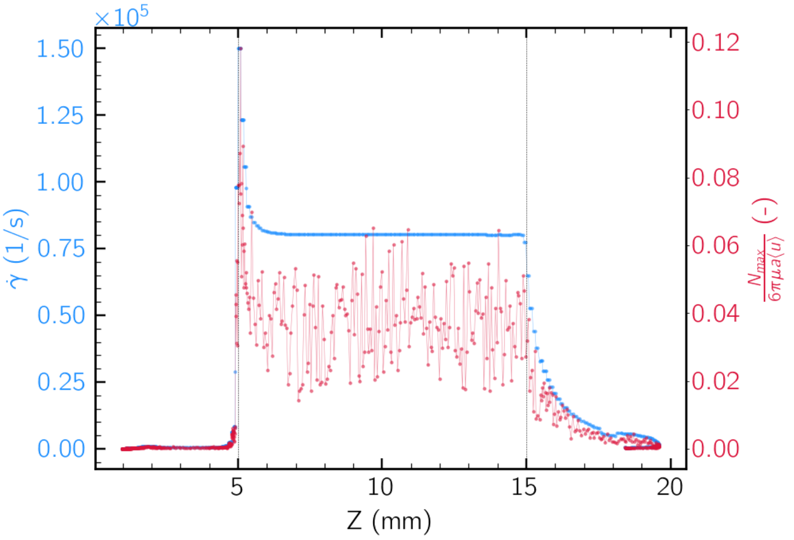

Fig. 5.5 Strain rate $\dot{\gamma}$ (blue) and normalized maximum tensile stress N_{max} inside a compact agglomerate (red) along the Z-coordinate for a sample trajectory in the microchannel. The fluctuating behaviour of N is due to changes in the orientation of the cluster with respect to the flow field.

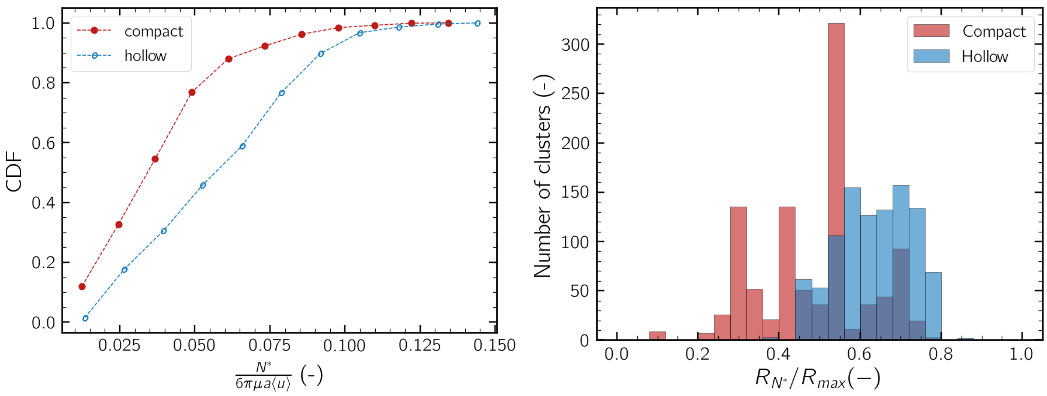

Fig. 5.6 Left: cumulative distribution functions (CDF) of the maximum normal stress inside clusters flowing in the microchannel. Red: compact agglomerates, Blue: hollow agglomerates. Right: Relative position of the most solicited bond for the two classes of agglomerates.

two signals. This is due to the fact that agglomerates are supposed to be perfectly rigid, and hence the transmission of the stress from the flow field to the agglomerate structure occurs instantaneously.

Finally, we studied the mechanical response of the different classes of clusters produced via spray drying to the hydrodynamic solicitation. Again, the population of 10 compact and 10 hollow agglomerates discussed in previous sections has been considered. Figure 5.6 (left) reports the cumulative distribution function of $N^* = max(N_{max})$, the maximum tensile stress experienced by a cluster along its entire trajectory in the microchannel. It can be noted that, as expected, compact agglomerates emerged as the most resistant class, while hollow agglomerates emerged as the weakest one. In other words, the maximum tensile stresses observed in compact clusters is lower than the one observed in hollow clusters.

The effective restructuring and the eventual breakup of agglomerates cannot be observed using the rigid body approximation: however, the location of the most stressed bonds is known, and this leads to legitimate considerations about the breakup mechanism. Figure 5.6 (right) shows the position of the most loaded bond for every cluster. R_{N^*} is the distance of the most loaded bond from the center of mass, normalized over the maximum radius of the agglomerate. Both compact and hollow agglomerates are hyperstatic, that is, every primary particle is linked to a large number of particles. Therefore, the mechanical stress generated on the outer region is discharged over the neighbouring particles, and it is not propagated and

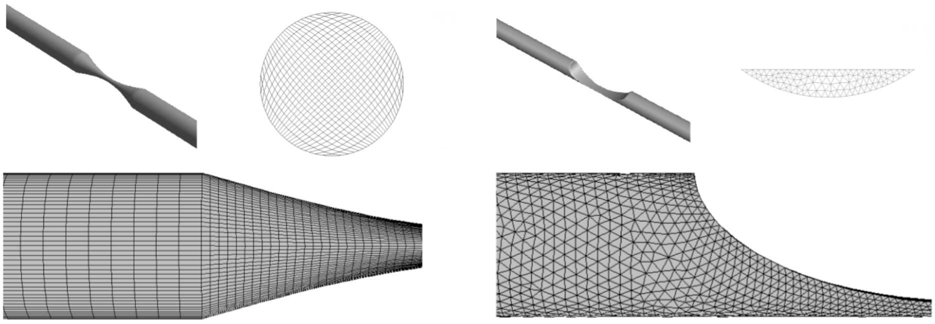

Fig. 5.7 Geometry, minimum cross-section shape, and mesh detail for the axisymmetric occlusion (Left) and the asymmetric occlusion (Right). The minimum cross-section of the axisymmetric occlusion is a circle with a diameter equal to 220 μm. The minimum cross-section of the asymmetric occlusion is a circular segment and its height is 105 μm.

accumulated toward the inner region of the agglomerate. The highest loaded bonds are thus located in its outer region. In compact agglomerates, the breakup should lead to the detachment of small fragments from their outer surface. The distribution of mechanical forces inside the hollow agglomerates is similar, but the distance over which stresses are propagated is limited by the shell-shape of the agglomerates. In this case, therefore, the breakup of outer bonds should be expected to lead to the opening of the shell structure.

5.3 Other geometries

The microfluidic device has been designed for experimental evaluation of the deagglomeration of drug carriers. In order to verify its ability to reproduce the pathological conditions occurring in an obstructed vessel, the hydrodynamic stress exerted by a fluid flowing in the microchannel has been compared with the one occurring in different and more realistic representations of an occluded blood vessel. Although clots in stenotic vessels come in a variety of shapes and sizes, axisymmetric or asymmetric deformed cylindrical tubes have been frequently employed as model representations [108–111], and thus these two geometries have been investigated. The geometries of the two investigated systems are shown in Figure 5.7. The axisymmetric geometry models the artery as a cylinder (diameter D_v=1.12 mm), while the shape of the stenosis is described by a sinusoidal curve. In the asymmetric geometry, the pre-stenotic region is equal to the one from the previous case, but

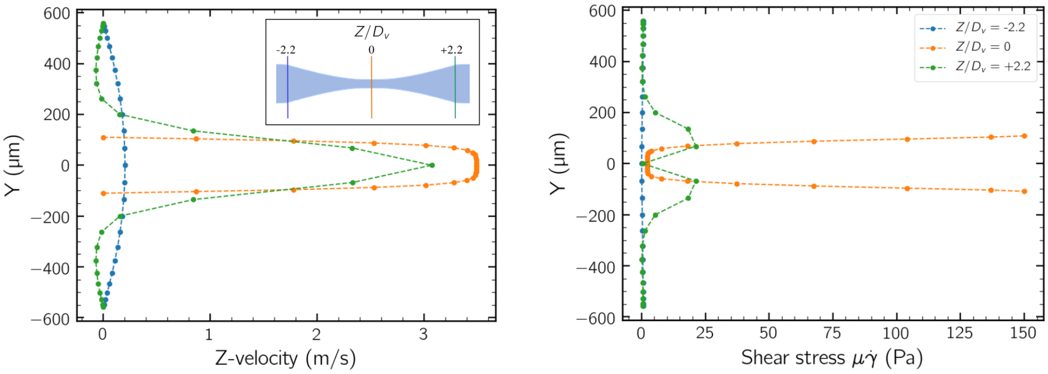

Fig. 5.8 Axisymmetric occlusion flow field. Z-velocity (left) and $\mu\dot{\gamma}$ profile (right) in the symmetry plane along the Y-coordinate at three different Z-coordinates. Z/D_v = -2.2 is the beginning of the stenotic section, Z/D_v = 0 is its middle point, and Z/D_v = +2.2 is its end.

the shape of the clot is instead described by a semi-ellipse, having a major axis of 2.24 mm and a minor axis of 1.015 mm. The major axis of the semi-ellipse is aligned with the flow direction, and the obstruction in the blood vessel is obtained by extruding the semi-ellipse in the orthogonal direction. The lumen obstruction is again 95%. The flow rate has been adjusted in order to reach the same pathological shear stress observed in the microchannel. A uniform velocity profile has been set at the inlet of the axisymmetric and the asymmetric occlusion. Again, wall boundary conditions were applied on the lateral surfaces, and an outflow boundary conditions was imposed at the outlet. The simulation domain was subdivided using 139375 hexahedral cells for the axisymmetric vessel, and 157330 tetrahedral cells for the asymmetric vessel.

5.3.1 Axisymmetric occlusion

The flow rate has been tuned to reproduce the pathological wall shear stresses of 125 and 183 Pa investigated in the microfluidic device. The boundary conditions leading to pathological wall shear stress are an inlet velocity of 0.075 m/s and 0.10 m/s, respectively. Figure 5.8 shows velocity and stress profiles at the beginning, center, and end of the stenotic region for an inlet velocity of 0.10 m/s. It can be seen that the fluid reaches a peak velocity of 0.20 m/s in the pre-stenotic region and a peak of 3.62 m/s in the stenotic region. As apparent from the velocity profile after the restricted section (at Z = +2.2D_v), the fluid generates a slowly decaying central jet surrounded by two lateral vortices. Therefore, also in this case a recirculation pattern

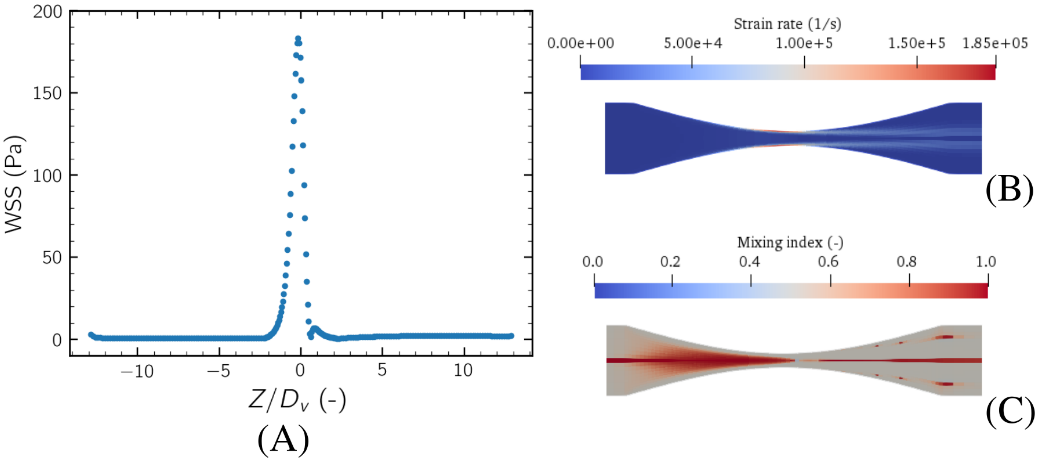

Fig. 5.9 Axisymmetric occlusion flow field characterization for an inlet velocity of 0.1 m/s . (A) Axial profile of the wall shear stress. (B) Contour plot of the strain rate and (C) mixing index in longitudinal cross-section.

is visible in the post-stenotic region. The shear stress profile of Figure 5.8 (right) makes it apparent that the largest shear stresses are found in the restricted section, and they are located in the region closest to the wall.

The effect of the restriction on the shear stress distribution is highlighted also in Figure 5.9A, where the maximum wall shear stress is plotted as a function of the longitudinal coordinate. The stress at the wall increases from about 0.4 Pa before the obstruction to a maximum of 183 Pa on the restricted section. The distribution of the strain rate is shown in Figure 5.9B. It can be noticed that the region of highest strain rate is located close to the wall in the converging and central region of the vessel, and it moves closer to the centre-line in the diverging region, at the transition between the fluid jet and the recirculation zones, thus suggesting that this region could contribute, even if to a lesser extent, to the breakup of the suspended drug carriers. The contour plot of the mixing index on a symmetry plane (Figure 5.9C) shows that the flow is shear-dominated and elongation is only present in the pre- and post-stenotic regions, as observed in the microchannel.

5.3.2 Asymmetric occlusion

Similarly to what has been done for the axisymmetric vessel, we ran simulations at different inlet velocities in the asymmetric vessel in order to determine the conditions

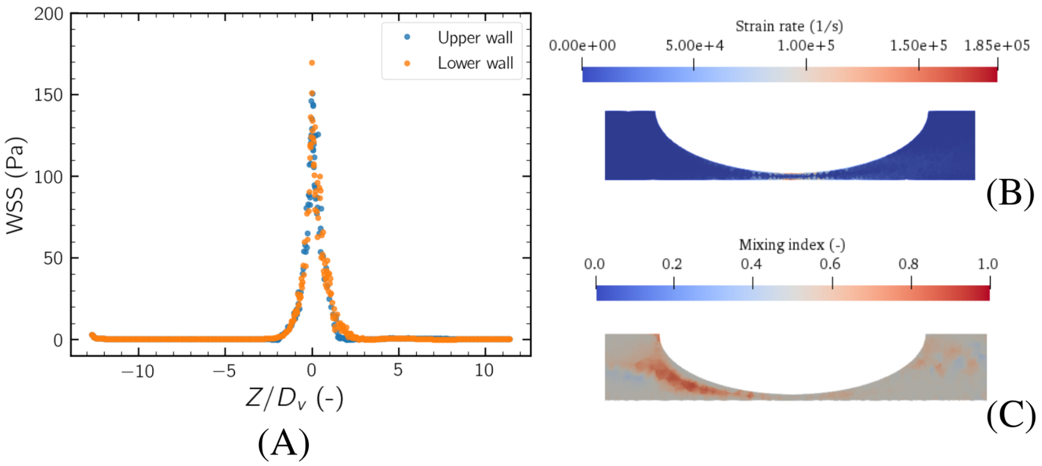

(A) (B) (C)

Fig. 5.10 Asymmetric occlusion flow field characterization for an inlet velocity of 0.067 m/s. (A) Axial profile of wall shear stress on the upper and lower wall. Contour plot of (B) shear rate and (C) mixing index in the symmetry plane.

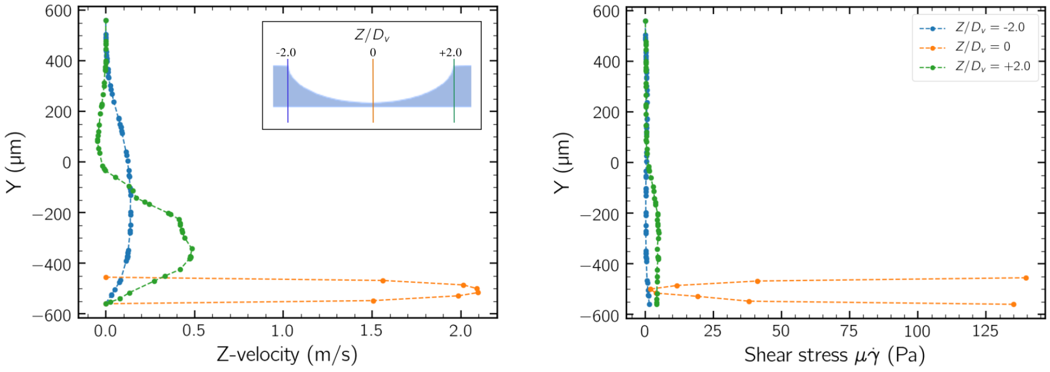

Fig. 5.11 Asymmetric occlusion flow field. Z-velocity (left) and $\mu\dot{\gamma}$ profile (right) in the symmetry plane along the coordinate Y at three different coordinates Z. Z/D_v = -2.0 is the beginning of the stenotic tract, Z/D_v = 0 is its middle point, and Z/D_v = +2.0 is its end.

leading to pathological wall shear stress (125 and 183 Pa). These have been found for an inlet velocity of 0.051 and 0.067 m/s, respectively. Figure 5.10A shows the distribution of the wall shear stress for the upper and lower walls of the vessel. It can be seen that the largest shear stress appears again in the restricted section, with no remarkable difference between the upper and lower walls. The mixing index and strain rate distributions reported in Figure 5.10B,C show that the flow field is mostly shear-dominated in the region of large shear stress, with elongational components of the flow arising only in the small regions before and after the restriction.

In Figure 5.11, we report the velocity profile and the shear stress profile on three different sections. In the plot on the left, it can be seen that the fluid reaches a peak velocity of 0.13 m/s in the pre-stenotic region and a peak of 2.2 m/s in the stenotic region. The negative values of the velocity at $Z/D_v = 2.0$ show that, also in this case, a recirculation pattern establishes in the post-stenotic region. Such a behaviour was seen to emerge at a Reynolds number greater than 200. The stress profile $\mu\dot{\gamma}$ for three different Z-coordinates is reported in Figure 5.11 (right). Again, the maximum shear stress is observed near the walls of the vessel in the restricted region.

5.3.3 Comparison with the microfluidic device

The main properties of the flow field in the three investigated geometries are reported in Table 5.1 and Table 5.2. The typical Reynolds number in blood vessels spans from 1 to 4000 for small arteries and the aorta, respectively [112]; in our simulations, it ranges between 50 and 800 and it is comparable with the one obtained in vessels having similar diameter [113]. It is worth to notice that different flow rates are needed to reach the same pathological wall shear stress in the three systems: nonetheless, an adequate tuning of the flow rate in the microfluidic device is sufficient to match the peak in the hydrodynamic forces exerted by the fluid in an obstructed blood vessel. The higher the strain rate is, the more intense hydrodynamic forces acting on clusters are: therefore, the maximum value of strain rate along a trajectory $\dot{\gamma}_{max}$ can be used as a parameter to compare the effectiveness of the different vessel geometries in inducing breakup. A statistical analysis on the maximum shear rate experienced by agglomerates flowing in the three vessels is presented in Figure 5.12. The plot shows the cumulative distribution function of the peak value of strain rate experienced by the agglomerates along trajectories in the three geometries for a maximum wall shear stress of 125 and 183 Pa, respectively. It can be seen that the

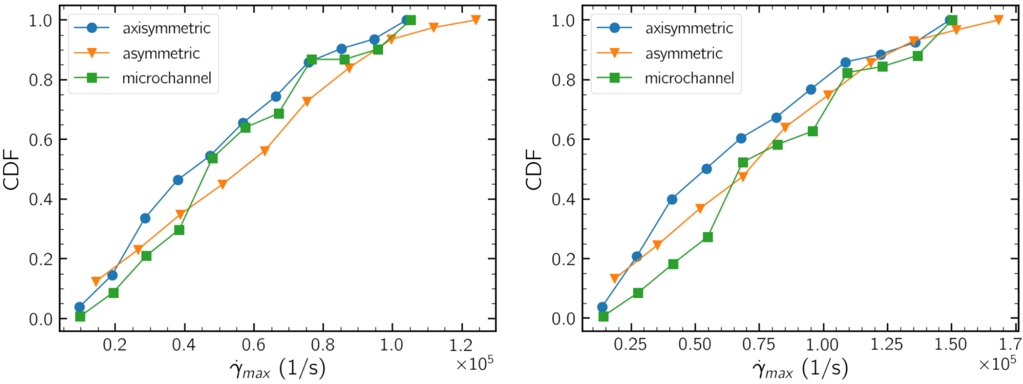

Fig. 5.12 Cumulative distribution functions (CDF) of the maximum strain rate $\dot{\gamma}_{max}$ along trajectories; circles represent the axisymmetric stenosis, triangles represent the asymmetric stenosis, and squares represent the microchannel. Left: maximum wall shear stress=125 Pa. Right: maximum wall shear stress = 183 Pa

shear rate statistics acting on the agglomerates in the microchannel well compares with the one experienced in the obstructed vessels, thus proving our microfluidic device as a valid representation of an obstructed blood vessel and a valid setup for running experimental trials. The longer restricted section of the microchannel in comparison to the stenotic systems has no impact on the distribution of $\dot{\gamma}_{\mathrm{max}}$, but it is expected to facilitate the separation of the fragments after breakup.

Stenosis	Region	Flow-rate (ml/min)	$\tilde{U}_{max}$ (m/s)	R_H (µm)	*Re*
Axisymmetric	Pre-stenotic	4.43	0.15	280	168
	stenotic		2.84	55	625
Asymmetric	Pre-stenotic	3.01	0.10	280	112
	stenotic		1.73	35	242
Microchannel	Pre-stenotic	1.11	0.07	200	56
	stenotic		1.66	40	266

Table 5.1 Principal properties of the flow field for the lowest flow-rate (maximum wall shear stress = 125 Pa) for the three geometries. $\tilde{U}_{max}$ is the maximum fluid velocity in a vessel, R_H is the hydraulic radius.

5.4 Conclusions

The characterization of an obstructed vessel through computational fluid dynamics clearly shows that the presence of the occlusion causes a significative local increase in the shear stress because of the induced distortion of the flow field. The more obstructed the lumen is, the more the hydrodynamic stress increases: a severe occlusion induces a pathological shear stress that is orders of magnitude higher than the regular condition. The subsequent peak in the mechanical tensions provoked in bodies flowing in the vessel acts as a trigger for the breakup of drug carriers, releasing the active agent by breaking up into fragments that are more likely to adhere to the clot walls and perform the thrombolytic action. Moreover, results from the microfluidic device and realistic reproductions of an obstructed blood vessel are comparable: therefore, the de-agglomeration of drug carriers can be simulated and experimentally observed in the microfluidic device without a significant loss in accuracy.

Information about the flow field in the microchannel are fed as an input to DEM simulations based on Stokesian dynamics to track the response of agglomerates produced via spray drying to the stress induced by hydrodynamic forces. Low mechanical tensions are found in compact clusters, and highest tensile stresses are found at the perifery of the agglomerate, suggesting erosion as the prevalent breakup mechanism. Bonds between nanoparticles in hollow clusters are subject to relatively high tensile stresses, eventually leading to the collapse of the shell structure.

Stenosis	Region	Flow-rate (ml/min)	$\tilde{U}_{max}$ (m/s)	R_H (µm)	Re
Axisymmetric	Pre-stenotic	5.90	0.20	280	223
	stenotic		3.62	55	794
Asymmetric	Pre-stenotic	3.96	0.14	280	156
	stenotic		2.21	35	300
Microchannel	Pre-stenotic	1.50	0.09	200	63
	stenotic		2.24	40	357

Table 5.2 Principal properties of the flow field for the highest flow-rate (maximum wall shear stress = 183 Pa) for the three geometries. $\tilde{U}_{max}$ is the maximum fluid velocity in a vessel, R_H is the hydraulic radius.

Chapter 6

Conclusions and open questions

This thesis was devoted to verify the feasibility of shear-responsive drug carriers as an efficient drug delivery system for the treatment of arterial occlusions, and to take the first steps to the establishment of a simulation framework able to follow the lifetime of the carriers from the agglomeration via spray drying to the shear-inducted de-agglomeration. A discrete element method taking into account capillary force, Brownian force and adhesive forces was used to track the motion of colloidal primary particles inside a shrinking droplet. This DEM method was implemented in the open-source software *Yade*, and relies on the free–draining approximation, i.e., all fluid-mediated particle-particle interactions are neglected. Therefore, the spray drying process is simulated at the single droplet scale, resulting in the formation of secondary particles to be treated as drug carriers. The DEM approach was employed also to simulate the de-agglomeration of the drug carriers when exposed to notable hydrodynamic forces. However, a refinement of the method was necessary to effectively track the restructuring and the breakup of agglomerates when exposed to high shear flow, and it was obtained by resorting to Stokesian dynamics, implemented in an *in-house* code. In this way, the viscous forces responsible for rupture are accurately modelled and predicted, along with the mechanical stress distribution within the clusters of primary particles. Computational fluid dynamics techniques were adopted to fully characterize the flow field inside a microfluidic device. The simulation results were compared with the flow field encountered in more realistic representations of an obstructed blood vessel, and then the results were fed as an input to the Stokesian dynamics simulations. The response of drug carriers produced via spray drying to the pathological flow field encountered in an obstructed blood vessel

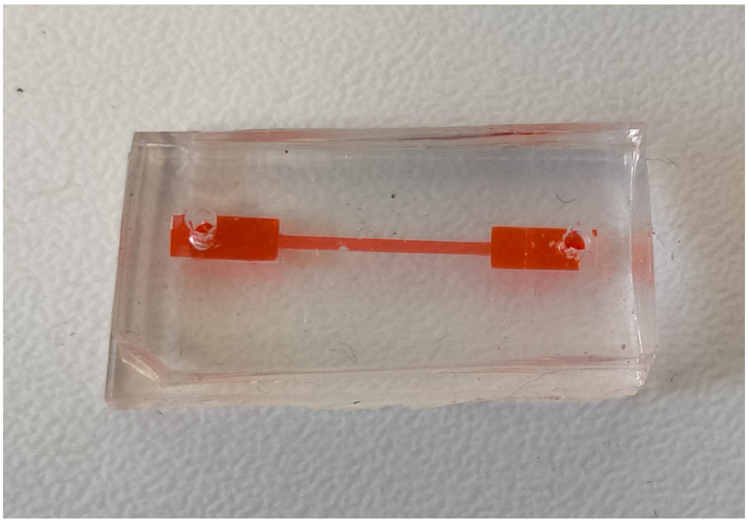

Fig. 6.1 Microfluidic device manufactured at CNR-NANOTEC in Lecce, devoted to *in-vitro* measurements of the activation of shear-responsive agglomerates.

was studied, i.e., the robustness of various classes of agglomerates was tested by verifying if a critical stress inducing breakup can be reached at any particle-particle contact.

The production process of agglomerates was investigated, and a qualitative relationship between the spray drying process conditions (mainly summarized in the Péclet number) and the morphology of the final product has been identified. Compact agglomerates are obtained in single-droplet drying simulations for fast particle diffusivity and long shrinkage time (low Péclet number). On the other hand, hollow agglomerates are the final product if the system is characterized by slow particle diffusivity and short shrinkage time (high Péclet number).

CFD simulations demonstrated the presence of a peak in hydrodynamic forces, caused by the occlusion of the blood vessel itself, that can act as an internal and non-invasive activation mechanism for the drug carriers. Micrometric agglomerates of nanoparticles have to be carefully designed in a way that let them free to circulate undisturbed in normal blood flow conditions but de-agglomerate right onto the lumen obstruction.

The behaviour of the two principal classes of agglomerates produced via spray drying flowing in a simple flow field and in an obstructed vessel was investigated as well: for both classes, maximum internal tensile stress is reached in proximity of the lumen obstruction, thus proving that the notable increase in hydrodynamic stress caused by distortion of the flow field can be effectively used as a trigger for the breakup of drug carriers; compact agglomerates are more resistant, and the distribution of the tensile stresses inside the cluster suggests the detachment of small fragments from the surface as the principal breakup mechanism; hollow agglomerates are more fragile, and the collapse of the shell structure is expected to occur after reaching the critical pull-off tension between monomers. Breakup dynamics of the proposed drug carriers has been therefore directly linked to their production process.

The principal limitation of the work up to now is the lack of an experimental validation of the simulation of the processes of agglomeration and de-agglomeration. A reliable protocol for the production of compact and hollow aggregates via spray drying has to be defined to validate the strict connection between morphology and process conditions that has been found using numerical methods. The activation process of the manufactured agglomerates should then be observed in a real microfluidic device. The proposed microchannel has been designed looking forward future in-vitro experimentations (Fig. 6.1). In this way, parameters of the proposed model can be tuned to properly match experimental evidences, and CFD-DEM simulations can in turn act as a valuable guideline for the production process: the choice of the material and the identification of the proper size and shape are the key steps for an optimal design of shear-responsive drug carriers able to correctly perform an efficient thrombolytic action. A parallel route for this investigation field is the simulation of blood flow along accurate vessel morphologies. Although it could be difficult to replicate a similar system in-vitro, such simulations would provide meaningful insights about the final scope of the drug carriers. In this case, approaches like Dissipative Particle Dynamics or Boundary Element Method would be more suitable than a CFD-SD method for the investigation of non-Newtonian fluids.

References

[1] Christopher JL Murray and Alan D Lopez. Global mortality, disability, and the contribution of risk factors: Global burden of disease study. *The Lancet*, 349(9063):1436–1442, 1997.

[2] James Grotta and John Marler. Intravenous rt-pa: a tenth anniversary reflection. *Surg. Neurol.*, 68:S12–S16, 2007.

[3] Glenn D Graham. Tissue plasminogen activator for acute ischemic stroke in clinical practice: a meta-analysis of safety data. *Stroke*, 34:2847–2850, 2003.

[4] Colin F Greineder, Melissa D Howard, Ronald Carnemolla, Douglas B Cines, and Vladimir R Muzykantov. Advanced drug delivery systems for antithrombotic agents. *Am. J. Hematol.*, 122:1565–1575, 2013.

[5] George J Shaw, Jason M Meunier, Shao-Ling Huang, Christopher J Lindsell, David D McPherson, and Christy K Holland. Ultrasound-enhanced thrombolysis with tpa-loaded echogenic liposomes. *Thromb. Res.*, 124:306–310, 2009.

[6] Jiangnan Hu, Shengwei Huang, Lu Zhu, Weijie Huang, Yiping Zhao, Kunlin Jin, and Qichuan ZhuGe. Tissue plasminogen activator-porous magnetic microrods for targeted thrombolytic therapy after ischemic stroke. *ACS Appl. Mater. Interfaces*, 10:32988–32997, 2018.

[7] Rui Cheng, Weijie Huang, Lijie Huang, Bo Yang, Leidong Mao, Kunlin Jin, Qichuan ZhuGe, and Yiping Zhao. Acceleration of tissue plasminogen activator-mediated thrombolysis by magnetically powered nanomotors. *ACS Nano*, 8:7746–7754, 2014.

[8] Siyu Wang, Xixi Guo, Weijun Xiu, Yang Liu, Lili Ren, Huaxin Xiao, Fang Yang, Yu Gao, Chenjie Xu, and Lianhui Wang. Accelerating thrombolysis using a precision and clot-penetrating drug delivery strategy by nanoparticle-shelled microbubbles. *Sci. Adv.*, 6:eaaz8204, 2020.

[9] Michael D Kaminski, Yumei Xie, Carol J Mertz, Martha R Finck, Haitao Chen, and Axel J Rosengart. Encapsulation and release of plasminogen activator from biodegradable magnetic microcarriers. *Eur. J. Pharm. Sci.*, 35:96–103, 2008.

[10] Emily Mihalko, Ke Huang, Erin Sproul, Ke Cheng, and Ashley C Brown. Targeted treatment of ischemic and fibrotic complications of myocardial infarction using a dual-delivery microgel therapeutic. *ACS Nano*, 12:7826–7837, 2018.

[11] Netanel Korin, Mathumai Kanapathipillai, Benjamin D Matthews, Marilena Crescente, Alexander Brill, Tadanori Mammoto, Kaustabh Ghosh, Samuel Jurek, Sidi A Bencherif, Deen Bhatta, et al. Shear-activated nanotherapeutics for drug targeting to obstructed blood vessels. *Science*, 337:738–742, 2012.

[12] Miroslav Soos, Lyonel Ehrl, Matthäus U Bäbler, and Massimo Morbidelli. Aggregate breakup in a contracting nozzle. *Langmuir*, 26:10–18, 2010.

[13] Debashish Saha, Miroslav Soos, Beat Lüthi, Markus Holzner, Alex Liberzon, Matthäus U Bäbler, and Wolfgang Kinzelbach. Experimental characterization of breakage rate of colloidal aggregates in axisymmetric extensional flow. *Langmuir*, 30:14385–14395, 2014.

[14] Romana Perinajová, Joe F Juffermans, Jos JM Westenberg, Roel LF van der Palen, Pieter J van den Boogaard, Hildo J Lamb, and Saša Kenjereš. Geometrically induced wall shear stress variability in cfd-mri coupled simulations of blood flow in the thoracic aortas. *Comput. Biol. Med.*, 133:104385, 2021.

[15] Yunduo Charles Zhao, Parham Vatankhah, Tiffany Goh, Rhys Michelis, Kiarash Kyanian, Yingqi Zhang, Zhiyong Li, and Lining Arnold Ju. Hemodynamic analysis for stenosis microfluidic model of thrombosis with refined computational fluid dynamics simulation. *Sci. Rep.*, 11:1–10, 2021.

[16] Guillaume Troianowski, Charles A Taylor, Jeffrey A Feinstein, and Irene E Vignon-Clementel. Three-dimensional simulations in glenn patients: clinically based boundary conditions, hemodynamic results and sensitivity to input data. *J. Biomech. Eng.*, 133:111006, 2011.

[17] Gregory Arbia, Chiara Corsini, Mahdi Esmaily Moghadam, Alison L. Marsden, Francesco Migliavacca, Giancarlo Pennati, Tain-Yen Hsia, and Irene E. Vignon-Clementel. Numerical blood flow simulation in surgical corrections: what do we need for an accurate analysis? *J. Surg. Res.*, 186:44–55, 2014.

[18] Chiara Corsini, Catriona Baker, Ethan Kung, Silvia Schievano, Gregory Arbia, Alessia Baretta, Giovanni Biglino, Francesco Migliavacca, Gabriele Dubini, Giancarlo Pennati, et al. An integrated approach to patient-specific predictive modeling for single ventricle heart palliation. *Comput. Methods Biomech. Biomed. Engin.*, 17:1572–1589, 2014.

[19] Lorenzo Vasquez Giuliano, Antonio Buffo, Marco Vanni, Alessandra Sabina Lanotte, Valentina Arima, Monica Bianco, Francesca Baldassarre, and Graziano Frungieri. Response of shear-activated nanotherapeutic particles in a clot-obstructed blood vessel by cfd-dem simulations. *The Canadian Journal of Chemical Engineering*, 100(12):3562–3574, 2022.

[20] Lorenzo Vasquez Giuliano, Antonio Buffo, Marco Vanni, and Graziano Frungieri. Micromechanics and strength of agglomerates produced by spray drying. *JCIS Open*, 9:100068, 2023.

[21] Jeffery S Marshall and Shuiqing Li. *Adhesive particle flow*. Cambridge University Press, 2014.

[22] Heinrich Hertz. Ueber die berührung fester elastischer körper. 1882.

[23] SP Timoshenko and JN Goodier. *Theory of Elasticity 3rd ed., 567*. McGraw-Hill, New York, 1970.

[24] Shuiqing Li, Jeffrey S Marshall, Guanqing Liu, and Qiang Yao. Adhesive particulate flow: The discrete-element method and its application in energy and environmental engineering. *Progress in Energy and Combustion Science*, 37(6):633–668, 2011.

[25] Boris V Derjaguin, Vladimir M Muller, and Yu P Toporov. Effect of contact deformations on the adhesion of particles. *Journal of Colloid and interface science*, 53(2):314–326, 1975.

[26] Kenneth Langstreth Johnson, Kevin Kendall, and A.D. Roberts. Surface energy and the contact of elastic solids. *P. Roy. Soc. A-Math. Phy.*, 324:301–313, 1971.

[27] Daniel Maugis. Adhesion of spheres: the jkr-dmt transition using a dugdale model. *Journal of colloid and interface science*, 150(1):243–269, 1992.

[28] Arati Chokshi, AGGM Tielens, and D Hollenbach. Dust coagulation. *The Astrophysical Journal*, 407:806–819, 1993.

[29] Peter A Cundall and Otto DL Strack. A discrete numerical model for granular assemblies. *Geotechnique*, 29:47–65, 1979.

[30] Raymond David Mindlin. Compliance of elastic bodies in contact. 1949.

[31] Kenneth Langstreth Johnson. *Contact mechanics*. Cambridge university press, 1987.

[32] Kazuyoshi Iwashita and Masanobu Oda. Rolling resistance at contacts in simulation of shear band development by dem. *Journal of engineering mechanics*, 124(3):285–292, 1998.

[33] C Thornton. Interparticle sliding in the presence of adhesion. *Journal of Physics D: Applied Physics*, 24(11):1942, 1991.

[34] Colin Thornton and KK Yin. Impact of elastic spheres with and without adhesion. *Powder technology*, 65(1-3):153–166, 1991.

[35] C Dominik and AGGM Tielens. Resistance to rolling in the adhesive contact of two elastic spheres. *Philosophical Magazine A*, 72(3):783–803, 1995.

[36] V. Šmilauer, E. Catalano, B. Chareyre, S. Dorofeenko, J. Duriez, A. Gladky, J. Kozicki, C. Modenese, L. Scholtès, L. Sibille, et al. *Yade Documentation 3rd ed.* The Yade Project, 2015.

[37] Barthelemy Harthong, Jean-Francois Jerier, Vincent Richefeu, Bruno Chareyre, Pierre Dorémus, Didier Imbault, and Frédéric-Victor Donzé. Contact impingement in packings of elastic–plastic spheres, application to powder compaction. *International Journal of Mechanical Sciences*, 61:32–43, 2012.

[38] Rodaina Aboul Hosn, Luc Sibille, Nadia Benahmed, and Bruno Chareyre. Discrete numerical modeling of loose soil with spherical particles and interparticle rolling friction. *Granular Matter*, 19:1–12, 2017.

[39] K L Johnson, K Kendall, and A D Roberts. Surface energy and the contact of elastic solids. *Proceedings of the Royal Society of London. A. Mathematical and Physical Sciences*, 324:301–313, 1971.

[40] M L Eggersdorfer, D. Kadau, H J Herrmann, and S E Pratsinis. Fragmentation and restructuring of soft agglomerates under shear. *Journal of Colloid and Interface Science*, 342:261–268, 2010.

[41] M. Kroupa, M. Vonka, and J. Kosek. Modeling the mechanism of coagulum formation in dispersions. *Langmuir*, 30:2693 – 2702, 2014.

[42] J.F. Wilson, M. Kroupa, J. Kosek, and M. Soos. Numerical study of soft colloidal nanoparticles interaction in shear flow. *Langmuir*, 34:15600 – 15611, 2018.

[43] X. Ruan, S. Chen, and S. Li. Structural evolution and breakage of dense agglomerates in shear flow and Taylor-Green vortex. *Chemical Engineering Science*, 211:115261, 2020.

[44] P S Grassia, E J Hinch, and L C Nitsdche. Computer simulations of brownian motion of complex systems. *Journal of Fluid Mechanics*, 282:373 – 403, 1995.

[45] Akash Saxena, Jean-Sébastien Kroll-Rabotin, and R Sean Sanders. Numerical investigation of the respective roles of cohesive and hydrodynamic forces in aggregate restructuring under shear flow. *Journal of Colloid and Interface Science*, 608:355–365, 2022.

[46] Yogesh M Harshe and Marco Lattuada. Universal breakup of colloidal clusters in simple shear flow. *The Journal of Physical Chemistry B*, 120:7244–7252, 2016.

[47] Graziano Frungieri and Marco Vanni. Aggregation and breakup of colloidal particle aggregates in shear flow: A combined Monte Carlo - Stokesian dynamics approach. *Powder Technology*, 388:357 – 370, 2021.

[48] Volker Becker, Eva Schlauch, Marek Behr, and Heiko Briesen. Restructuring of colloidal aggregates in shear flows and limitations of the free-draining approximation. *Journal of Colloid and Interface Science*, 339(2):362–372, 2009.

[49] Lorenzo Turetta and Marco Lattuada. The role of hydrodynamic interactions on the aggregation kinetics of sedimenting colloidal particles. *Soft Matter*, 18(8):1715–1730, 2022.

[50] Graziano Frungieri, Matthaus U. Bäbler, and Marco Vanni. Shear-induced heteroaggregation of oppositely charged colloidal particles. *Langmuir*, 36:10739 – 10749, 2020.

[51] Marco Vanni and Andrea Gastaldi. Hydrodynamic forces and critical stresses in low-density aggregates under shear flow. *Langmuir*, 27:12822–12833, 2011.

[52] Marco Vanni. Accurate modelling of flow induced stresses in rigid colloidal aggregates. *Computer Physics Communications*, 192:70–90, 2015.

[53] Z. Ren, Y M Harshe, and M. Lattuada. Influence of the potential well on the breakage rate of colloidal aggregates in simple shear and uniaxial extensional flows. *Langmuir*, 31:5712–5721, 2015.

[54] Graziano Frungieri. *A novel Monte Carlo-Discrete Element Method approach for the micro-mechanics of colloidal suspensions*. PhD thesis, Ph. D. thesis, Politecnico di Torino, 2018.

[55] S Kim and SJ Karrila. Microhydrodynamics: Principles and selected applications, 2005.

[56] Louis Durlofsky, John F Brady, and Georges Bossis. Dynamic simulation of hydrodynamically interacting particles. *Journal of Fluid Mechanics*, 180:21–49, 1987.

[57] John F Brady, Ronald J Phillips, Julia C Lester, and Georges Bossis. Dynamic simulation of hydrodynamically interacting suspensions. *Journal of Fluid Mechanics*, 195:257–280, 1988.

[58] Elisabeth Guazzelli and Jeffrey F Morris. *A physical introduction to suspension dynamics*. Cambridge University Press, 2011.

[59] Sangtae Kim and Seppo J Karrila. *Microhydrodynamics: principles and selected applications*. Butterworth-Heinemann, 1991.

[60] J.S. Marshall. Discrete-element modeling of particulate aerosol flows. *Journal of Computational Physics*, 228:1541–1561, 2009.

[61] C. Dominik and A G G M Tielens. The physics of dust coagulation and the structure of dust aggregates in space. *The Astrophysical Journal*, 480:647 – 673, 1997.

[62] Katalin Bagi and Matthew R Kuhn. A definition of particle rolling in a granular assembly in terms of particle translations and rotations. *Journal of Applied Mechanics*, 71:493–501, 2004.

[63] J. De Bona, A S Lanotte, and M. Vanni. Internal stresses and breakup of rigid isostatic aggregates in homogeneous and isotropic turbulence. *Journal of Fluid Mechanics*, 755:365 – 396, 2014.

[64] Graziano Frungieri, Gianluca Boccardo, Antonio Buffo, Daniele Marchisio, Hossein Ali Karimi-Varzaneh, and Marco Vanni. A CFD-DEM approach to study the breakup of fractal agglomerates in an internal mixer. *The Canadian Journal of Chemical Engineering*, 98:1880–1892, 2020.

[65] Graziano Frungieri, Gianluca Boccardo, Antonio Buffo, Hossein Ali Karimi-Varzaneh, and Marco Vanni. CFD-DEM characterization and population balance modelling of a dispersive mixing process. *Chemical Engineering Science*, 260:117859, 2022.

[66] Joel H Ferziger, Milovan Perić, and Robert L Street. *Computational methods for fluid dynamics*, volume 3. Springer, 2002.

[67] Ronald L Fournier. *Basic transport phenomena in biomedical engineering*. Taylor & Francis, Philadelphia, PA,, 2017.

[68] Dmitry A Fedosov, Hiroshi Noguchi, and Gerhard Gompper. Multiscale modeling of blood flow: from single cells to blood rheology. *Biomech. Model. Mechanobiol.*, 13:239–258, 2014.

[69] Fuat Yilmaz and Mehmet Yasar Gundogdu. A critical review on blood flow in large arteries; relevance to blood rheology, viscosity models, and physiologic conditions. *Korea Aust. Rheol. J.*, 20:197–211, 2008.

[70] Amirhossein Arzani. Accounting for residence-time in blood rheology models: do we really need non-newtonian blood flow modelling in large arteries? *J. R. Soc. Interface*, 15:20180486, 2018.

[71] Lorenzo Vasquez Giuliano, Marco Vanni, Antonio Buffo, and Graziano Frungieri. Sviluppo di farmaci innovativi per la rimozione di ostruzioni arteriose: modellazione fluidodinamica del processo di attivazione. Master's thesis, 2019.

[72] ANSYS Fluent. Ansys fluent theory guide 15.0. *ANSYS, Canonsburg, PA*, 33, 2013.

[73] CT Crowe, Martin Sommerfeld, and Yutaka Tsuji. Multiphase flows with particles and droplets, 1998.

[74] Dan-Lei Yang, Qian Sun, Yong-Hong Duan, Hao Niu, Rui-Li Wang, Dan Wang, Mei-Fang Zhu, and Jie-Xin Wang. Efficient construction of SiO_2 colloidal nanoparticle clusters as novel fillers by a spray-drying process for

dental composites. *Industrial & Engineering Chemistry Research*, 58:18178–18186, 2019.

[75] Archana Mishra, Vipul K Pandey, Bhavani S Shankar, and Jose S Melo. Spray drying as an efficient route for synthesis of silica nanoparticles-sodium alginate biohybrid drug carrier of doxorubicin. *Colloids and Surfaces B: Biointerfaces*, 197:111445, 2021.

[76] Maria-Inês Rè. Formulating drug delivery systems by spray drying. *Drying Technology*, 24:433–446, 2006.

[77] Lucas Ruffel, Jérémy Soulié, Yannick Coppel, Pierre Roblin, Fabien Brouillet, Christine Frances, and Mallorie Tourbin. Ibuprofen loading into mesoporous silica nanoparticles using co-spray drying: A multi-scale study. *Microporous and Mesoporous Materials*, 291:109689, 2020.

[78] Nicolas Tsapis, David Bennett, Blair Jackson, David A Weitz, and D A Edwards. Trojan particles: large porous carriers of nanoparticles for drug delivery. *Proceedings of the National Academy of Sciences*, 99:12001–12005, 2002.

[79] P Roy, G Bertrand, and C Coddet. Spray drying and sintering of zirconia based hollow powders. *Powder Technology*, 157:20–26, 2005.

[80] G. Bertrand, P. Roy, C. Filiatre, and C. Coddet. Spray-dried ceramic powders: A quantitative correlation between slurry characteristics and shapes of the granules. *Chemical Engineering Science*, 60:95–102, 2005.

[81] Rui Zhang, Qingke Tan, Shouchun Bao, Jianbin Deng, Yan Xie, Fei Zheng, Guanglei Wu, and Binghui Xu. Spray drying induced engineering a hierarchical reduced graphene oxide supported heterogeneous tin dioxide and zinc oxide for lithium-ion storage. *Journal of Colloid and Interface Science*, 608:1758–1768, 2022.

[82] Gaoyang Liu, Zehong Wang, Bingwei Bao, Zhijun Ouyang, Chunxiao Du, Fen Liu, Wei Wang, and Dan Yu. Construction of sustainable and multifunctional polyester fabrics via an efficiently and eco-friendly spray-drying layer-by-layer strategy. *Journal of Colloid and Interface Science*, 588:50–61, 2021.

[83] Iris Schmitz-Schug, Ulrich Kulozik, and Petra Foerst. Modeling spray drying of dairy products–impact of drying kinetics, reaction kinetics and spray drying conditions on lysine loss. *Chemical Engineering Science*, 141:315–329, 2016.

[84] Asep Bayu Dani Nandiyanto and Kikuo Okuyama. Progress in developing spray-drying methods for the production of controlled morphology particles: From the nanometer to submicrometer size ranges. *Advanced Powder Technology*, 22:1–19, 2011.

[85] A. Stunda-Zujeva, Z. Irbe, and L. Berzina-Cimdina. Controlling the morphology of ceramic and composite powders obtained via spray drying – a review. *Ceramics International*, 43:11543–11551, 2017.

[86] Ranajt Mondal, Avik Das, Debasis Sen, Dillip K Satapathy, and Madivala G Basavaraj. Spray drying of colloidal dispersions containing ellipsoids. *Journal of colloid and interface science*, 551:242–250, 2019.

[87] Rosa Mondragon, Leonor Hernandez, J Enrique Julia, Juan Carlos Jarque, Sergio Chiva, Belal Zaitone, and Cameron Tropea. Study of the drying behavior of high load multiphase droplets in an acoustic levitator at high temperature conditions. *Chemical Engineering Science*, 66:2734–2744, 2011.

[88] Abdulkadir Osman, Lucas Goehring, Alessandro Patti, Hugh Stitt, and Nima Shokri. Fundamental investigation of the drying of solid suspensions. *Industrial & Engineering Chemistry Research*, 56:10506–10513, 2017.

[89] Jui Chen Lin and James W Gentry. Spray drying drop morphology: experimental study. *Aerosol Science & Technology*, 37:15–32, 2003.

[90] Eline Boel, Robin Koekoekx, Sien Dedroog, Iurii Babkin, Maria Rosaria Vetrano, Christian Clasen, and Guy Van den Mooter. Unraveling particle formation: from single droplet drying to spray drying and electrospraying. *Pharmaceutics*, 12:625, 2020.

[91] E Lintingre, F Lequeux, Laurence Talini, and N Tsapis. Control of particle morphology in the spray drying of colloidal suspensions. *Soft Matter*, 12:7435–7444, 2016.

[92] Christopher S Handscomb, Markus Kraft, and A E Bayly. A new model for the drying of droplets containing suspended solids after shell formation. *Chemical Engineering Science*, 64:228–246, 2009.

[93] Christopher S Handscomb and Markus Kraft. Simulating the structural evolution of droplets following shell formation. *Chemical Engineering Science*, 65:713–725, 2010.

[94] Hassan Abdullahi, Christopher L Burcham, and Thomas Vetter. A mechanistic model to predict droplet drying history and particle shell formation in multicomponent systems. *Chemical Engineering Science*, 224:115713, 2020.

[95] Moritz Buchholz, Johannes Haus, Swantje Pietsch-Braune, Frank Kleine Jäger, and Stefan Heinrich. Cfd-aided population balance modeling of a spray drying process. *Advanced Powder Technology*, 33(7):103636, 2022.

[96] Thomas Breinlinger, Adham Hashibon, and Torsten Kraft. Simulation of the influence of surface tension on granule morphology during spray drying using a simple capillary force model. *Powder Technology*, 283:1–8, 2015.

[97] Shigeto Miyazaki, Daisuke Nishiura, Atsuko Shimosaka, Yoshiyuki Shirakawa, and Jusuke Hidaka. Revealing the formation mechanism of granules by drying simulation of slurry droplet. *Advanced Powder Technology*, 22:93–101, 2011.

[98] Katarzyna Jabłczyńska, Jakub M Gac, and Tomasz R Sosnowski. Self-organization of colloidal particles during drying of a droplet: Modeling and experimental study. *Advanced Powder Technology*, 29:3542–3551, 2018.

[99] Sabrina Zellmer, Georg Garnweitner, Thomas Breinlinger, Torsten Kraft, and Carsten Schilde. Hierarchical structure formation of nanoparticulate spray-dried composite aggregates. *ACS Nano*, 9:10749–10757, 2015.

[100] AL Yarin, Günter Brenn, O Kastner, and C Tropea. Drying of acoustically levitated droplets of liquid–solid suspensions: Evaporation and crust formation. *Physics of Fluids*, 14:2289–2298, 2002.

[101] J. Cranck. *The mathematics of diffusion*. Clarendon Press, 1979.

[102] Monica Skoge, Aleksandar Donev, Frank H Stillinger, and Salvatore Torquato. Packing hyperspheres in high-dimensional euclidean spaces. *Phys. Rev. E*, 74:041127, 2006.

[103] Léa Guérin, Carole Coufort-Saudejaud, Alain Liné, and Christine Frances. Dynamics of aggregate size and shape properties under sequenced flocculation in a turbulent taylor-couette reactor. *Journal of colloid and interface science*, 491:167–178, 2017.

[104] Graziano Frungieri and Marco Vanni. Aggregation and breakup of colloidal particle aggregates in shear flow: A combined monte carlo-stokesian dynamics approach. *Powder Technol.*, 388:357–370, 2021.

[105] Graziano Frungieri and Marco Vanni. Shear-induced aggregation of colloidal particles: A comparison between two different approaches to the modelling of colloidal interactions. *The Canadian Journal of Chemical Engineering*, 95(9):1768–1780, 2017.

[106] Y.M. Harshe, L. Ehrl, and M. Lattuada. Hydrodynamic properties of rigid fractal aggregates of arbitrary morphology. *Journal of Colloid and Interface Science*, 352:87 – 98, 2010.

[107] L. Sanchez Fellay, C. Twist, and M. Vanni. Motion of rigid aggregates under different flow conditions. *Acta Mechanica*, 224:2225 – 2248, 2013.

[108] Abdul SM Khader, Satish B Shenoy, Raghuvir B Pai, Ganesh S Kamath, Nabeel Md Sharif, and VRK Rao. Effect of increased severity in patient specific stenosis of common carotid artery using cfd—a case study. *World J. Model. Simul.*, 7:113–122, 2011.

[109] Yue Zhou, Chunhian Lee, and Jingying Wang. The computational fluid dynamics analyses on hemodynamic characteristics in stenosed arterial models. *J. Healthc. Eng.*, 2018:4312415, 2018.

[110] Q Long, XY Xu, KV Ramnarine, and P Hoskins. Numerical investigation of physiologically realistic pulsatile flow through arterial stenosis. *J. Biomech.*, 34:1229–1242, 2001.

[111] Giulio Lorenzini and Erminio Casalena. Cfd analysis of pulsatile blood flow in an atherosclerotic human artery with eccentric plaques. *J. Biomech.*, 41:1862–1870, 2008.

[112] David N Ku. Blood flow in arteries. *Annual review of fluid mechanics*, 29(1):399–434, 1997.

[113] M Klarhöfer, B Csapo, Cs Balassy, JC Szeles, and E Moser. High-resolution blood flow velocity measurements in the human finger. *Magnetic Resonance in Medicine: An Official Journal of the International Society for Magnetic Resonance in Medicine*, 45(4):716–719, 2001.

Appendix A

Yade code for single droplet spay drying

```
### DESCRIPTION ###
# Spray drying process of a droplet with radius 'R', containing a dispersion of 'np' particles of mean radius 'a'
# Radius distribution can be uniform between aMin=a*(1-fuzz) and aMax=a*(1+fuzz) [BimodalBool=False]
# or bimodal with spheres of radius aMin and aMax [BimodalBool=True]
# Phases in the script:
# - From t=0 to t=tauCrust : drying phase at constant temperature (Twetbulb);
# - From t=tauCrust to t=tau : drying phase with linearly increasing temperature from Twetbulb to Tboil;
# - From t=tau to t=tau*(1+expFrac): thermal expansion phase (optional)
# Particles are cohesive. The bond strength is related to their superficial energy 'sigma'
# If [EnableBrownian=True], brownian motion is taken into account
# Timestep can be modified by 'iterPeriod' and 'TimeStepFrac'
##################

### INPUT ###
# Input data expressed in so-called DEM program units (see conversions below), can also be converted
# in SI units at the beginning and reconverted in DEM units for the final output.
```

```
#############

### OUTPUT ###
# - geometry file describing position of nanoparticles at intermediate adimensional times 'theta'
# - geometry file of the aggregate at the end of  drying   phase "FinalGeometry_tau.geo" ;
# - geometry file of the aggregate at the end of therm. exp. phase "FinalGeometry_tauExp.geo" ;
# - File with the variation of R and T over time "droplet.dat" [EnableVTK=True];
# - VTK files for postprocess in paraView [EnableVTK=True]
##############

### POSTPROCESS ###
# use the yade script 'finalAggregate.py' on the final geometry, using the following command line:
# $ yade finalAggregate.py FinalGeometry_***.geo
#
# The python script 'post.py' compares final geometries in terms of hc, dc, relative position of monomers inside the agglomerate
###################

### BATCH MODE ###
# This script can be run in batch mode, i.e. various jobs with variation of parameters as defined in file 'params.txt'
# For  batch mode  , use command line: $ yade-batch params.txt script.py
# For non-batch mode, use command line: $ yade script.py
#
# - Parallelization
#   If all jobs shall use the same number of threads, '--job-threads=2' means that each job will get 2 threads.
#   The number of jobs that run simultaneously is defined by the total number of threads that you allow by -j option.
#   This parameters do not affect the total number of jobs/simulations that can be set up in the parameters table,
#   if the cores are not enough some simulations will begin as soon as the others come to an end.
#
#   '-j**' defines total number of threads (example: -j10 establishes that 10 threads will be used during batch simulation)
```

```python
#   '--job-threads=**' defines threads per job (example: --job-threads=2 establishes that 2 threads per job will be used)
#
#   add 'nohup' at the beginning and '&' at the end for remote background execution:
#   $ nohup yade-batch -jN --job-threads=n params.txt script.py &
###################



# DEM units
L = 1e-7       #[m]
M = 1e-6       #[kg]
T = 1.0        #[s]
F = L*M/(T**2) #[N]
P = F/(L**2)   #[N/m^2]
# Packages required
import math
import random
from yade import pack



# ---- INPUT ---- #

# Run automatically
runAuto = True # Set to 'False' for non-batch execution and debug
# Initial geometry
BimodalBool = False # if 'False', radii of the monomers follows a uniform distribution.
# Enabling thermal expansion phase
EnableThermExp = False

# Variables imported from table. A std. value for non-batch mode is defined
readParamsFromTable(
  np = 100, # Initial number of particles
  a = 5.0, # Mean monomer radius in DEM unit
  fuzz = 0.0, # Relative fuzz (dispersion) of radius 'a'
  R0 = 100.,# Initial droplet radius in DEM unit
  tau = 5.0e-3,#[s] # Drying time
  tauCrust = 1.0e-3,#[s] # Time at wich crust is supposed to be formed (it has to be true that tauCrust<tau)
```

```
  ExpFrac = 0.1, # tau*ExpFrac is 'tauExp', time for the thermal
    expansion phase
  iterPeriod = 1, # Principal functions are called after '
    iterPeriod' steps
  TimeStepFrac = 1., # O.dt=PWaveTimestep*TimeStepFrac
  sigma = 0.073e-3,#[N/m]# Water Surface tension
  etaRoll = 1.8, # Dimensionless rolling strength.
  Twetbulb = 100,#[C] # Wet bulb temperature of the droplet in
    Celsius
  Tboil = 100,#[C] # Boiling  temperature of the droplet in
    Celsius
  EnableBrownian = True, # if 'True', the brownian motion is taken
     into account
  omega = 1.0, # Cn proportional to Fadh*omega
  )
# make all table variables accessible directly as variables later
from yade.params.table import *

a  =  a*L #[m] # Mean monomer radius
R0 = R0*L #[m] # Initial droplet radius

aMax = a + a*fuzz # max monomer radius
aMin = a - a*fuzz # min monomer radius

tauExp = tau*ExpFrac # Time for thermal expansion

# Properties of the material
rho = 1300  #[kg/m^3] # PLGA Density
E   = 3.4e9 #[Pa] # PLGA Young modulus
nu  = 0.5 # PLGA Poisson coefficient
eps = 10.0e-3 #[N/m] # PLGA surface energy

# Gravity
g_x = 0.
g_y = 0. #-9.81
g_z = 0.

# Other parameters
hamak  = 0.966e-20 # Hamaker constant
z0dist = 0.165e-9 #[m] # distance z0
r_int  = 1.0 # interaction radius needed for cohesion (1.0 => no
    interaction until contact)

```

```
# Properties of the fluid. Hp: no interaction between particles before contact, stagnant fluid
rho_l = 1000 #[kg/m^3] # water density
eta_l = 1e-3 #[Pa s]   # water viscosity
u_lx  = 0.0  #[m/s]  # water velocity along x
u_ly  = 0.0  #[m/s]  # water velocity along y
u_lz  = 0.0  #[m/s]  # water velocity along z
w_lx  = 0.0  #[rad/s]  # water ang.vel. along x
w_ly  = 0.0  #[rad/s]  # water ang.vel. along y
w_lz  = 0.0  #[rad/s]  # water ang.vel. along z
Kb  = 1.38064852e-23 #[m^2*kg/s^2/K] # Boltzmann's constant

# VTK for postprocessing
EnableVTK = True # if 'True', files for postprocess in ParaView are produced
frames     = 250  # number of desired frames

# Three adimensional times at wich geometry has to be printed (theta=0. beginning of the shrinkage, tau=1. end)
theta_0  = 0.0
theta_1  = 0.2
theta_2  = 0.4
# --- #


# Path for simulations
# Create a folder for each simulation.
# use O.tags['d.id'] to distinguish individual runs of the same simulation
title   = O.tags['d.id']
folder  = os.path.dirname(sys.argv[0])+str(title)+"/"
if os.path.exists(folder)==False:
  os.mkdir(folder)



### SETTING UP THE SIMULATION
print("\n")

### Adhesive force and cohesion factors Cn/Cs
# Use the general JKR model. Select the most suitable approximation based on the value of 'fuzz'
if fuzz<0.5: # calculate Cn using aMin=a*(1-fuzz)
```

```
    Fadh = 3/2*math.pi*eps*aMin # Adhesive force
    Cn   = Fadh/(aMin**2)*omega # Normal cohesion factor
    Cs   = Cn/omega         # Shear  cohesion factor
    print("Adhesion force  from JKR using aMin : Fadh = %5.3e N" %Fadh )
    print("Cohesion factor from JKR using aMin : Cn   = %5.3e N/m^2" %Cn   )
    print("\t\t\tCs   = %5.3e N/m^2" %Cs   )
else: # calculate Cn using aMean=a
    Fadh = 3/2*math.pi*eps*a  # Adhesive force
    Cn   = Fadh/(a**2)*omega  # Normal cohesion factor
    Cs   = Cn/omega         # Shear  cohesion factor
    print("Adhesion force  from JKR using aMean: Fadh = %5.3e N" %Fadh )
    print("Cohesion factor from JKR using aMean: Cn   = %5.3e N/m^2" %Cn   )
    print("\t\t\tCs   = %5.3e N/m^2" %Cs   )

# Define cohesive material and append it to the simulation
sampleMat=CohFrictMat(
 young=E,
 poisson=nu,
 frictionAngle=radians(17),
 isCohesive=True,
 alphaKr=1.8, # Dimensionless rolling stiffness
 alphaKtw=0, # Dimensionless  twist  stiffness
 etaRoll=etaRoll,   # Dimensionless rolling strength
 normalCohesion=Cn, # Kn - Tensile strength, homogeneous to a pressure
 shearCohesion=Cs,  # Ks -  Shear  strength, homogeneous to a pressure
 momentRotationLaw=True,
 density=rho,
 label='PLGA',
)
O.materials.append(sampleMat)


### Initial geometry
# Generate a bimodal distribution of np monomers in a droplet with radius R0.
def BimodalDistribution(np,a1,a2,R0):

```

```python
# Create arrays containing x,y,z coordinates and radius of every particle
xArray=numpy.array([])
yArray=numpy.array([])
zArray=numpy.array([])
radiusArray=numpy.array([])
materialArray=numpy.array([])
VolumeRatio=int( max(a1,a2)**3/min(a1,a2)**3 )
for ii in range(np): # For every particle that needs to be added:

  # Alternate the two radii according to volume ratio
  if ii%(VolumeRatio+1)==0:
    radius=max(a1,a2) ; material='PLGA_BimodMax'
  else:
    radius=min(a1,a2) ; material='PLGA_BimodMin'


  # Generate x,y,z and radius of the first particle
  x = random.random()*2*R0 - R0
  y = random.random()*2*R0 - R0
  z = random.random()*2*R0 - R0
  itercounter=0
  while math.sqrt(x**2+y**2+z**2)>(R0-max(a1,a2)):
    x = random.random()*2*R0 - R0
    y = random.random()*2*R0 - R0
    z = random.random()*2*R0 - R0
    itercounter=itercounter+1
    if itercounter > 1000:
      print("ERROR")
      exit()

  # Generate x,y,z and radius of the other particles, with the condition of no-overlapping
  for jj in range(len(xArray)):
    itercounter=0
    while math.sqrt((x-xArray[jj])**2+(y-yArray[jj])**2+(z-zArray[jj])**2)<(radius+radiusArray[jj]) \
    or math.sqrt(x**2+y**2+z**2)>(R0-max(a1,a2)):
      x = random.random()*2*R0 - R0
      y = random.random()*2*R0 - R0
      z = random.random()*2*R0 - R0
      itercounter=itercounter+1
```

```
        if itercounter > 1000:
          print("ERROR")
          exit()

    xArray = numpy.append(xArray,x)
    yArray = numpy.append(yArray,y)
    zArray = numpy.append(zArray,z)
    radiusArray = numpy.append(radiusArray,radius)
    materialArray = numpy.append(materialArray,material)
  return xArray,yArray,zArray,radiusArray, materialArray

if BimodalBool:
  ### Define two materials with different Cn for the two classes of monomers:
  ## - radius aMin
  Fadh_BimodMin=3/2*math.pi*eps*aMin ; Cn_BimodMin=Fadh_BimodMin/(aMin**2) ; Cs_BimodMin=Cn_BimodMin
  sampleMat_BimodMin=CohFrictMat(
   young=E,
   poisson=nu,
   frictionAngle=radians(17),
   isCohesive=True,
   alphaKr=1.8,
   alphaKtw=0,
   etaRoll=etaRoll,
   normalCohesion=Cn_BimodMin,
   shearCohesion=Cs_BimodMin,
   momentRotationLaw=True,
   density=rho,
   label='PLGA_BimodMin',)
  O.materials.append(sampleMat_BimodMin)
  ## - radius aMax (BimodMax)
  Fadh_BimodMax=3/2*math.pi*eps*aMax ; Cn_BimodMax=Fadh_BimodMax/(aMax**2) ; Cs_BimodMax=Cn_BimodMax
  sampleMat_BimodMax=CohFrictMat(
   young=E,
   poisson=nu,
   frictionAngle=radians(17),
   isCohesive=True,
   alphaKr=1.8,
   alphaKtw=0,
   etaRoll=etaRoll,
   normalCohesion=Cn_BimodMax,
```

```
      shearCohesion=Cs_BimodMax,
      momentRotationLaw=True,
      density=rho,
      label='PLGA_BimodMax',)
    O.materials.append(sampleMat_BimodMax)
    # Generate a population of monomers with BIMODAL radius distribution
    xBimod,yBimod,zBimod,radiusBimod,materialBimod=BimodalDistribution(np,aMin,aMax,R0)
    # Add monomers to the simulation
    for ii in range(np):
        O.bodies.append(sphere(
            center=(xBimod[ii],yBimod[ii],zBimod[ii]),
            radius=radiusBimod[ii],
            material=materialBimod[ii],
            ))
else:
    # Generate a population of monomers with uniform radius distribution
    # Cloud of pcles in a defined box, add to the simulation only the ones enclosed in the droplet
    sp=pack.SpherePack()
    sp.makeCloud(
        # corners of the box that encloses a sphere with radius R0
        minCorner=(-R0,-R0,-R0),
        maxCorner=(+R0,+R0,+R0),
        num=2*np,
        rMean=a, # mean radius of pcles
        rRelFuzz=fuzz, # spheres will have radii rMean +- (rMean*rRelFuzz)
        )
    # Predicate that defines the droplet at the beginning of the simulation
    pred = pack.inSphere(center=(0,0,0),radius=R0)
    for c,r in sp:
        if pred(c,r): # if a sphere with center 'c' and radius 'r' is inside predicate, append it to the simulation
            O.bodies.append(sphere(center=c,radius=r,material='PLGA'))
    # then, update the value of np with the effective number of particles in the droplet
    np = len(O.bodies)


```

```
# Quadratic law for shrinkage : R(t)**2 = R0**2 - k*t. Calculate k from condition R(tau)=0.0
k = R0**2 / tau

# Quadratic law for therm.exp.: R(t)**2 = kExp*t. Calculate kExp from condition R(tauExp)=R0
kExp = R0**2 / tauExp

# Inizialization of the temperature and conversion in Kelvin
 Twetbulb     = Twetbulb + 273.15
 Tboil        = Tboil    + 273.15
 temperature  = Twetbulb

# Diffusivity estimation based on mean radius 'a' and on initial temperature
D  = Kb*temperature / (6*math.pi*eta_l*a) #[m^2/s]

# Peclet number estimation
Pe = R0**2 / (tau*D)

# Array identifying particles on the surface by assigning a '1' to their index. At the beginning, no pcles on the surface ('0').
 surf_pcles=numpy.zeros(np)

# List of forces and torques to be applied by PyRunner
Fdrag  = numpy.zeros((np,3)) # Drag  force
Tdrag  = numpy.zeros((np,3)) # Drag  torque
Fbrown = numpy.zeros((np,3)) # Brown force
Tbrown = numpy.zeros((np,3)) # Brown torque
 Fsurf  = numpy.zeros((np,3)) # Capillar force



### SIMULATION LOOP
O.engines=[
 ForceResetter(),
 InsertionSortCollider([Bo1_Sphere_Aabb(aabbEnlargeFactor=r_int, label='bo1s')]),
 InteractionLoop(
 [Ig2_Sphere_Sphere_ScGeom6D(interactionDetectionFactor=r_int, label='ig2ss')],
 [Ip2_CohFrictMat_CohFrictMat_CohFrictPhys(
```

```
  setCohesionNow=True, setCohesionOnNewContacts=True, label="cohesiveIp")],
[Law2_ScGeom6D_CohFrictPhys_CohesionMoment(useIncrementalForm=True,label="cohesiveLaw")]
),
NewtonIntegrator(gravity=(g_x, g_y, g_z),damping=0.2),
# Spray drying functions (user-defined)
PyRunner(iterPeriod=1 ,dead=False ,command='check()' ,label='labelCheck'),
PyRunner(iterPeriod=iterPeriod ,dead=False ,command='update()' ,label='labelUpdate'),
PyRunner(iterPeriod=iterPeriod ,dead=False ,command='temp()' ,label='labelTemp'),
PyRunner(iterPeriod=iterPeriod ,dead=False ,command='applysurf()' ,label='labelApplysurf'),
PyRunner(iterPeriod=iterPeriod ,dead=False ,command='drag()' ,label='labelDrag'),
]

### Brownian Force ###
if (EnableBrownian):
  O.engines=O.engines+[
     PyRunner(iterPeriod=iterPeriod ,dead=False ,command='brownian()',label='labelBrownian'),
     ]

### Thermal Expansion Phase ###
if (EnableThermExp):
  O.engines=O.engines+[
     PyRunner(iterPeriod=iterPeriod ,dead=True ,command='updateExp()',label='labelUpdateExp'),
     PyRunner(iterPeriod=iterPeriod ,dead=True ,command='applysurfExp()',label='labelApplysurfExp'),
     ]

### At the end of the loop, add engines for summation of forces and output message ###
O.engines=O.engines+[
  PyRunner(iterPeriod=iterPeriod ,dead=False ,command='sum()',label='labelSum'),
  PyRunner(iterPeriod=iterPeriod*10000,dead=False ,command='output()',label='labelOutput'),
  ]
```

```




# Critical timestep
O.dt=TimeStepFrac*utils.PWaveTimeStep()

# Iterations required to complete the shrinkage of the drop
iterTau     = int(tau/O.dt)
# Iterations required to complete the thermal expansion phase
iterTauExp  = int(tauExp/O.dt)

# Characteristic forces estimation: capillary force, drag force,
    brownian motion
# NB: R0/tau is a reference velocity for pcles following the
    droplet surface
Fsurf_char   = 2*math.pi*a*sigma
Fdrag_char   = 6*math.pi*eta_l*a*(R0/tau-u_lx)
Fbrown_char = (24*Kb*temperature*6*math.pi*eta_l*a/(O.dt*
    iterPeriod) )**(3/2)

# Solid Volume Fraction 'phi'
VolumeDroplet = (4/3)*math.pi*(R0**3)
VolumeSolid    = numpy.sum([4/3*math.pi*b.shape.radius**3 for b in
    O.bodies if isinstance(b.shape,Sphere)])
phi   = VolumeSolid/VolumeDroplet

# Inizialization
R           = R0
R_initial   = R0
R_final     = R0
dR          = 0.0

# Terminal output for the user
print ("\nMESSAGE:")
print ("NP (monomers) = %i " %np)
if BimodalBool:
  print("Bimodal distribution of monomers: aMin=%5.2e" %aMin)
  print("\t\t\taMax=%5.2e" %aMax)
else:
  print("Uniform distribution of monomers: a=(%8.2e+/-%5.2e) m" %(
    a,a*fuzz))
print ("Droplet radius =  %8.2e m " %R0)
```

```
print ("Solid fraction =  %8.2e "   %phi)
print ("Drying time     =  %8.2e s " %tau)
print ("Shrinkage vel. k =  %8.2e m^2/s" %k)
print ("Timestep =  %8.2e s " %O.dt)
print ("Cohes. Factor Cn =  %8.2e N/m^2" %Cn)
print ("Cohes. Factor Cs =  %8.2e N/m^2" %Cs)
if(EnableBrownian):
  print ("Brownian motion: ENABLED")
  print ("Temperature = %5.2f K" %temperature)
  print ("Diffusivity = %5.2e m^2/s" %D)
  print ("Peclet   Pe = R0**2/(D*tau) = %5.2f" %Pe)
  print ("\tPe_v = v0*R0/D = k/D = %5.2f\n" %(k/D))
  print ("Characteristic surface  force = %8.3e" %Fsurf_char   )
  print ("Characteristic drag     force = %8.3e" %Fdrag_char   )
  print ("Characteristic brownian force = %8.3e" %Fbrown_char )
  print ("Fsurf  / Fdrag = %8.3e"   %(Fsurf_char /Fdrag_char) )
  print ("Fbrown / Fdrag = %8.3e"   %(Fbrown_char/Fdrag_char) )
  print ("Fbrown / Fsurf = %8.3e\n" %(Fbrown_char/Fsurf_char) )
else:
  print ("Brownian motion: DISABLED")
if(EnableThermExp):
  print ("Thermal Expansion Phase: ENABLED")
  print ("Therm.Exp. time  tauExp =  %8.2e s" %tauExp)
  print ("Expansion vel.   kExp   =  %8.2e m^2/s" %kExp)
  print ("To complete the drying process, %i iterations are needed." %(iterTau+iterTauExp) )
  print ("Execute the command line 'O.run(%i)' or 'O.run(iterTauExp)'." %(iterTau+iterTauExp) )
  print ("Execute 'O.run(iterTau)'to simulate the shrinkage of the droplet up to R=0.")
  print ("Execute 'O.run(iterTau+iterTauExp)' to observe the behaviour of the cluster also in the thermal expansion phase.")
else:
  print ("Thermal Expansion Phase: DISABLED")
  print ("To complete the drying process, %i iterations are needed." %iterTau  )
  print ("Execute the command line 'O.run(%i)' or 'O.run(iterTau)'." %iterTau  )
  print ("Execute 'O.run(iterTau)'to simulate the shrinkage of the droplet up to R=0.")


### Verify the brownian motion condition
```

```
if (EnableBrownian):
  print("\n")
  R_initial = R0
  R_final   = R0
  dR        = 0.0
  iterVerifyBrownian=int(tau/(O.dt*iterPeriod))
  for iii in range(iterVerifyBrownian):
    R_final = math.sqrt( R0**2 - k*O.dt*iterPeriod*iii )
    dR = R_initial-R_final
    if dR>a/50:
      print("### ERROR: dR too high, reduce timestep or 'iterPeriod'!\n")
      exit()
    R_initial = R_final


### Verify that tauCrust is lower than tau
if tauCrust>=tau:
  print("### ERROR: tauCrust too high, reduce it!")
  exit()




### LIST OF FUNCTIONS

# 'check' function: Identify the end of the drying process. When the process is done:
#  1. Print a message on terminal for the user;
#  2. Impose R = 0.0;
#  3. Print final position of monomers on an output file;
#  4. Start the thermal expansion phase
def check():
  global R
  if  O.iter==(iterTau-1) :
    # 1.
    print ("\n\nShrinkage of the drop is finished. Beginning the thermal expansion phase.\n")
    # 2.
    print("Percentage of radius reduction: %5.3f" %(1.-R/R0) )
    R=0.0
    # 3.
    a_output=a/L ; r_max=0.0
```

```
    # use O.tags['d.id'] to distinguish individual runs of the same simulation
    fileGeoOut = open(folder+"/FinalGeometry_tau"+".geo","w")
    fileGeoOut.write("# monomer mean radius a\n")
    fileGeoOut.write(" %5.2f \n" %a_output )
    fileGeoOut.write("# number of monomers np\n")
    fileGeoOut.write(" %5i \n" %np)
    fileGeoOut.write("#\tid\t\tx\t\ty\t\tz\t\tr\t\ta\n")
    for i in range(np):
      sph = O.bodies[i]
      x  = sph.state.pos[0]/L
      y  = sph.state.pos[1]/L
      z  = sph.state.pos[2]/L
      ai = sph.shape.radius/L
      distFromOrigin = math.sqrt( x**2+y**2+z**2 )
      r_ext = math.sqrt(x**2 + y**2 + z**2)
      if r_ext>r_max: r_max=r_ext
      fileGeoOut.write("%8i\t%8.4f\t%8.4f\t%8.4f\t%8.4f\t%8.3f \n"
        %(i+1,x,y,z,distFromOrigin,ai))
    fileGeoOut.write("\n")
    fileGeoOut.close()

  # 4.
  if O.iter > (iterTau) :
    labelUpdate.dead = True
    labelApplysurf.dead = True
    if (EnableThermExp):
      labelUpdateExp.dead = False
      labelApplysurfExp.dead = False


  if O.iter==(iterTau+iterTauExp-1) :
    a_output=a/L
    fileGeoOut = open(folder+"/FinalGeometry_tauExp"+".geo","w")
    fileGeoOut.write("# monomer mean radius a\n")
    fileGeoOut.write(" %5.2f \n" %a_output )
    fileGeoOut.write("# number of monomers np\n")
    fileGeoOut.write(" %5i \n"   %np)
    fileGeoOut.write("#\tid\t\tx\t\ty\t\tz\t\tr\t\ta\n")
    for i in range(np):
      sph = O.bodies[i]
      x = sph.state.pos[0]/L
      y = sph.state.pos[1]/L
```

```
      z = sph.state.pos[2]/L
      ai= sph.shape.radius/L
      distFromOrigin = math.sqrt( x**2+y**2+z**2 )
      fileGeoOut.write("%8i\t%8.4f\t%8.4f\t%8.4f\t%8.4f\t%8.3f \n"
        %(i+1,x,y,z,distFromOrigin,ai))
    fileGeoOut.write("\n")
    fileGeoOut.close()

  # INTERMEDIATE GEOMETRIES
  # adimensional time theta=k*t/(R0**2) ; geometries for around theta=theta_0 , theta=theta_1 , theta=theta_2
  if O.iter==int(iterTau*theta_0)+1 or O.iter==int(iterTau*theta_1)+1 or O.iter==int(iterTau*theta_2)+1 :
    a_output=a/L
    filename=( "/theta%5.2fR%5.3e.geo" %( k*O.time/(R0**2), R ) )
    fileGeoOut = open(folder+filename,"w")
    fileGeoOut.write("# monomer mean radius a\n")
    fileGeoOut.write(" %5.2f \n" %a_output )
    fileGeoOut.write("# number of monomers np\n")
    fileGeoOut.write(" %5i \n"  %np)
    fileGeoOut.write("#\tid\t\tx\t\ty\t\tz\t\tr\t\ta\n")
    for i in range(np):
      sph = O.bodies[i]
      x = sph.state.pos[0]/L
      y = sph.state.pos[1]/L
      z = sph.state.pos[2]/L
      ai= sph.shape.radius/L
      distFromOrigin = math.sqrt( x**2+y**2+z**2 )
      fileGeoOut.write("%8i\t%8.4f\t%8.4f\t%8.4f\t%8.4f\t%8.3f \n"
        %(i+1,x,y,z,distFromOrigin,ai))
    fileGeoOut.write("\n")
    fileGeoOut.close()

# 'update' function: update the value of R during the shrinkage
def update():
  global R
  R = math.sqrt( R0**2 - k*O.time )

# 'updateExp' function: update the value of R during the thermal expansion
def updateExp():
  global R
  R = math.sqrt( kExp*(O.time-tau) )
```

```

# 'temp' function: update the value of T from Twetbulb to Tboil when the crust is formed
def temp():
  global temperature
  if (O.time>tauCrust) and (O.time<=tau):
    temperature = Twetbulb + (Tboil-Twetbulb)*(O.time-tauCrust)/(tau-tauCrust)

# 'applysurf' function: calculate the centripetal force for pcles lying on the surface of the drop in the shrinkage phase
def applysurf():
  global surf_pcles
  global Fsurf
  for i in range(np): # loop for every particle;
    surf_pcles[i]=0 # initialization;
    sph = O.bodies[i] # index of particle i;
    x   = sph.state.pos[0] # x position of particle i;
    y   = sph.state.pos[1] # y position of particle i;
    z   = sph.state.pos[2] # z position of particle i;
    ai  = sph.shape.radius # radius of particle i;
    pos = math.sqrt(x**2+y**2+z**2) # distance from origin of particle i;
    if pos<R+ai and pos>R-ai: # if particle i is on surface:
      Fc = 2*math.pi*sigma * math.sqrt(ai**2-(pos-R)**2)
      surf_pcles[i]=1 # define i as a "surface" particle;
      Fsurf[i][0] = -Fc*x/pos # x component of centripetal force;
      Fsurf[i][1] = -Fc*y/pos # y component of centripetal force;
      Fsurf[i][2] = -Fc*z/pos # z component of centripetal force;
    else:
      Fsurf[i][0] = 0.0
      Fsurf[i][1] = 0.0
      Fsurf[i][2] = 0.0

# 'applysurfExp' function: calculate the centripetal force for pcles lying on the surface of the drop in the therm. exp. phase
def applysurfExp():
  global surf_pcles
  global Fsurf
  for i in range(np): # loop for every particle;
    surf_pcles[i]=0 # initialization;
    sph = O.bodies[i] # index of particle i;
    x   = sph.state.pos[0] # x position of particle i;
```

```python
    y   = sph.state.pos[1] # y position of particle i;
    z   = sph.state.pos[2] # z position of particle i;
    ai  = sph.shape.radius # radius of particle i;
    pos = math.sqrt(x**2+y**2+z**2) # distance from origin of particle i;
    if pos<R+ai and pos>R-ai: # if particle i is on surface:
      Fc = 2*math.pi*sigma * math.sqrt(ai**2-(pos-R)**2)
      surf_pcles[i]=1 # define i as a "surface" particle;
      Fsurf[i][0] = +Fc*x/pos # x component of centripetal force;
      Fsurf[i][1] = +Fc*y/pos # y component of centripetal force;
      Fsurf[i][2] = +Fc*z/pos # z component of centripetal force;
    else:
      Fsurf[i][0] = 0.0
      Fsurf[i][1] = 0.0
      Fsurf[i][2] = 0.0

# 'drag' function: apply drag force and torque on all the particles
def drag():
  for i in range(np): # loop for every particle;
    sph = O.bodies[i] # index of particle i;
    x   = sph.state.pos[0] # x position of particle i;
    y   = sph.state.pos[1] # y position of particle i;
    z   = sph.state.pos[2] # z position of particle i;
    pos = math.sqrt(x**2+y**2+z**2) # distance from origin of particle i;
    ai  = sph.shape.radius # radius of particle i;

    if pos<R: # if particle i is inside the drop:
      # Force
      u_px = sph.state.vel[0] # x velocity of particle i;
      u_py = sph.state.vel[1] # y velocity of particle i;
      u_pz = sph.state.vel[2] # z velocity of particle i;

      Fdrag[i][0]  = -6*math.pi*eta_l*ai*(u_px-u_lx) # Drag force along x;
      Fdrag[i][1]  = -6*math.pi*eta_l*ai*(u_py-u_ly) # Drag force along y;
      Fdrag[i][2]  = -6*math.pi*eta_l*ai*(u_pz-u_lz) # Drag force along z;

      # Torque
      w_px = sph.state.angVel[0] # x ang.vel. of particle i;
```

```
      w_py = sph.state.angVel[1] # y ang.vel. of particle i;
      w_pz = sph.state.angVel[2] # z ang.vel. of particle i;

      Tdrag[i][0]  = -8*math.pi*eta_l*(ai**3)*(w_px-w_lx) # Drag torque along x;
      Tdrag[i][1]  = -8*math.pi*eta_l*(ai**3)*(w_py-w_ly) # Drag torque along y;
      Tdrag[i][2]  = -8*math.pi*eta_l*(ai**3)*(w_pz-w_lz) # Drag torque along z;

    else: # pcle not in the liquid, no drag or brownian forces
      Fdrag[i][0]=0.0 ; Tdrag[i][0]=0.0
      Fdrag[i][1]=0.0 ; Tdrag[i][1]=0.0
      Fdrag[i][2]=0.0 ; Tdrag[i][2]=0.0

# 'brownian' function: apply brownian force and torque on all the particles
def brownian():
  for i in range(np): # loop for every particle;
    sph = O.bodies[i] # index of particle i;
    x   = sph.state.pos[0] # x position of particle i;
    y   = sph.state.pos[1] # y position of particle i;
    z   = sph.state.pos[2] # z position of particle i;
    ai  = sph.shape.radius # radius of particle i;
    pos = math.sqrt(x**2+y**2+z**2) # distance from origin of particle i;

    if pos<R: # if particle i is inside the drop:
      # Force
      chi_x = random.random() - 0.5 # x random number between -0.5 and +0.5
      chi_y = random.random() - 0.5 # y random number between -0.5 and +0.5
      chi_z = random.random() - 0.5 # z random number between -0.5 and +0.5
      # Brownian force along x,y,z
      Fbrown[i][0] = math.sqrt( 24*Kb*temperature*6*math.pi*eta_l*ai/(O.dt*iterPeriod) )*chi_x
      Fbrown[i][1] = math.sqrt( 24*Kb*temperature*6*math.pi*eta_l*ai/(O.dt*iterPeriod) )*chi_y
      Fbrown[i][2] = math.sqrt( 24*Kb*temperature*6*math.pi*eta_l*ai/(O.dt*iterPeriod) )*chi_z

```

```
      # Torque
      chi_x = random.random() - 0.5 # x random number between -0.5 and +0.5
      chi_y = random.random() - 0.5 # y random number between -0.5 and +0.5
      chi_z = random.random() - 0.5 # z random number between -0.5 and +0.5
      # Brownian torque along x,y,z
      Tbrown[i][0] = math.sqrt( 24*Kb*temperature*8*math.pi*eta_l*(ai**3)/(O.dt*iterPeriod) )*chi_x
      Tbrown[i][1] = math.sqrt( 24*Kb*temperature*8*math.pi*eta_l*(ai**3)/(O.dt*iterPeriod) )*chi_y
      Tbrown[i][2] = math.sqrt( 24*Kb*temperature*8*math.pi*eta_l*(ai**3)/(O.dt*iterPeriod) )*chi_z

    else: # pcle not in the liquid, no drag or brownian forces
      Fbrown[i][0]=0.0 ; Tbrown[i][0]=0.0
      Fbrown[i][1]=0.0 ; Tbrown[i][1]=0.0
      Fbrown[i][2]=0.0 ; Tbrown[i][2]=0.0

# 'sum' function: sum all the forces and torques acting on all the single particles and apply them
def sum():
  O.forces.reset(resetAll=True) # initialization of applied forces;
  for i in range(np):
    Ftot_x = Fdrag[i][0]+Fbrown[i][0]+Fsurf[i][0]
    Ftot_y = Fdrag[i][1]+Fbrown[i][1]+Fsurf[i][1]
    Ftot_z = Fdrag[i][2]+Fbrown[i][2]+Fsurf[i][2]
    Ttot_x = Tdrag[i][0]+Tbrown[i][0]
    Ttot_y = Tdrag[i][1]+Tbrown[i][1]
    Ttot_z = Tdrag[i][2]+Tbrown[i][2]
    O.forces.setPermF(i,(Ftot_x,Ftot_y,Ftot_z)) # apply total force
    O.forces.setPermT(i,(Ttot_x,Ttot_y,Ttot_z)) # apply total torque

# 'output' function: print terminal output during the simulation
def output():
  print ("Iter  : %i"    %O.iter)
  print ("Time  : %8.4e" %O.time)
  print ("R     : %8.4e" %R)
  print ("Temp.: %8.4e" %temperature)
```

```
  if O.iter > iterTau:
    print ("phase: Thermal Expansion")
    print (" kExp: %8.2e" %kExp)
  else:
    print ("phase: Drying")
    print (" k: %8.2e" %k)

  print ("Particles on surface: %i \n" %numpy.sum(surf_pcles))
#####################


### OTHER COMMANDS ###
# Save initial state of simulation (needed to restart)
O.saveTmp()
#####################


### VTK for ParaView ###
if (EnableVTK):
  # Define the iterperiod for the VTKRecorder engine to obtain the
     desired number of frames
  snapPeriod=int((iterTau+iterTauExp)/frames)
  # Add the VTKRecorder to the engines. Save data of the spheres
  O.engines=O.engines+[
  VTKRecorder(iterPeriod=snapPeriod,recorders=['spheres'],fileName
   =folder+'/vtkframe_'),
  ]
  # Add a function that saves position and radius of the droplet
    at every frame
  O.engines=O.engines+[
  PyRunner(iterPeriod=snapPeriod,dead=False,command='droplet()',
    label='labelDroplet' ),
  ]
  # open the file
  fileDroplet = open(folder+"/droplet"+".dat","w")
  fileDroplet.write("frame\tTime\t\tRdroplet\tTemperature\n")
  frame_cntr = 0
  # 'droplet ' function: generate a file containing info on the
    droplet
  def droplet():
    global frame_cntr
    frame_cntr=frame_cntr+1
    fileDroplet.write("%6i\t%5.2e\t%8.3e\t%8.3e\n"
```

```
       %(frame_cntr,O.time,R,temperature) )
#######################


### LAUNCH THE SIMULATION ###
# at the end of the script, run the simulation for the desired number of iterations.
if (runAuto):
  if (EnableThermExp):
    O.run(iterTau+iterTauExp)
  else:
    O.run(iterTau)
# when running with yade-batch, the script must not finish until the simulation is done fully.
# this command will wait for that (has no influence in the non-batch mode)
waitIfBatch()
############################
```

Appendix B

Law for droplet vaporization

The radius reduction over time for an evaporating droplet follows a r^2-law, extracted using a coupling between mass balance and energy balance. Let's imagine a uniform, spherical droplet in air: r is the radial coordinate, R is the droplet radius, $Y_{F,s}$ and T_s are the fluid mass fraction and the temperature at the interface, respectively. $Y_{F,\infty}$ and T_∞ are the water mass fraction in the surrounding gas and the ambient temperature (Figure B.1).

Other assumptions are:

- Uniform temperature in the droplet;
- Single component liquid, in which gas is not soluble;
- The gas surrounding the droplet is quiescent;
- Quasi-steady state;

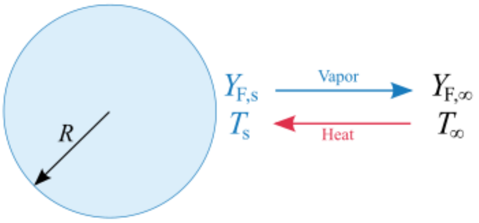

Fig. B.1 Evaporation of a droplet: radius of the droplet, fluid mass fraction and temperature at interface and in the external medium.

- Fick's law for diffusion is valid;
- Constant thermophysical properties, such as diffusivity D, specific heat capacity c_p, thermal conductivity λ and diffusivity α;
- Lewis number $Le = \alpha / D = 1$.

Under these hypoteses, the evaporating mass flow-rate can be determined. In quasi-steady state, Eq. B.1 can be written. The gas flow rate is zero and the mass flow-rate can be expressed in terms of mass flux $\dot{m}''$ (Eq. B.2).

$$\dot{m}(r) = const. = \dot{m}_{gas} + \dot{m}_F \tag{B.1}$$

$$\dot{m}(r) = \dot{m}_F = 4\pi r^2 \dot{m}'' = const. \tag{B.2}$$

From the conservation of species F:

$$\begin{aligned} \dot{m}''_F &= Y_F \dot{m}'' - \rho D \nabla Y_F \\ \frac{\dot{m}}{4\pi r^2} &= Y_F \frac{\dot{m}}{4\pi r^2} - \rho D \nabla Y_F \\ \dot{m} &= -4\pi r^2 \frac{\rho D}{1 - Y_F} \frac{dY_F}{dr} \end{aligned} \tag{B.3}$$

Finally, the flow-rate can be defined in terms of a quantity called r_y^*.

$$\frac{dY_F}{1 - Y_F} = -\frac{\dot{m}}{4\pi\rho D} \frac{dr}{r^2} = r_y^* \frac{dr}{r^2} \tag{B.4}$$

$$\dot{m} = -4\pi\rho D r_y^* \tag{B.5}$$

Integrating Eq. B.4 between R and a generic r, Eq. B.6 is obtained. If $r \to \infty$, a mass transfer number B_y can be defined (Eq.B.7). Coupling Eq. B.5 and B.7, a new definition for the mass flow-rate is obtained (Eq. B.8).

$$Y_F(r) = 1 - \frac{(1 - Y_{F,s})\, e^{-r_y^*/r}}{e^{-r_y^*/R}} \tag{B.6}$$

$$\frac{r_y^*}{R} = ln\left(\frac{1 - Y_{F,\infty}}{1 - Y_{F,s}}\right) \; ; \; B_y \equiv \frac{Y_{F,s} - Y_{F,\infty}}{1 - Y_{F,s}} \tag{B.7}$$

$$\dot{m} = -4\pi\rho D R \, ln(1 + B_y) \tag{B.8}$$

At this point, $\dot{m}$ and $Y_{F,s}$ are unknown. To close the problem, energy balance is employed (Eq. B.9). Also in this case, the equation can be re-arranged in order to define a term r_h^* (Eq. B.10) and it can be integrated.

$$\dot{m}c_p \frac{dT}{dr} = \frac{d}{dr}\left(\lambda 4\pi r^2 \frac{dT}{dr}\right) \tag{B.9}$$

$$r_h^* = \frac{\dot{m}c_p}{4\pi\lambda} \tag{B.10}$$

$$\begin{aligned} r_h^* \frac{dT}{dr} &= \frac{d}{dr}\left(r^2 \frac{dT}{dr}\right) \\ r_h^* T + const &= r^2 \frac{dT}{dr} \end{aligned} \tag{B.11}$$

At the surface, it has to be true that:

$$R^2 \left[\frac{dT}{dr}\right]_s = \frac{\dot{m}}{4\pi\lambda} h_{fg} \tag{B.12}$$

From this condition, it can be derived that $const = r_h^* \left(h_{\mathrm{fg}}/c_p - T_s\right)$ and therefore:

$$r^2 \frac{dT}{dr} = r_h^* \left(T - T_s + h_{fg}/c_p\right) \tag{B.13}$$

Integrating similarly to the species conservation equation, we can define the mass flow-rate in terms of a heat transfer number B_h.

$$B_h \equiv \frac{c_p \left(T_\infty - T_s\right)}{h_{fg}} \tag{B.14}$$

$$\dot{m} = -4\pi\rho\alpha R \, ln(1 + B_h) \tag{B.15}$$

Now a comparison between Eq. B.8 and B.15 can be done. If the Lewis number Le is equal to 1, then $\alpha = D$ and therefore $B_y = B_h$.

$$\frac{Y_{F,s} - Y_{F,\infty}}{1 - Y_{F,s}} = \frac{c_p \left(T_\infty - T_s\right)}{h_{fg}} \tag{B.16}$$

To close the problem, a relation between $Y_{F,s}$ and T_s is needed. This relation is provided by the Clausius-Clapeyron equation, if phase equilibrium between liquid and vapor at droplet surface is assumed. Eq. B.8 and B.15 can be re-arranged in the following way:

$$\frac{\dot{m}}{R} = -4\pi\rho DR\, ln(1+B_y) = -4\pi\rho\alpha R\, ln(1+B_h) \tag{B.17}$$

If ρD, $\rho\alpha$, B_y and B_h are constant, also $\dot{m}/R$ is constant. It is now possible to extract the droplet radius shrinking law. Up to now, the symbol ρ has referred to the gas density ρ_g. The relation between mass flow-rate and droplet radius can be expressed as:

$$\frac{\dot{m}}{R} = -4\pi\rho_g\alpha R\, ln(1+B_h) \tag{B.18}$$

The mass of the droplet is $m = 4/3\pi\rho_l R^3$, from which it can be written:

$$\begin{aligned} \dot{m} &= \frac{4}{3}\pi\rho_l 3R^2\dot{R} \\ \dot{m} &= 4\pi\rho_l R^2\dot{R} \\ \frac{\dot{m}}{R} &= 4\pi\rho_l R\dot{R} \end{aligned} \tag{B.19}$$

$$\frac{\dot{m}}{R} = 2\pi\rho_l\frac{d(R^2)}{dt} \tag{B.20}$$

Putting together Eq. B.18 and B.20, the evaporation constant k can be defined and, knowing that $R(t=0)$ is equal to R_0, the droplet radius shrinking law is obtained.

$$\frac{d(R^2)}{dt} = -\frac{2\rho_g\alpha\, ln(1+B_h)}{\rho_l} = k \tag{B.21}$$

$$R^2 = R_0^2 - k\cdot t \tag{B.22}$$